

Department of Physics and Astronomy

University of Heidelberg

Master thesis

in Physics

submitted by

Max Heikenfeld

born in Witten

2013

**Modelling the Thermal Dynamics of Polygonal Soil
Structures in the Permafrost of the Lena Delta,
Northern Siberia**

This Master thesis has been carried out by Max Heikenfeld

at the

Institute of Environmental Physics

under the supervision of

Prof. Dr. Kurt Roth

PD Dr. Julia Boike (Alfred Wegener Insitute Potsdam)

Modelling the Thermal Dynamics of Polygonal Soil Structures in the Permafrost of the Lena Delta, Northern Siberia

Patterned ground structures characterised by strong heterogeneities in surface and subsurface properties are a common feature of permafrost landscapes in the Arctic. In this thesis, an existing permafrost model including conductive heat transfer and the phase change of water is extended to simulate the thermal dynamics of polygonal soil structures in an Arctic tundra wetland in Northern Siberia. A two-dimensional model formulation in cylindrical coordinates is implemented and coupled to a surface energy balance model. The model performance is assessed by a comparison with analytical solutions and field measurements of soil temperature and surface heat fluxes. The heat transfer in the soil is represented well with mean absolute deviations of up to 1 °C. The coupled simulations with surface energy balance calculation represent the soil temperatures with larger deviations that can be attributed to the description of the snow cover in the model. Lateral heat fluxes in the polygon only occur during limited periods and do not have a substantial impact on the thermal dynamics of the system. Simplified one-dimensional model descriptions based on averaged soil and surface parameters show a cold bias of up to 0.7 °C in the mean annual temperature of the permafrost compared with the detailed two-dimensional model. The thaw depth is simulated consistently by the models of different complexity .

Modellierung der Temperaturdynamik von polygonalen Bodenstrukturen im Permafrostboden des Lena-Deltas in Nordsibirien

Frostmusterböden mit starker Heterogenität in den Boden- und Oberflächeneigenschaften sind charakteristisch für die Permafrostgebiete der Arktis. In dieser Arbeit wird ein existierendes Permafrostmodell für konduktiven Wärmetransport im Boden inklusive des Phasenwechsels von Wasser erweitert um die Temperaturdynamik von polygonalen Bodenstrukturen in der Tundra Nordsibiriens zu simulieren. Es wird eine zweidimensionale Beschreibung in Zylinderkoordinaten entwickelt und an ein Oberflächenenergiebilanzmodell gekoppelt. Zur Überprüfung der Modellergebnisse werden analytische Lösungen der Wärmeleitungsgleichung betrachtet und ein Vergleich mit gemessenen Bodentemperaturen und Wärmeflüssen durchgeführt. Der Wärmetransport im Boden wird mit mittleren absoluten Abweichungen von bis zu 1 °C gut repräsentiert. Die gekoppelten Simulationen mit Berechnung der Oberflächenenergiebilanz weisen größere Abweichungen auf, die hauptsächlich auf die Beschreibung der Schneedecke im Modell zurückgeführt werden können. Laterale Wärmeflüsse treten im Polygon nur in beschränkten Zeiträumen auf und haben keinen nennenswerten Einfluss auf die Temperaturdynamik des Systems. Vereinfachte eindimensionale Modellbeschreibungen auf Basis von gemittelten Boden- und Oberflächenparametern zeigen eine Unterschätzung der Jahresmitteltemperaturen im Permafrost von bis zu -0.7 °C gegenüber detaillierten zweidimensionalen Simulationen. Die Auftautiefe des Bodens wird von den Modellen unterschiedlicher Komplexität konsistent repräsentiert.

Contents

1	Introduction and motivation	1
2	Theory and background	3
2.1	Surface energy balance	3
2.2	Heat transfer in soils	5
2.3	Turbulent transport in the atmospheric boundary layer	8
2.4	Permafrost and polygonal tundra	12
3	Study site and measurement data	17
3.1	Study site: Samoylov Island (Lena River delta, Siberia)	17
3.2	Measurement data	17
4	Model description	27
4.1	The basic model formulation	27
4.2	Surface energy balance model	29
4.3	Two-dimensional model formulation in cylindrical coordinates	31
4.4	Numerical solution	35
4.5	Model set-up	36
5	Model quality assessment	41
5.1	Comparison of the simulations with analytical solutions	42
5.2	Soil model with forcing from soil temperature measurements	45
5.3	Simulations with the coupled surface energy balance	49
5.4	Discussion	58
6	Two-dimensional simulations of the thermal dynamics of a polygon	65
6.1	Two-dimensional heat fluxes in the polygon	65
6.2	Comparison of model configurations of different complexity	70
6.3	Discussion	75
7	Conclusions and outlook	81
8	Lists	85
8.1	List of Figures	85
8.2	List of Tables	86
8.3	List of abbreviations and variables	87
9	Bibliography	89

A	Appendix	95
A.1	Universal functions	95
A.2	Freezing characteristics	97
A.3	Correction of soil temperature offset	101
A.4	Soil model with forcing from temperature sensors	103
A.5	Coupled model with surface energy balance calculations	105
A.6	Variation of the organic surface layer	107

1 Introduction and motivation

Permafrost is an important phenomenon of the Earth's continental surface and subsurface covering about 25 % of the Northern Hemispheric land surface (French, 2007; Brown et al., 1997). Permafrost can be found in the Arctic regions of Alaska, Canada, Greenland, Northern Europe and Asia as well as in high mountain ranges (French, 2007). The polar regions and high mountain areas are expected to face the most drastic warming in the next century (ACIA, 2004; IPCC, 2007). Temperature increases in the Arctic permafrost have already been observed in the past years and decades in different regions of the Arctic (Romanovsky et al., 2010b; Smith et al., 2010; Christiansen et al., 2010). The thermal state of permafrost is of high relevance for a wide range of ecosystem processes in these areas, such as local and regional hydrology or atmospheric conditions (French, 2007). Permafrost soils contain large amounts of organic carbon of different age and biochemical state. Substantial amounts of these carbon deposits could be released into the atmosphere in the form of methane or carbon dioxide due to a destabilisation of permafrost soils in the following centuries. This would form a positive feedback mechanism in the climate system (Zimov et al., 2006; Tarnocai et al., 2009). However, the sensitivity of permafrost carbon to rising temperatures and the complex interplay with other processes such as land cover changes are still open research questions (Schuur et al., 2009).

Permafrost landscapes are often characterised by strong heterogeneities of soil composition and surface properties on different length scales. These often occur as so called patterned ground structures on a scale of metres to tens of metres and are formed based on processes connected to the freeze-thaw dynamics of the soil or mechanical effects due to the large temperature range in the course of the annual cycle (French, 2007). In high-latitude wetlands the landscape is often dominated by low-centred polygons created by frost-cracking and the formation of ice-wedges (Lachenbruch, 1962; Mann, 2003). This landscape type shows strong heterogeneities of both surface and subsurface characteristics on a scale of metres to tens of metres between the elevated rims and the depressed centres of the polygons. That includes, for example, water content, albedo or roughness length. These properties determine the heat transfer processes in the soil and at the soil surface. A pronounced microtopography leads to strong differences in snow depth which determines the insulation of the soil during the cold winter period.

Previous studies in this landscape type revealed distinct differences in the surface energy balance for the different compartments (Kutzbach, 2006; Langer et al., 2011a). Variations in snow cover thickness and soil water content were determined as main factors affecting the thermal state of the under-laying permafrost (Langer et al.,

2013). Given these strong lateral variations in the parameters governing the heat transfer processes, substantial lateral heat fluxes can be expected inside the polygons. These horizontal heat fluxes are not described by the common one-dimensional permafrost modelling (Riseborough et al., 2008), which could lead to biases in the simulation of the thermal state of permafrost in such landscape type.

An established model for heat transfer in permafrost soils based on heat conduction and the phase change of water (Westermann, 2010; Westermann et al., 2011; Langer et al., 2013) is extended to a two-dimensional formulation. Cylindrical coordinates are chosen to represent the approximately circular shape of the polygonal soil structures. Furthermore, a surface energy balance model is coupled to the soil heat transfer model so that the forcing can be provided by meteorological measurements. This allows to include lateral heterogeneities in both subsurface soil composition and surface properties in the simulations of the thermal dynamics.

To assess the quality of the model, simulations are performed with gradually increased physical complexity. The numerical accuracy of the heat transfer model scheme is investigated for special cases that feature analytical solutions of the non-linear problem of heat transfer with phase change. The accuracy of the simulations of heat transfer in the soil and the choice of the soil parametrisation are examined with simulations based on boundary forcing from measured soil temperatures close to the soil surface. Simulations of the coupled model including the surface energy balance and soil heat transfer are compared to measurements of soil temperature and heat fluxes both at the surface and in the ground. This allows for the identification of the main factors that determine the heat transfer processes at the surface and subsurface of the permafrost landscape.

The two-dimensional model formulation is used to simulate the thermal dynamics of a tundra polygon with two main research questions. The simulation results will allow to investigate to which extent lateral heat fluxes occur within the subsurface of the polygon and give quantitative information about the magnitude of these fluxes in comparison to the vertical fluxes.

Large scale climate models for climate research or weather prediction use different approaches to include heterogeneities in the surface cover at subgrid scales in their internal surface energy balance calculations (Avisar and Pielke, 1989; Giorgi and Avisar, 1997). The results of a detailed two-dimensional model simulation are compared to simplified model schemes based on one-dimensional heat transfer in the soil and averaged soil and surface parameters to reveal effect of such simplifications on key parameters of permafrost landscapes such as average soil temperatures and thaw depth. This gives an assessment of the representation of the thermal dynamics in polygonal tundra landscape in usual one-dimensional model schemes.

2 Theory and background

The thermal dynamics of the ground are determined by the heat transfer processes inside the soil and the heat exchange with the atmosphere at the ground surface. In this chapter the theoretical background of the numerical model description used to simulate the heat transfer processes in the soil and at the soil surface are outlined. The physical processes involved in the thermal dynamics include radiative and turbulent diffusive heat transfer in the atmosphere, conductive heat transfer in the soil and the phase change of water between liquid water and ice. This will be completed by a short introduction into the basic characteristics of permafrost soils and into the relevant features of the landscape type of polygonal tundra.

2.1 Surface energy balance

The energy balance at the earth's surface is made up by the different heat flux processes in the two adjacent compartments of the solid earth and the atmosphere, i.e the soil and the atmospheric boundary layer. This includes the net radiation budget Q_{net} , the turbulent fluxes of sensible heat Q_{h} and lateral heat Q_{e} , and the ground heat flux Q_{g} . The description of the heat fluxes at the surface follows the sign conventions that has become a certain standard in the description of surface energy balances (Foken, 2008a; Kraus, 2008). All radiation fluxes, both incoming and outgoing, are described by positive values and the net radiation is positive when it is directed towards the earth's surface while the other heat fluxes are chosen positive when directed away from the surface. Hence, a positive sensible or latent heat flux is cooling the surface, whereas a positive ground heat fluxes lead to a warming of the subsurface.

Conservation of energy balance at the surface is ensured

$$Q_{\text{net}} = Q_{\text{h}} + Q_{\text{e}} + Q_{\text{g}}. \quad (2.1)$$

Radiation in the earth's atmosphere is present in two distinct wavelength bands (Foken, 2008a). Short-wave radiation Q_{SW} includes the incoming sunlight and the scattered and reflected light in the ultraviolet, optical and near infrared range ($\lambda \approx 5 - 2800 \text{ nm}$). The thermal radiation emitted by the earth's surface and the atmosphere makes up the long-wave radiation Q_{LW} in the infrared spectrum ($\lambda \approx 5 - 50 \mu\text{m}$). The net radiation is given by

$$Q_{\text{net}} = Q_{\text{SW,in}} - Q_{\text{SW,out}} + Q_{\text{LW,in}} - Q_{\text{LW,out}}. \quad (2.2)$$

The albedo A is the ratio of reflected to incoming radiation in the short-wave range

$$A = \frac{Q_{\text{SW,out}}}{Q_{\text{SW,in}}}. \quad (2.3)$$

The emissivity ϵ in the thermal range gives the fraction of the incoming radiation that is absorbed by the surface. Furthermore, the emission of thermal radiation depends on the surface temperature T_s which is described by Stefan-Boltzmann's law

$$Q_{\text{LW,out}} = \epsilon\sigma T_s^4 + (1 - \epsilon)Q_{\text{LW,in}}, \quad (2.4)$$

with the Stefan-Boltzmann constant $\sigma = 5.67 \cdot 10^{-8} \text{ W m}^{-2} \text{ K}^{-4}$ and the surface temperature T_s . Hence, the total radiation balance at the surface reads

$$Q_{\text{net}} = (1 - A) Q_{\text{SW,in}} + \epsilon Q_{\text{LW,in}} - \epsilon\sigma T_s^4. \quad (2.5)$$

The sensible and latent heat fluxes Q_h and Q_e are forming the turbulent heat exchange in the lower atmosphere that is explained in more detail in Chapter 2.3.

The ground heat flux Q_g in this description of the surface energy balance is the heat flux across the atmosphere-ground interface in summer or the atmosphere-snow interface in winter. The thermal dynamics of the snow cover are regarded separately. However, the presence of snow directly influences the surface energy balance due to surface parameters such as albedo and roughness length that differ strongly from the ones of the ground surface. In addition, snow has a low heat conductivity compared to most soils. This drastically limits the heat flux from the surface into the ground or vice versa during snow covered periods (Goodrich, 1982). During the snow melt, this component of the energy budget can be quite large and accounts for most of the absorbed net radiation (Langer et al., 2011a).

When the components of the energy balance are determined by independent measurements, the energy balance closure term ΔQ (Foken, 2008b) ensures the conservation of energy at the surface

$$Q_{\text{net}} - Q_h - Q_e - Q_g = \Delta Q \neq 0. \quad (2.6)$$

The deviation can be attributed to measurement errors or physical processes not covered in the underlying concepts. Examples are heat storage at the surface or heat transfer processes in the atmosphere that are not covered by the assumptions about turbulence that the measurement principle is based on.

2.2 Heat transfer in soils

Heat transfer in soils can be derived from the conservation of thermal energy

$$\frac{\partial E}{\partial t} = \nabla j_h + S_h \quad (2.7)$$

which states that a change of the thermal energy E of an elementary volume of the soil can only change due to heat fluxes j_h through the boundaries or internal sources of thermal energy S_h . Assuming only conductive heat transport the heat flux is given by Fourier's Law:

$$j_h = -k\nabla T, \quad (2.8)$$

based on the gradient of the soil temperature T and the thermal conductivity k_h . The change in internal energy is related to the temperature change by the volumetric heat capacity c_h of the soil:

$$\frac{\partial E}{\partial T} = c_h = \rho c_m. \quad (2.9)$$

This leads to the diffusive heat conduction equation:

$$c_h(\vec{x}, T) \frac{\partial T}{\partial t} = \nabla (k_h(\vec{x}, T) \nabla T) + S(\vec{x}, t, T) \quad (2.10)$$

The thermal properties of the soil and possible source terms can depend on time, space and soil temperature. In the case of spatially and temporally constant thermal properties c_h and k_h and in the absence of energy sources S in the soil equation (2.10) simplifies to:

$$\frac{\partial T}{\partial t} = \frac{k}{c} \Delta T = D_h \Delta T \quad (2.11)$$

with the thermal diffusivity $D_h = k_h/c_h$.

According to Roth and Boike (2001) the heat transfer in such a linear system can be described by the theory of transfer integrals. The travel time t_{\max} of the maximum of a heat pulse from the boundary of the model domain into a certain depth z can be calculated as

$$t_{\max} = \frac{z^2}{D_h}. \quad (2.12)$$

In this thesis soils of heterogeneous composition with the phase change processes of freezing and thawing are examined which adds a non-linear term to the heat equation so that the basic assumption of linearity that the theory is based on is not valid any more. Nevertheless, these concepts often offers a very intuitive way to estimate the magnitudes or scales of processes, especially in the case of regarding either the

thawed or the frozen parts of the soil independently.

The description of purely conductive heat transfer is based on the assumption that convective transport processes due to the movement of heat with water flow and water vapour transport can be neglected. Weismüller et al. (2011) report a convective heat flux of 3% of the conductive heat flux and even less for water vapour diffusion for a permafrost site on Svalbard. They come to the conclusion that a simulation based on heat conduction and the phase change of water should yield accurate results for most permafrost conditions.

Soil freezing characteristics and the effective heat capacity

While the freezing of liquid water in an open water body occurs at a certain temperature around 0 °C, depending on solute content, water in porous media can be partially liquid over a larger temperature range. The energy balance of the water phase is changed by interfacial forces (Roth, 2012). An additional term is added to the Gibbs free enthalpy that shifts the equilibrium between the two phases of liquid water and ice, depending on the capillary forces inside the pores. Therefore, the liquid water content in the pores gradually decreases with temperature according to the distribution of pore radii with liquid water present at temperatures far below 0 °C. This leads to a continuous function for the amount of liquid water depending on the soil temperature. This relation can be described by empirical functions depending on the respective soil type. The change in liquid water content due to the thawing or freezing of water in the soil is associated with an energy turnover ΔE according to the latent heat of fusion $L_{s,l}$ of water

$$\Delta E = \theta_{w,liq} \rho_w L_{s,l} V, \quad (2.13)$$

where V denotes a soil volume with a total water content of θ_w . This process is very important for the thermal dynamics of freezing and thawing soils as the latent heat of fusion of water is several magnitudes larger than the heat capacities c_h of the materials (Williams and Smith, 1989). This adds an additional term to the heat conduction equation that depends on the variation of liquid water content $\theta_{w,liq}$ with temperature:

$$c_h(\vec{x}, T) \frac{\partial T}{\partial t} = \nabla (k_h(\vec{x}, T) \nabla T) + \rho L_{s,l} \frac{\partial \theta_{w,liq}}{\partial T}. \quad (2.14)$$

The two processes can be combined by incorporating the energy term due to the phase change into the effective heat capacity. This yields an effective heat capacity c_{eff} of the soil

$$c_{\text{eff}} = c_h(T) + \rho_w L_{s,l} \frac{\partial \theta_{w,liq}}{\partial T} \quad (2.15)$$

The heat conduction equation with phase change changes to

$$c_{\text{eff}}(\vec{x}, T) \frac{\partial T}{\partial t} = \nabla (k_h(\vec{x}, T) \nabla T), \quad (2.16)$$

which forms the basis of the soil heat transfer model used in this thesis.

The de Vries model for the thermal conductivity of soils

The thermal conductivity of soil or any other medium that is characterised by the coexistence of different materials cannot be obtained from a simple weighting of the material properties of the constituents, as it is the case for the heat capacity. The configuration of the different constituents influences the bulk conductivity of the material. Small amounts of a highly-conducting material can form heat bridges that strongly enhance the conductive heat transfer inside the material, while a thin but continuous layer of low-conducting material can have a strong insulating effect.

An approach to solve this problem was first presented in de Vries (1963) based on the theory of electric conductivity of granular media. The short description of the model used in this study is mainly based on the formulation given in (Campbell et al., 1994), where the basic theory extended further.

The thermal conductivity of a porous medium is described by the function

$$\frac{\sum_i \theta_i f_i k_i}{\sum_i \theta_i f_i}, \quad (2.17)$$

that adds weighting factors f_i to the sum over the heat conductivities k_i and volumetric fractions θ_i of the the phases i that constitute the porous medium, i.e. liquid water, ice, air, mineral material and organic material. Only one of the components is assumed to form the continuous phase that is interconnected throughout the entire porous medium. The other constituents occur as discontinuous domains surrounded by the continuous phase. k_n denotes the thermal conductivity of the continuous phase.

As mineral and organic material in the soil are assumed to be present as particles, the continuous phase can be formed by either air, water, or ice, depending on total water content and temperature. For an unfrozen soil with high water content, liquid water forms the continuous phase while the ice will take that part in a frozen state. In contrast, air is the continuous phase in a dry soil in frozen and unfrozen state. The weighting factor of the continuous phase is set to unity. For the discontinuous phases, spherical shape is assumed and represented by the following weighting factors:

$$f_i = \frac{1}{1 + \frac{1}{3} \frac{k_i}{k_c}}. \quad (2.18)$$

This ensures the functional dependencies that are expected for this model concept depending on the ratio of the heat conductivity of the continuous phase and the other

soil constituents. The transition from the regime of air to water as the continuous medium is given by the function

$$k_c = k_{\text{air}} + \beta_{\text{air,w}} (k_w - k_{\text{air}}) \quad (2.19)$$

with the weighting coefficient β_{aw} :

$$\beta_{\text{aw}} = \frac{1}{1 + \left(\frac{\theta_w}{\theta_{w0}}\right)^{-q}}. \quad (2.20)$$

The water content $\theta_{w,0} = 0.7$ and the exponent $q = 1.7$ are set according to Campbell et al. (1994). The same calculation is performed for the transition from ice to air and from water to ice. The thermal conductivity can be obtained from an interpolation on the surface spanned by the the vectors of water and ice content (Ippisch, 2001). The dependence of the liquid water content on temperature is based on the freezing characteristics which leads to a temperature dependent heat conductivity of the soil.

This description is of course a simplification that might differ quite substantially from the actual geometry of the soil phases, especially in the case of the organic material and the ice content of the soil. de Vries (1963) assumes that the theory provides soil conductivities with an accuracy of about 10%. This was concluded based on validation experiments in both peat soils and minerals soils. Ippisch (2001) used the formulation for a permafrost soil on Svalbard and achieved good results for the thermal conductivities of the soil material.

2.3 Turbulent transport in the atmospheric boundary layer

Apart from radiation in different wavelength bands, the vertical transport of heat in the atmosphere is mainly driven by turbulent transport processes (Roedel and Wagner, 2011). This includes fluxes of sensible heat and fluxes of latent heat in the form of water vapour. The turbulent flow of a gas or a liquid is physically described by the Navier-Stokes equation from which the relevant transport processes could be derived. However, a direct numerical solution of this equation is not feasible in most practical applications. Therefore, simplified model concepts describing these transport processes are used in most studies.

The lower part of the atmosphere that is directly affected by the hydrodynamical processes induced by the viscous interaction with the Earth's surface is called Planetary boundary layer (PBL) or Atmospheric boundary layer (ABL). This layer is characterised by strong turbulent processes and a rapid vertical mixing. The Atmospheric boundary layer itself is composed of three sublayers of different physical behaviour. They can be classified according to the characteristics of the transfer of momentum. The Viscous layer directly above the land or water surface has a

very small thickness of only a few millimetres. In this layer momentum flux and other transfer processes are dominated by molecular viscosity and molecular diffusion. This results in a linear wind profile (Foken, 2008a). The overlaying Prandtl layer is dominated by turbulent processes and reaches up to heights of several tens of metres depending on the atmospheric stability. The influence of the rotation of the Earth in the form of the Coriolis force can be neglected here. For this study the description of the Prandtl layer is sufficient as the conditions in that layer directly determine the turbulent heat transfer from and towards the Earth's surface.

The transport processes in the ABL are strongly determined by the prevailing temperature profile. The virtual potential temperature Θ_v is a temperature scale in the atmosphere that includes the corrections for temperature for adiabatic processes in uplifting of an air parcel and for the changes in water content (Roedel and Wagner, 2011).

Thus, atmospheric stability can be directly described by the gradient of potential virtual temperature

$$\frac{\partial \Theta_v}{\partial z} \begin{cases} < 0 : \text{unstable} \\ = 0 : \text{neutral} \\ > 0 : \text{stable.} \end{cases} \quad (2.21)$$

The vertical turbulent flux of momentum, sensible heat and water vapour can be attributed to the covariance between the fluctuations of the relevant transported physical quantity and the fluctuations of the vertical wind speed v'_z . For the transport of sensible heat, this includes the heat capacity c_p and density ρ of air with the potential temperature Θ . In the case of the latent heat the fluctuations of the absolute humidity q' are taken into account, along with the latent heat of evaporation of water L_{sl} . The so called K-approach assumes that these fluxes can be described by a diffusive process with the diffusion constant (eddy diffusivity) K and the respective gradient

$$Q_h = c_p \rho \overline{v'_z \Theta'} = -c_p \rho K_h(z, t) \frac{\partial \Theta}{\partial z} \quad (2.22)$$

$$Q_e = L_{lg} \rho \overline{v'_z q'} = -L_{lg} \rho K_h(z, t) \frac{\partial q}{\partial z}. \quad (2.23)$$

The shear velocity or friction velocity is defined as

$$u_* = \overline{u'_x u'_z} = -K_m(z, t) \frac{\partial u}{\partial z}. \quad (2.24)$$

based on dimensional analysis the mixing length theory by Prandtl (1925) predicts a proportionality of the eddy diffusivity to the friction velocity u_* and the height z

for neutral conditions. Inserting this into (2.24) yields

$$u_*^2 = \kappa u_* z \frac{\partial u}{\partial z}, \quad (2.25)$$

where the proportionality constant κ is the so called von Kármán constant. Today measurements give a value of $\kappa = 0.4$ with a high accuracy (Foken, 2008b).

By integration of equation (2.25) from the roughness length z_0 , where the wind speed is assumed to be zero, to the height z the logarithmic wind profile in the Prandtl layer is acquired:

$$u(z) = \frac{u_*}{\kappa} \ln \frac{z}{z_0}. \quad (2.26)$$

For grass covered land typical values lie in the range of several centimetres, while smooth snow surfaces can have roughness length as small as only a few tens of micrometres (Foken, 2008a). Similar logarithmic profiles are expected for temperature and humidity according to equations (2.22) and (2.23).

Monin-Obhukov similarity theory for non-neutral conditions

To extend the description of the atmospheric boundary layer from the case of neutral conditions given above to arbitrary stratification, Monin and Obukhov (1954) developed the Monin-Obhukov similarity theory. A dimensional analysis can be performed according to Buckingham's PI-theorem (Buckingham, 1914), taking into account the physical processes determining the transfer of momentum and heat and the physical units that these properties are based on. It can be shown that the physical quantities such as the profiles of wind speed, temperature, and humidity must be described by functions $\varphi(\zeta)$ of one dimensionless parameter (Roth, 2012; Foken, 2006). From these considerations Monin and Obukhov (1954) derived a characteristic length scale, the so called (Monin-)Obhukov length:

$$L := -\frac{u_*^3 \Theta_v}{\kappa g v'_z \Theta'_v}, \quad (2.27)$$

where g denotes the gravitational acceleration and \bar{T} is the average air temperature. The covariance term $\overline{v'_z \Theta'_v}$ describes the vertical transport of virtual potential temperature. The Monin-Obhukov length can be calculated based on the turbulent heat fluxes according to the definition of the virtual temperature and equations (2.22) and (2.23) (Foken, 2008a)

$$L = -\frac{\rho c_p T}{\kappa g} \frac{u_*^3}{Q_h + 0.61 \frac{T}{L_{sl}} Q_e}. \quad (2.28)$$

This length scale defines the dimensionless stability parameter ζ which is calculated as the ratio of measurement height z and the Monin-Obhukov length L

$$\zeta = \frac{z}{L}. \quad (2.29)$$

Negative values of L and ζ represent unstable conditions, while positive values indicate stable stratification in the atmosphere. The gradients of wind speed, temperature and humidity are modified with the two universal functions ϕ_m and ϕ_h , where the latter function is usually assumed to be valid both for temperature and humidity (Foken, 2008a). Under neutral stratification the covariance term $\overline{v'_z \Theta'_v}$ cancels and the Monin-Obhukov length approaches infinity while the stability parameters ζ approaches zero. This yields a constant universal function which leads to scale-free relation according to equations (2.24), (2.22), and (2.23).

The functions $\phi_m(\zeta)$ and $\phi_h(\zeta)$ can only be restrained to their dependence on the stability parameter $\zeta = z/L$. The detailed form must be derived from intense field measurements that have been conducted in a number of studies for different locations throughout the last decades, e.g. (Businger et al., 1971; Högström, 1988; Grachev et al., 2007). These universal functions are integrated from the roughness length z_0 to the measurement height z , leading to the following terms that describe the corrections to the logarithmic profiles in neutral conditions

$$\Psi_m = \int_{z_0/L}^{z/L} \frac{1 - \phi_m(\zeta)}{\zeta} d\zeta, \quad (2.30)$$

$$\Psi_h = \int_{z_0/L}^{z/L} \frac{1 - \phi_h(\zeta)}{\zeta} d\zeta. \quad (2.31)$$

The friction thus velocity results from the integration of the universal function and the wind speed u in the height z

$$u_* = \kappa u \left(\ln \frac{z_m}{z_0} - \psi \left(\frac{z_0}{L}, \frac{z}{L} \right) \right)^{-1}. \quad (2.32)$$

As pressure differences can be neglected in case of the small heights z of a few metres considered in this thesis, the potential temperature Θ can be replaced by the temperature T . The temperature at the height corresponding to the roughness length is set equal to the surface temperature.

The flux of sensible heat is calculated from the temperature gradient between the surface and the height z , the friction velocity u_* and the volumetric heat capacity

made up by the density of air ρ_{air} and the specific heat capacity of air c_p .

$$Q_h = -\rho_{\text{air}}c_p u_* \overline{v'_z T'} = -\rho_{\text{air}}c_p \kappa u_* (T(z) - T_s) \left(\ln \frac{z_m}{z_0} - \psi_h \left(\frac{z_0}{L}, \frac{z}{L} \right) \right)^{-1}. \quad (2.33)$$

The latent heat flux is obtained accordingly from the difference in absolute humidity q between the soil surface and the measurement height along with the latent heat of evaporation of water $L_{1,g}$

$$Q_e = -\rho_{\text{air}}L_{1,g}u_* \overline{v'_z q'} = -\rho_{\text{air}}L_{1,g}\kappa u_* (q(z) - q_s) \left(\ln \frac{z_m}{z_0} - \psi_h \left(\frac{z_0}{L}, \frac{z}{L} \right) + \kappa u_* r_s \right)^{-1}. \quad (2.34)$$

The additional term $\kappa u_* r_s$ in equation (2.34) accounts for the limited availability of water to evapotranspiration at the surface compared to an open water surface. This is quantified by the surface resistance to evapotranspiration r_s that is determined by vegetation cover and soil moisture (Foken, 2008a).

Högström (1996) and Foken (2006) give estimates of the uncertainty of the universal functions of around 10–20%. These uncertainties directly translate into the uncertainties of the calculated turbulent heat fluxes.

2.4 Permafrost and polygonal tundra

Permafrost is defined as soil that has a temperature below 0 °C for at least two consecutive years (van Everdingen, 1998). Figure 2.4 shows a vertical profile through a

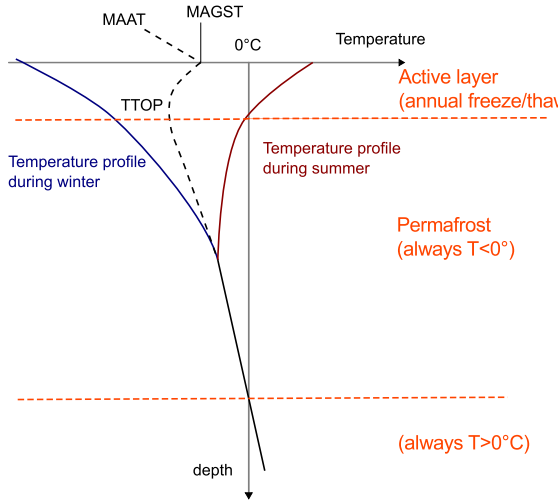


Figure 2.1: Schematic temperature profile in a permafrost soil. The most important layers (active layer, permafrost, continuously unfrozen) separated by the orange lines. The temperature profile is sketched for both the maximum temperatures in summer (*red*), the minimum temperatures in winter (*blue*) and the annual mean (*black, dashed*). Mean air temperature (MAAT), mean annual ground surface temperature (MAGST) and the average temperature at the top of the permafrost (TTOP) are shown with the respective offsets described in this section.

permafrost soil with the temperature curves for the stages of maximum and mini-

imum surface temperature. The subsurface at a permafrost site can be divided into three distinct layers based on the thermal state of the soil. The actual permafrost is the part of the ground where temperatures do not exceed 0°C (van Everdingen, 1998). The active layer is the uppermost soil layer that thaws during summer and is therefore dominated by physical processes connected to the freezing and thawing of the soil. The active layer thickness depends on the meteorological conditions and the soil composition. Permafrost reaches down to certain depth called permafrost base, as soil temperature raises with depth due to the geothermal heat flux. Note that liquid water can be present in the compartment that is continuously below the freezing point of water due to the freezing characteristics described in Chapter 2.2. The thickness of the permafrost layer reaches from a few metres at lower latitudes to 600–1000 m in Northern Siberia (Romanovsky et al., 2004). In contrast to Northern Europe and Canada most of Siberia was not covered by isolating ice sheets during the last glacial period and was present there throughout that time (French, 2007). The permafrost of Siberia is not in equilibrium with the current climatic conditions due to the large thermal inertia of the thick layers of frozen soil. In this thesis a site within the zone of continuous permafrost is investigated. However, large areas are only partially underlain by permafrost, called discontinuous, sporadic or isolated permafrost (Brown et al., 1997; van Everdingen, 1998). The distribution of these zones over the Northern Hemisphere is shown in the first map in Figure 3.1.

Permafrost can generally form at places where the mean annual temperature is below 0°C . However, there are several processes that influence the temperature of the uppermost soil layers. The mean annual ground surface temperature (MAGST) is the determining quantity for the formation or stability of permafrost. It can differ from the mean annual air temperature (MAAT) by several degrees centigrade. This can be explained by the insulation from the low air temperatures that the snow cover provides during the winter months (Goodrich, 1982).

Another offset in the temperature profile is introduced by a combination of the temperature dependence of thermal diffusivity and the exchange of latent heat in the active layer. This leads to a difference in the effective heat transfer between the winter and the summer months. Thus, the mean annual temperature at the top of the permafrost is lower than the average temperature in the active layer (Romanovsky and Osterkamp, 1995; Burn and Smith, 1988). The two contrasting effect partly cancel each other. However, in most cases the warming effect of the snow cover dominates (Zhang, 2005; Goodrich, 1982).

Figure 2.2 shows a schematic overview of the annual cycle of the active layer at a typical wet permafrost site. During the spring after the melting of the snow cover, the thawing front penetrates into the soil. The maximum thaw depth is reached during late summer. During autumn the temperature over the whole active layer decreases to a temperature around 0°C , thus forming the so called zero curtain. The temperature decrease stagnates due to the release of latent heat in the freezing process and the low temperature gradient in the soil. This leads to an isothermal plateau of temperatures characterized by temperatures slightly below 0°C that is present for a period of weeks to months even at times when the air temperature and

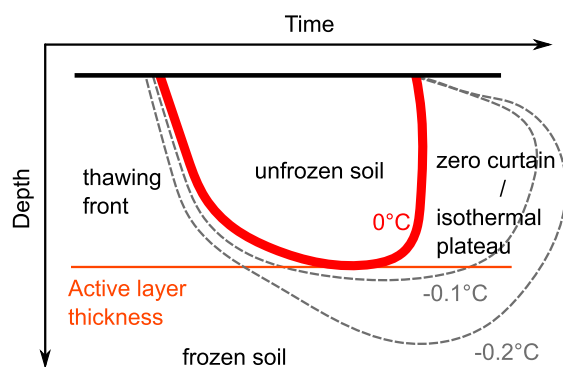


Figure 2.2: Typical yearly cycle of a wet permafrost site with the most important processes. The red line indicates 0°C , the grey dashed depict two slightly negative isothermals.

the surface temperature attain very cold temperatures (Roth, 2012; French, 2007).

Patterned ground and polygonal tundra

Patterned ground structures are a typical feature of permafrost soils (French, 2007). The regular freezing and thawing with the associated volume changes lead to different processes shaping the uppermost soil layers. Typical examples of such patterned ground landscapes range from stone circles (Kessler and Werner, 2003) to mud boils (Boike et al., 2008).

The polygonal tundra studied in this work is a landscape type that is typical for large areas of high latitude wetlands (French, 2007). The formation of the polygons was first described by Leffingwell (1915). During the rapid freezing of the soil in early winter (about $0.5\text{--}1\text{ K d}^{-1}$), the contraction of the ice rich soil leads to tensions that exceed the fracture toughness of the soil, which results in the formation of cracks. During spring the water available from the snow melt enters the cracks and refreezes there due to the cold temperature in the soil. As this process takes place repeatedly over the course of decades and centuries, large ice wedges form beneath the cracks. During their growth these ice wedges push the surrounding soil upwards so that the typical microtopography of elevated rim and depresses centres is formed (French, 2007). However, also other processes including the thermal expansion of the soil in the centre of the polygon are expected to be involved in creating the surface and subsurface shape of the polygons (Washburn, 1980; French, 2007). The development of the polygonal structures has been reproduced in numerical models, for example by Plug and Werner (1998).

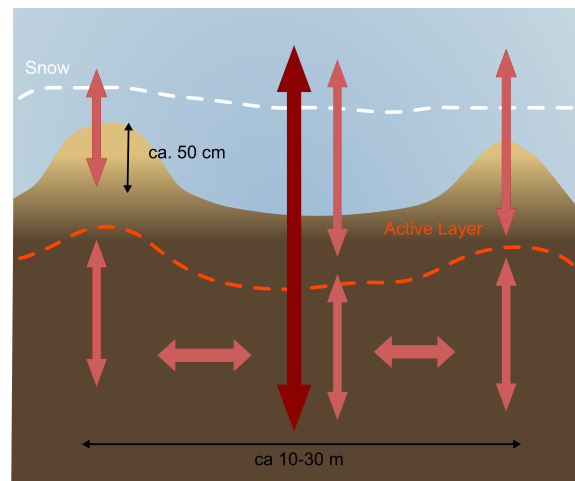
The landscape that forms based on these processes is characterized by a pronounced microtopography and strong lateral heterogeneities in terms of soil and surface properties (French, 2007; Kutzbach, 2006). The depressed centres of the polygons are usually made up by peat soils and feature a water saturation almost up to the surface. The elevated rims consist of predominantly mineral soils due to the redistribution of sediments by the formation of the ice wedge. The rims are covered by a dry moss layer, whereas the vegetation in the centre of the polygon is dominated by sedges and wet moss cover (Kutzbach, 2006).

The distinct differences in both surface and subsurface properties between the two main compartments centre and rim of the polygon give reason to expect influences on the general thermal dynamics in the polygonal soil structures. Figure 2.3 shows a cut through a simplified polygon with the main heat transfer paths that could be subject to such an influence of lateral variations between the centre and the rim of the polygon:

- i) Differences in surface cover and soil moisture in the uppermost soil layer influence the atmospheric heat fluxes due to variations in albedo, roughness length and water availability for evapotranspiration and thus turbulent latent heat flux.
- ii) The snow cover heterogeneity due to the strong microtopography and frequent wind drift processes influences insulation of the uppermost soil layer during winter creating a distinct difference between the thicker snow layer in the centre and almost snow-free polygonal rims.
- iii) Variations of soil water content in the active layer determine the amount of latent heat transformed during the freezing and thawing of the soil. This mainly determines the thaw depth and active layer thickness.
- iv) Soil composition in general influences soil heat conductivity. This is mainly relevant during the winter months, when most water in the soil is frozen and latent heat exchange is negligible.

Lateral heat fluxes at different depths could evolve from these differences in the vertical heat transfer processes, which is a process that is not covered by one-dimensional modelling approaches for permafrost soils.

Figure 2.3: Schematic overview of the heat transfer processes in a typical low-centred tundra polygon. The shading in the colour of the soil indicates the different conditions where bright brown depicts the dryer rim of the polygon, whereas darker brown indicates wet polygon centre. The heterogeneous snow cover is indicated by the dashed line. The bright red arrows indicate the individual heat flux paths at the surface and in the subsurface while the dark red arrow denotes the overall heat flux between the atmosphere and the permafrost.



3 Study site and measurement data

3.1 Study site: Samoylov Island (Lena River delta, Siberia)

The study site is located on an island in the Lena River delta in Northern Siberia about 100 km south of the Arctic Ocean at (72°22'N, 126°30'E). The Lena delta is the largest river delta at the Arctic Ocean and covers an area of about 30 000 km² surrounded by the Laptev Sea (Schwamborn et al., 2002). Figure 3.1 shows the location of the study site both on a global scale and in the regional context of the Lena delta. The site is located in the zone of continuous permafrost with a depths of about 400–600 m (Grigoriev, 1960). The eastern part of the delta, including the study site, is covered by Holocene river sediments that are present in the form of smaller islands characterized by polygonal ice wedge tundra (Schwamborn et al., 2002).

The island consists of two different landscape types that are representative for the large areas of the Lena delta and other Arctic lowlands (Boike et al., 2013). The western half of the island is occupied by a recent floodplain shaped by the annual flooding by the Lena river in spring. The eastern part of the island is covered with ice-wedge polygonal tundra and provides the landscape unit that is studied in this thesis. The deeper layers of the subsurface are made up by river sediments of different sand and silt content. They reach down to depths that are comparable to the expected permafrost thickness of several hundred metres (Schwamborn et al., 2002).

A detailed description of the site and the climatic conditions can be found in (Boike et al., 2013). The annual air temperature range is very large spanning about 65 °C from down to –45 °C in the polar night in winter to more than 20 °C in summer. The mean annual air temperature of the period since 1998 for which long term measurements are available is 12.5 °C. The mean annual precipitation is about 200 mm with a contribution of about 25 % in the form of snow during the winter months.

3.2 Measurement data

The measurement site is located in a typical network of low centred ice wedge polygons in the south-west of Samoylov island. This section gives an overview of the measurement site and the data available for the chosen modelling period. This

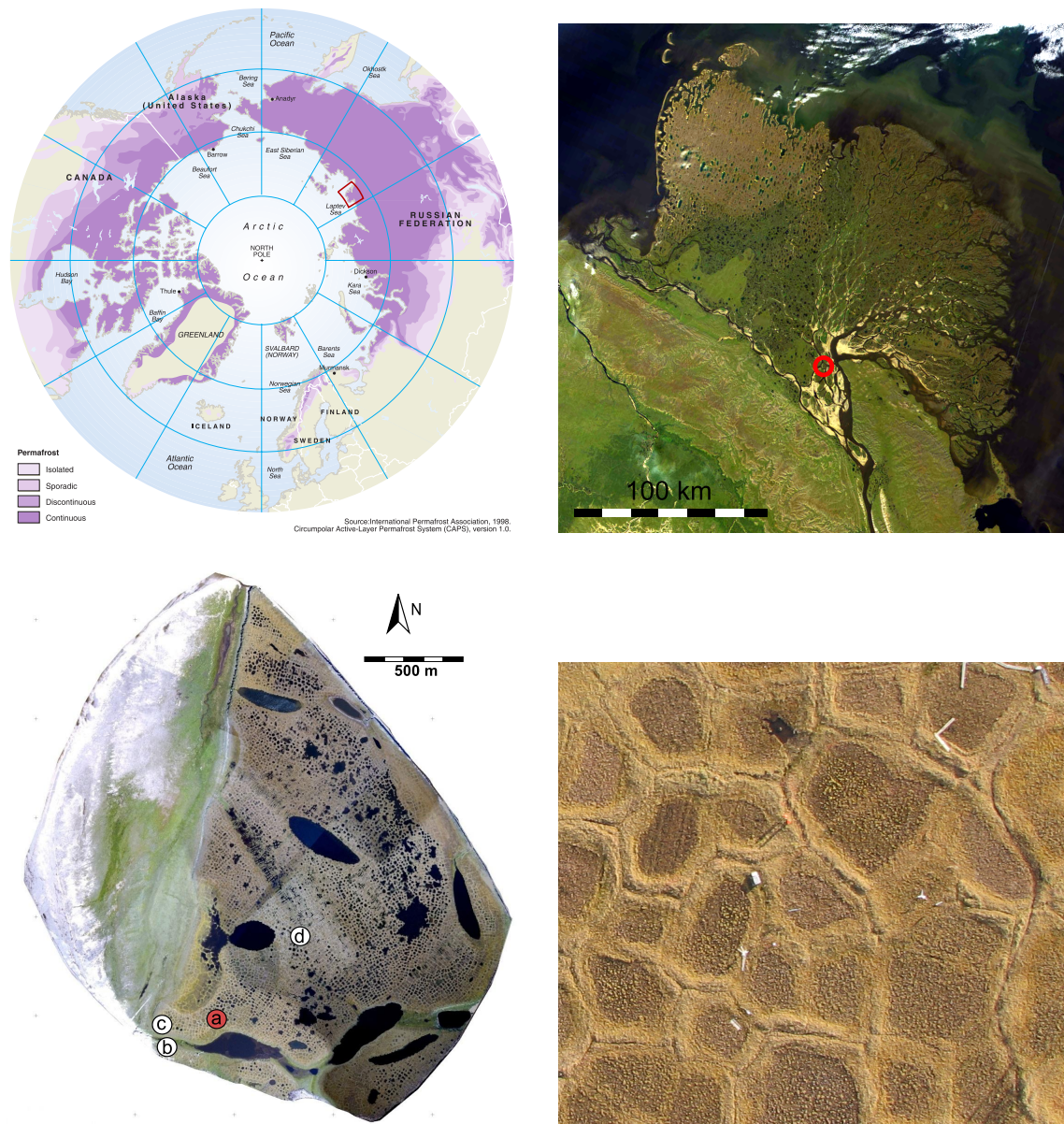


Figure 3.1: Location of the study site on different spatial scales.

Top, left: Location of the Lena River delta (red square) in a map of the distribution of permafrost in the Northern Hemisphere (Image: International Permafrost Association, based on (Brown et al., 1997)). The shades of purple depict the zones of continuous permafrost, discontinuous permafrost, sporadic, and isolated appearance of permafrost.

Top, right: Location of Samoylov island in the Lena delta (red circle), satellite image taken by NASA satellite MODIS Terra on 8 August 2012

Bottom, left: Aerial image of Samoylov Island with the location of the measurement sites used in this study. a: Primary measurement site used in this study, climate tower and soil station, b: Old research station building, c: New research station building (constructed 2011-2012), d: Eddy covariance flux tower

Bottom, right: Detailed aerial picture of the study site. The polygon with the soil monitoring station can be found in the centre of the image.

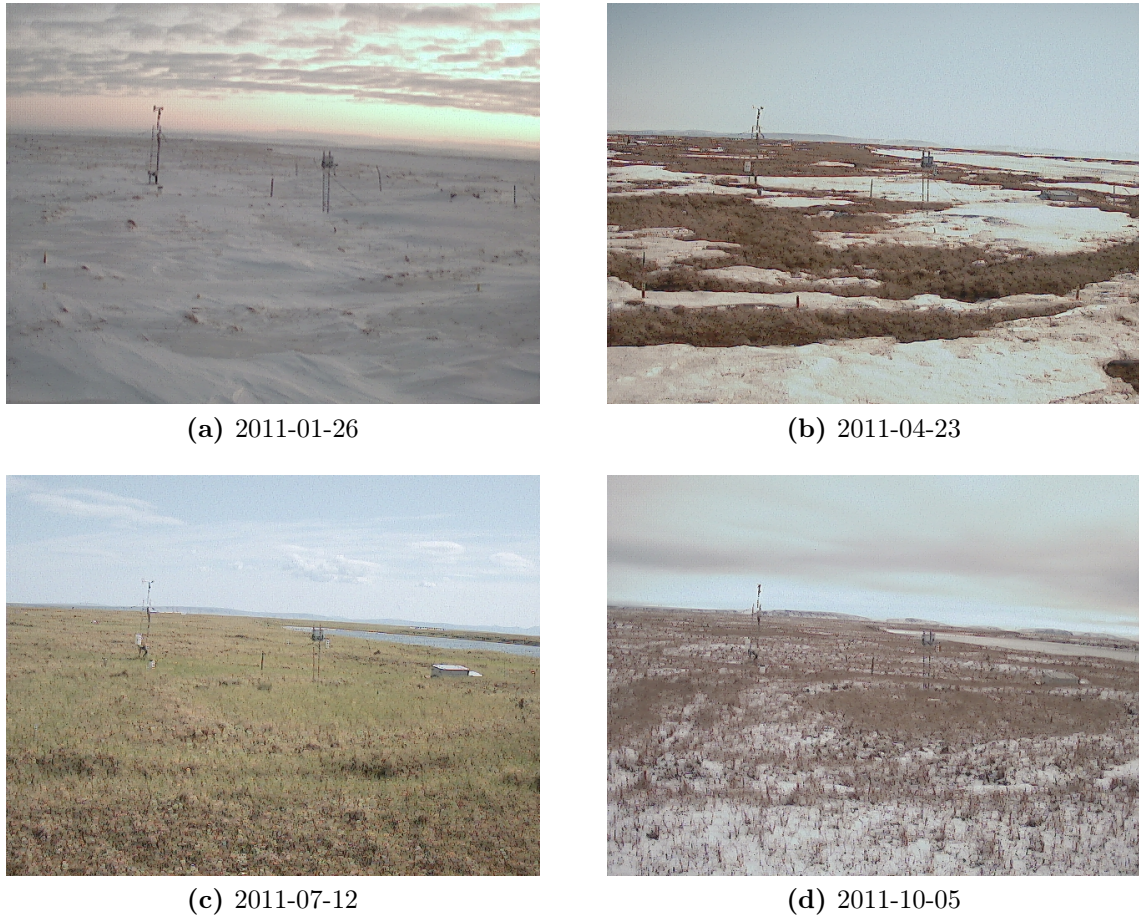


Figure 3.2: Images of the measurement site taken by an automatic camera in different seasons during the model period. *Top left:* Winter, surface fully covered with snow; *Top right:* Spring, snow melt period; *Bottom left:* Summer; *Bottom right:* Autumn, first snowfall, thin incomplete snow cover.

The polygon in the centre of the image is instrumented with three soil monitoring profiles at different positions along a transect from the centre of the polygon towards the rim (close to the aluminium box containing the datalogger and battery pack). The snow depth sensor is installed at the solar panel in the centre of the image. The climate tower and the rain gauge can be found to the left. The background shows one of the smaller lakes on the island and the Verchojansk mountain range bordering the Lena River delta to the south.

includes a short description of the measurement set-up including the different sensors. A soil monitoring station has been established in a typical tundra polygon in August 2002 (Kutzbach, 2006), accompanied with a tower for meteorological measurements. Table 3.1 summarises the installed sensors with detailed information about the sensor positions and the sensor measurement ranges and measurement accuracies. Figure 3.3 gives a schematic overview of the arrangement of the sensors installed in the subsurface of the polygon.

Figure 3.2 shows images of the soil station at four characteristic periods of the year. The images are taken by an automatic camera at 12:00 local time on each day of the year. This continuous series of images offers a good qualitative insight into the conditions at the study site in terms of the weather, the snow cover and the evolution of the vegetation.

The 2-year period from 1 August 2010 until 31 July 2012 has been chosen as the model period for this study. It offers continuous forcing and validation data without data gaps. The availability of a four-component radiation sensor during that period provides measurements of incoming solar and thermal radiation. Thus surface parameters, such as albedo and emissivity, can be taken into account in the surface energy balance calculation of the model.

Figure 3.4 shows the time series of the six input variables for the model forcing over the entire model period. In this thesis, some applications of the model require an initialisation over a longer time period. This longer spin-up data series is composed of a random combination of the two year dataset over a period of 10 years.

The following paragraphs give a short description of the measurement principles for the different physical quantities and additional information about the measurement process, such as measurement range and accuracy.

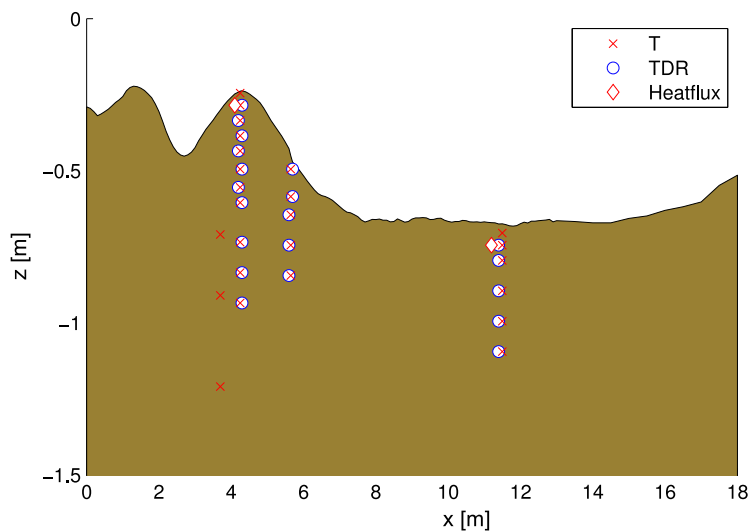


Figure 3.3: Topography and sensor positions in the instrumented polygon. The depth is given relative to a horizontal reference line that was used during installation. The sensors for temperature (red cross), soil water content (blue circle) and heat flux (red diamond) are arranged in three vertical profiles at characteristic sites in the polygon. Additionally the ice wedge under the rim of the polygon is equipped with a profile of temperature sensors.

Quantity	Sensor height / depth	Sensor	Accuracy	Measurement range
Temperature T	2 m	Campbell Sc. HMP45C	$\pm 0.2-0.5$ °C	$-39.2-60$ °C
Humidity RH	2 m	Campbell Sc. HMP45C	± 2 %	$0.8-100$ %
Wind speed u	3 m	RM Young 05305	\pm	$0-50$ m s ⁻¹
Radiation (Q_{sw} , Q_{LW})	2 m	Hukseflux NR01	10 %	$0-2000$ W m ⁻² (SW) $0-1000$ W m ⁻² (LW)
Snow depth d_{snow}	0.8 m	Campbell Sc. SR50A	± 1 cm ^a	
Surface temperature T_{surf}	30 cm	Apogee IRTS-P	± 0.3 °C	$-10-55$ °C
Soil temperature T	centre: 3,6,11,16,21,27,33 slope: 3,7,16,22,32,42 rim: 3,6,11,16,21,27,33,38,51,61,71	Campbell Scientific T107	± 0.1 °C for $T > 0$ °C ± 0.4 °C for $T = -30$ °C ^b	$-35-50$ °C
Water content $\theta_{w,liq}$	centre: 6,11,16,21,27,33 slope: 7,16,22,32,42 rim: 6,11,16,21,27,33,38,51,61,71	Campbell Scientific CS605	5-10 %	0-100 %
Soil heat flux j_z	centre: 3 rim: 3	Hukseflux HFPO1	5 % / -15 % ^c	$-2000-2000$ W m ⁻²
Soil temperature $T_{borehole}$	0-26.75 m	RBR XR-420	$-40-35$ °C	± 0.005 °C

Table 3.1: Sensors for soil physical and meteorological measurements

^aexcluding errors from the temperature correction

^beffect of the correction of temperature offset not includes (A.3)

^cin most common soils (based on 12 hour totals)

Soil temperature

The soil temperatures is measured in three profiles at characteristic positions inside the polygon, i.e. in the centre of the polygon, at the top of the rim of the polygon and at the slope in between these two compartments. The measurements are performed with thermistor based temperature probes (Campbell Scientific T107). The sensors are installed down to the base of the active layer, which is up to 42 cm in the centre and at the slope of the polygon and 71 cm below the rim of the polygon. During the time that they are installed in the ground, the temperature sensors show a drift in the measurement values. This offset must be corrected to yield the appropriate accuracy in the physically most important temperature range around 0 °C. The correction is described in detail in appendix A.3.

The ice-wedge below the rim of the polygon and the crack towards the next polygon is equipped with an additional chain of temperature sensors.

Liquid water content (TDR)

The liquid water content in the soil is measured by Time Domain Reflectometry (TDR) with Campbell Scientific CS605 probes. The measurement principle is based on the determination of dielectric permittivity of the soil, based on the runtime of an reflected electromagnetic pulse in a wave-guide in the soil. Since the dielectric constant of water is much larger than that of the other soil constituents, the measurement this allows for the determination of the liquid water content. The data processing has been performed according to (Roth et al., 1990). The TDR-probes are always installed a few cm next to a soil temperature sensor to include temperature dependences in the data evaluation.

Soil heat flux

The two profiles at the centre and at the rim of the polygon are equipped with Huxeflux HFP01 heat-flux plates at a depth of 7 cm below the soil surface. These devices measure the conductive heat flux in the soil based on the temperature difference between the two sides of a horizontal plastic plate. The plate has a diameter of 80 mm and is 5 mm thick. The thermal resistance of the heat flux plate is $6.25 \cdot 10^{-3} \text{ K m}^2 \text{ W}^{-1}$, which is equivalent to a thermal conductivity of $0.8 \text{ W K}^{-1} \text{ m}^{-1}$ for the given sensor thickness. This value is in the range of typical thermal conductivities of unfrozen soils, but only half of thermal conductivities of ice rich frozen soils (Williams and Smith, 1989).

Surface temperature

The surface temperature is measured at one location above the soil profile in the rim of the polygon. The measurement is based on the infrared radiation emitted from the soil surface corrected for the temperature of the sensor body. However, the sensor (Apogee IRTS-P) is only expected to give reasonable data for temperatures

above the minimum value of the calibration curve at -10°C . Hence, the data do not allow for an investigation of wintertime snow surface temperature.

Snow depth

A Campbell Scientific SR50A ultrasonic distance sensor mounted to a pole in the centre of the polygon provides the measurement of snow depth in the polygon used throughout this thesis. A raw distance value is obtained from the runtime of ultrasonic pulses and then corrected for the temperature dependency of the sound speed in air based on the measured air temperature. The snow depth is, however, a quantity that is highly variable due to the microtopography of the study site. This is clearly visible in three of the images in Figure 3.2, that show both partial snow cover and the complete snow cover shaped by wind drift processes. Still, this heterogeneity is not directly measured. The snow depth reaches a maximum of 18 cm in the first winter and 16 cm in the second winter of the modelling period. That is distinctly lower than the average maximum snow depth during previous years when values of up to 50 cm were measured in the polygon centres (Boike et al., 2013; Langer et al., 2011b).

Radiation

The radiation budget is measured by a four-component radiation sensor (Hukseflux NR01). Both incoming and outgoing radiation is measured in the short-wave band 350–2800 nm and in a thermal band 4.5–50 μm . The measurement principle is based on the absorption of the radiation on thermopile sensors. The sensitivity to the spectral bands is achieved by the choice of the material of the sensor windows (glass/silicon). In the far infrared sensors, the signal is automatically corrected for the sensor temperature.

The measurement of the outgoing long-wave radiation $Q_{\text{LW},\text{out}}$ can be used to obtain a reliable value for the surface temperature T_{surf} according to equation (2.4).

Air temperature and relative humidity

The air temperature and the relative humidity are measured with a combined sensor (HMP45). The temperature is measured with a platinum resistance thermometer (PRT), while the relative humidity is detected based on the effect of humidity on the dielectric properties of a polymer. For these two quantities, data measured at the eddy covariance tower at a distance of about 500 m from the soil monitoring station is used.

The mean air temperature during the modelling period is 11.1°C with maximum temperatures of 25.2°C . The minimum measured temperature corresponds to the lower range of the temperature sensors, which means that there were temperatures below -39.8°C during the model period that are not represented in the data. However, these situations are restricted to a few cold nights during February and March of both years. Therefore, a strong effect on the thermal dynamics of the system is

not expected.

Wind speed

The wind speed and the wind direction are measured at the climate tower at a measurement height of 3 m. Wind directions are not taken into account for this thesis since the landscape is rather homogeneous on a scale larger than the polygonal soil structures around the study site. The mean wind speed over the model period is 4.3 m s^{-1} . Maximum values of up to 17 m s^{-1} are only reached during short stormy periods. Windless periods characterised by wind speeds of less than 0.5 m s^{-1} require a special treatment in the model simulations. However, this affects only 3% of the total model period, mainly during late winter in February and March.

Soil temperature (borehole)

A borehole with temperature sensors provides temperature measurement in larger depth in the permafrost to complement the detailed temperature measurements in the active layer. The borehole is located under the rim of a typical polygon comparable to the principal measurement site in the same landscape unit at a distance of about 150 m.

Soil scientific measurements and classifications

During the set-up of the soil monitoring station in summer 2002, a transect through the polygon has been dug for the horizontal installation of the measurement sensors. At the same time a soil scientific study of the subsurface was performed that is described in detail in Kutzbach (2006). This includes the identification and characterisations of the different soil horizons. Furthermore soil samples were taken for each of the soil layers and analysed for their physical, chemical and biological characteristics. For this study the relevant parameters are porosity, and the content of mineral and organic material that are used for calculation of the soil thermal properties in the numerical model.

Freezing characteristics

The pairing of the temperature sensors and the TDR probes close to each other in the soil profiles allows for the determination of the freezing characteristics of the soil at these measurement points. Figures A.1 - A.3 show the respective plots for all pairs of sensors in the three soil profiles in the polygon. The freezing and thawing branches of the relationship show a distinctly different shape for most of the sensors. The freezing branch generally shows a smooth curve for the liquid water content that follows the expected freezing characteristics. Liquid water content reaches the value of total water content value at a temperature of $0 \text{ }^\circ\text{C}$. The curve describing the thawing front in this plot, however is characterised by a strongly varying curve that shows positive temperatures long before the liquid water content reaches the

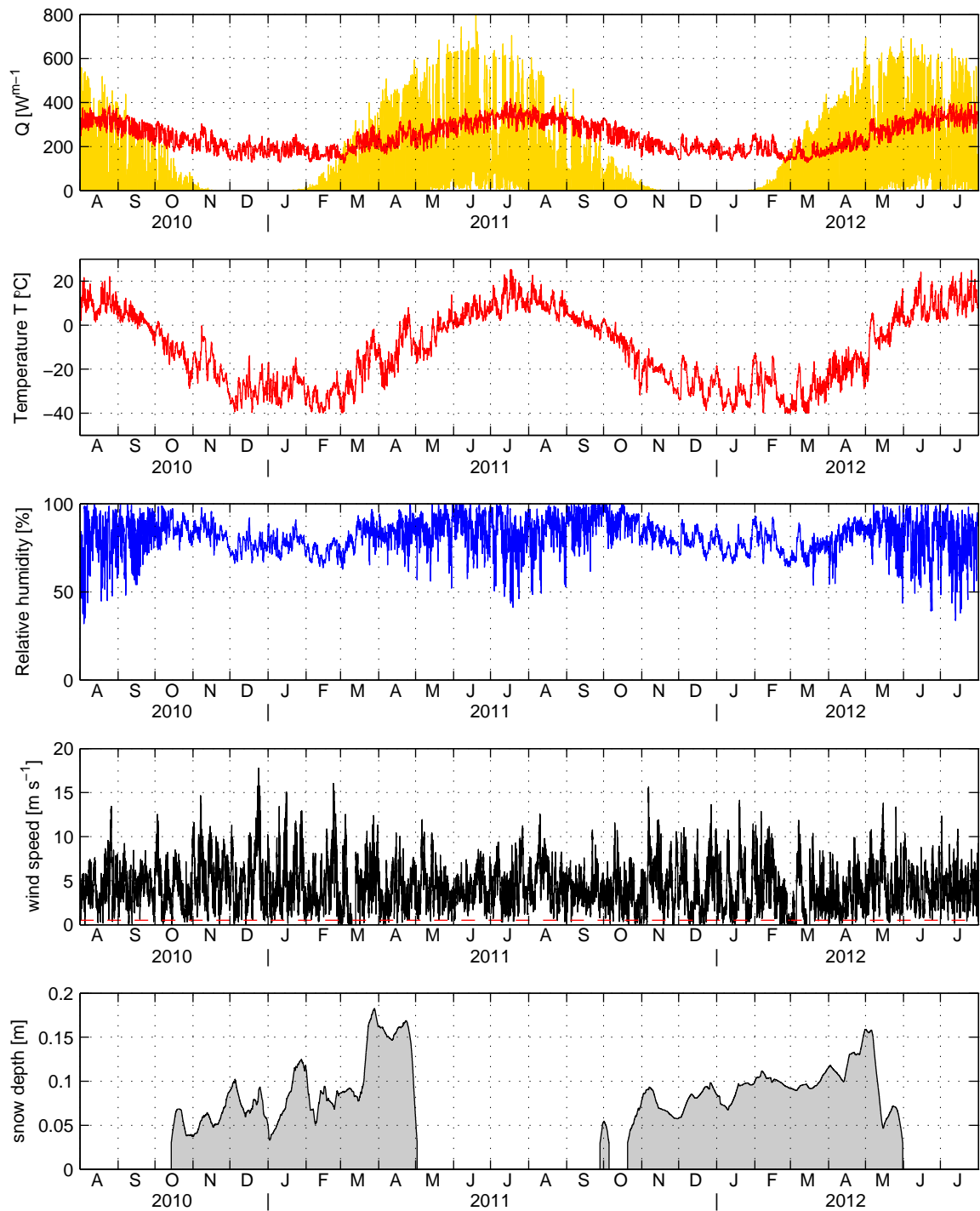


Figure 3.4: Two year forcing data series used for all simulations with surface energy balance forcing in this thesis. From top to the bottom: Incoming short-wave and long-wave radiation, air temperature in 2 m height, relative humidity in 2 m height, wind speed measured in 3 m height (the red line shows the minimum wind speed used in the model calculations), snow depth in the centre of the polygon

plateau value of the summer months. This difference has been investigated in detail by Ludin (2010) for the same measurement set-up as described in this Chapter in an earlier study. It was concluded that the difference in the shape can be attributed to the different characteristics of the thawing and freezing period in the soil (see Chapter 2.4). The thawing period is characterised by a sharp front penetrating into the soil. This can lead to the situation that the temperature sensor and the TDR probe are found in distinctly different soil conditions. i.e. at different sides of the sharp thawing front, despite the small lateral distance of only a few cm between the two sensors. In contrast, the freezing process is dominated by the zero-curtain regime and the isothermal plateau, which leads to small temperature gradients and slow phase change processes. Thus, the freezing characteristics is represented well despite the lateral distance between the sensors. Therefore, only the freezing branch of the soil freezing characteristic should be taken into account in the determination of the parameters describing the empirical freezing curve.

4 Model description

The numerical model used in this study is based on an established permafrost model that has been applied successfully in several studies (Westermann et al., 2011; Langer et al., 2013; Westermann et al., 2013). The basic version contains the description of conductive heat transfer and phase change in the soil along with a dynamic snow layer of constant physical properties.

In this thesis, the model is extended to simulate the thermal dynamics in the laterally heterogeneous landscape units of the tundra polygons:

- (i) A surface energy balance calculation scheme is coupled to the soil model, which allows for a forcing of the model with meteorological data and a variation of the surface parameters in the different parts of the polygon.
- (ii) A two dimensional formulation of the model in cylindrical coordinates is developed. This allows for the explicit calculation of the lateral heat transfer processes inside the tundra polygons. This involves the representation of the microtopography and changes to the description of the snow cover in the model.
- (iii) The numerical solution of the differential equation is implemented using a first order Euler-scheme with adaptive time-stepping according to two different stability criteria.

This chapter displays the computational implementation of the model based on the theoretical basis given in Chapter 2. A short description of the existing modelling scheme is given. The main extensions to the model implemented in this work are outlined in more details along with the model setup for the specific conditions at the study site.

4.1 The basic model formulation

The soil thermal parameters in the model are calculated based on the composition of the soil from the four components water content θ_w , mineral content θ_{min} , organic content θ_{org} and air content θ_{air}

$$\sum_i \theta_i = \theta_w + \theta_{min} + \theta_{org} + \theta_{air} = 1. \quad (4.1)$$

The total water content, the mineral content and the organic content are set for each grid cell. In practice this is done by interpolation between grid points of known or assumed soil composition. The two phases of the soil matrix θ_{min} and θ_{org} are

constant in time for each grid cell. The total water content is also kept constant as the sum of liquid water content and ice content while the air content results as the residuum to unity. The temperature dependency of the thermal properties is modelled in the temperature range between $T_f = -10^\circ\text{C}$ and $T_{th} = 0^\circ\text{C}$, where the soil is completely thawed. This temperature range is discretised in temperature steps of 0.01 K. For each grid cell and each temperature steps both effective heat capacity and heat conductivity are calculated in the initialisation process.

The soil freezing characteristic is represented by an empirical function which gives the liquid water content of the soil depending on the soil temperature. In this study the formulation is based on the total water content θ_w , the minimal liquid water content $\theta_{w,\min}$ and a polynomial of second order in temperature determined by two coefficients a and b

$$\theta_{w, \text{liq}} = \begin{cases} \theta_{w,\min} & \text{for } T \leq T_f \\ \theta_{w,\min} + \frac{\theta_w - \theta_{w,\min}}{1 - aT + bT^2} & \text{for } T_f < T < T_{th} \\ \theta_w & \text{for } T \geq T_{th}. \end{cases} \quad (4.2)$$

The effective heat capacity of each soil cell is calculated as the weighted mean of the volumetric heat capacities of the components

$$c(T) = \sum_i \theta_i(T) c_i, \quad (4.3)$$

which includes the variation of the liquid water and ice content with temperature according to equation (4.2). The heat conductivity of the soil is calculated based on the model by de Vries described in Chapter 2.2. The temperature dependencies of the heat capacities and thermal conductivities of the soil constituents are neglected due to the small variations of these properties compared to the variations that occur due to the phase change of water. The effective heat capacity is dominated by the latent energy exchange that is several magnitudes larger than the volumetric heat capacity of the soil constituents.

The resulting matrices are used as a lookup and are calculated once in the initialization of the model. This avoids the computational effort of calculating the material properties in each time step during the model calculation. The value for the effective capacity and thermal conductivity is chosen for each single model cell according to the soil temperature at that time.

The numerical model is solved using a finite differences scheme. The model features a main grid z on which the soil temperature and the effective heat capacity are calculated and a second grid z_k at the interfaces of the soil cells where the heat conductivity is needed in the calculation scheme.

The grid resolution is not uniform, but decreasing with depth. A grid size of 1 cm to 2 cm is used in the snow layer and the uppermost soil layer. Hence, the dynamic processes of snow cover built-up and snow melt as well as freezing and thawing of

the soil are calculated with the right accuracy. Furthermore this allows for a detailed representation of the microtopography in the two-dimensional model configuration. Towards greater depths the resolution can be increased in a quasi-logarithmic way to save calculation efforts, as the thermal dynamics in the deeper layers are not very dynamic, especially as the model is initialized with a steady-state temperature profile.

The cells of the model domain can be either treated as "soil", "snow" or "air", which allows to include a dynamic snow cover in the model. This approach is displayed schematically in Figure 4.3 for the two-dimensional case. The position of the soil surface is set in the initialisation and kept fixed for the whole modelling period. All cells below that interface (topography) are soil cells with thermal properties set during the initialisation. The changing snow depth introduces another interface position. All cells above that interface (surface (SEB)) are ignored in the calculation whereas the cells between the two interface are treated as snow with uniform thermal properties. For periods without snow cover, the position of two interfaces is identical, leading to a direct soil-atmosphere interface.

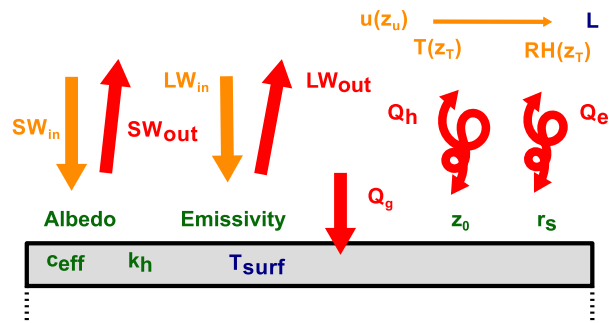
4.2 Surface energy balance model

The surface energy balance model is implemented according to the theoretical background given in Chapters 2.1 and 2.3. The surface temperature T_0 and the ground heat flux Q_g provide the coupling between the surface energy balance model and the soil heat transfer model. Figure 4.1 gives a schematic overview of the model calculations.

The surface energy balance is calculated in each time step based on the temperature of the uppermost soil or snow cell and the atmospheric forcing that is provided by the set of meteorological measurements described in Chapter 3.2. This includes air temperature, relative humidity, wind speed and incoming radiation in the short-wave as well as in the thermal long-wave band. The input data is given with a resolution of 30 min. For each time step the forcing is linearly interpolated to the model time from the two neighbouring input time steps.

The radiation balance is calculated from the incoming radiation components accord-

Figure 4.1: Schematic overview of the surface energy balance scheme used in the model. The colours indicate whether a certain quantity is given by the model forcing (orange), set as a parameter in the initialisation (green), taken from the last time-step (blue) or calculated in the surface energy balance model (red)



ing to the surface parameters albedo A and emissivity ϵ . For a snow covered surface the albedo strongly increases. In this study, a value of $A_{\text{snow}} = 0.8$ (Weller, 1972) is set for all snow-covered periods.

To simulate the turbulent fluxes of sensible and latent heat the friction velocity u_* is calculated according to equation (2.32) based on the current wind speed u and the stability condition calculated in the last time step.

The surface energy balance scheme tends to produce unreliable heat fluxes for windless periods (Martin and Lejeune, 1998; Brun et al., 1989). Thus, the forcing wind speed is set to a minimum of $u_{\text{min}} = 0.5$ in case that the measured wind speed is below that threshold. This only applies to 3% of the modelling period.

The turbulent fluxes of sensible and latent heat are calculated according to equations (2.33) and (2.34). The surface temperature T_0 in this calculation is given by the temperature of the uppermost soil cell in the last time step at $t = t_{i-1}$. The atmospheric stability is given by Monin-Obhukov length L which is calculated from the heat fluxes in the previous time step according to equation (2.28). For the universal functions the formulation by Högström (1988) is used under unstable conditions ($\zeta < 0$)

$$\varphi_m = (1 + 19.3\zeta)^{-1/4} \quad (4.4)$$

$$\varphi_h = 0.95((1 - 11.6\zeta)^{\frac{1}{2}}). \quad (4.5)$$

Under stable conditions ($\zeta > 0$) the modified formulations according to (Grachev et al., 2007) are used, because these better reflect the atmospheric conditions under Arctic conditions, especially during the polar night (Grachev et al., 2007; Westermann, 2010)

$$\varphi_m = 1 + \frac{6.5\zeta(1 + \zeta)^{1/3}}{1.3 + \zeta} \quad (4.6)$$

$$\varphi_h = 1 + \frac{5\zeta(1 + \zeta)}{1 + 3\zeta + \zeta^2}. \quad (4.7)$$

In the numerical calculation, the integrated forms of these universal functions are used to avoid the calculations of the integrals during model runtime. They are given explicitly in the Appendix A.1.

According to equation (2.1) the ground heat flux is calculated as the residuum of the three other surface energy balance components

$$Q_g = Q_{\text{net}} - Q_h - Q_e. \quad (4.8)$$

acting as a source term in the uppermost soil or snow cell.

The thickness of the dynamic snow cover is controlled by three different processes, snow fall, sublimation and melting. In the model, the snow is internally described by the snow water equivalent (SWE) rather than the snow depth, as SWE is the relevant quantity for the latent energy stored in the frozen water of the snow layer.

The built-up of the snow is simulated based on a snowfall rate. In the present study, this snow fall rate is derived as the slope of the measurements of the snow depth itself, as this is the only available measurement of the snow cover at the study site. The snow cover is reduced by sublimation at the snow surface and melt processes in the entire snow layer. Snow sublimation results directly from the latent heat fluxes in the surface energy balance calculation

$$\Delta\text{SWE}_{\text{subl}} = \frac{Q_e}{(L_{\text{sl}} + L_{\text{lv}})\rho_w}. \quad (4.9)$$

Snow melt is calculated for each snow cell separately as soon as the temperature in the cell would reach a value above 0 °C in the model calculations. In this case, the temperature of this cell is kept at the freezing point while the energy difference is converted into the corresponding snow water equivalent

$$\Delta\text{SWE}_{\text{melt}} = \frac{\Delta E}{L_{\text{sl}}} = \frac{c_{\text{snow}}T}{L_{\text{sl}}}. \quad (4.10)$$

The changes of the snow water equivalent due to these three processes are converted to a snow depth change and accumulated over all snow cells in a column. As soon as the change sums up to the equivalent of a grid cell, the snow cover is reduced or increased accordingly.

4.3 Two-dimensional model formulation in cylindrical coordinates

The model description of the thermal dynamics inside a typical tundra polygon is supposed to incorporate the main features of the system, which are given by the strong differences between the centre and the rim of the polygon, while keeping the simplest possible model description. The aerial picture of the study site (Figure 3.2) reveals that the assumption of nearly circular shape is appropriate for most of the polygons around the instrumented site. Although some of the polygons may deviate from the assumed circular shape, the general shape is still given by a strong radial gradient in the surface cover. The same spatial pattern can also be expected for the subsurface structure of the landscape due to the underlying process of polygon formation (Lachenbruch, 1962). Therefore the thermal heat transfer inside a single polygon can be described in cylindrical coordinates under the assumption of radial symmetry which implies the following limitations and assumptions:

- The polygons can be treated as approximately round.
- The soil and surface parameters in the polygons only vary with depth and distance to the centre. There are no variations in angular direction.

- All heat transfer processes in the polygon only have vertical and radial components. There is no heat transfer in angular direction.

This system allows for a formulation of the heat transfer equation (2.16) in cylindrical coordinates with all dependencies on the angular direction neglected

$$c_{\text{eff}}(r, z, T) \frac{\partial T}{\partial t} = \frac{\partial}{\partial z} \left(k_h(z, r, T) \frac{\partial T}{\partial z} \right) + \frac{1}{r} \frac{\partial}{\partial r} \left(r k_h(z, r, T) \frac{\partial T}{\partial r} \right). \quad (4.11)$$

The heat transfer processes is thus simulated in the three-dimensional cylindrical model domain with an effectively two-dimensional numerical model. A three-dimensional description of the problem would drastically increase the number of nodes in the numerical discretisation, both inside the soil and at the surface which would lead to a very long model runtime applying the necessary spatial resolution. Furthermore, detailed information about the system is only available on a transect through the polygon. This includes both the measurements of soil temperature and soil water content as the description of the soil composition. This essentially limits the validity of the model simulation to the radially symmetric case.

The calculation in cylindrical coordinates takes into account both the actual dimensions and the appropriate volumes in the polygon. This leads to a realistic simulation of heat transfer, which is not the case in a linear two-dimensional model description along a transect thorough one or more polygons. Assuming zero heat flux between neighbouring polygons, the entire landscape can be stitched together from these cylindrical model polygons. A theoretical coverage of up to 90% ($\pi/\sqrt{12}$) (Rogers, 1958) of the surface in an idealised packing is achieved for polygons of equal size. Thus, the average soil and surface parameters as well as the average vertical fluxes obtained for one polygon can be seen as a good approximation of the average over larger landscape.

The cylindrical model domain is discretised in both vertical and radial direction for the numerical solution of the differential equation with a finite differences scheme. The model domain is made up by soil cells in the shape of rings. The resolution in the vertical direction is chosen vertically decreasing as in the one-dimensional case. In the radial direction a coarser resolution of 10 cm is justified because the freezing and thawing front can be expected to propagate nearly vertically due to the forcing from the soil surface.

The model grid consists of a main grid (z, x) placed at the centre of these rings for the temperature and the effective heat capacity. Two additional grids for the heat conductivities (z_k, x) (z, x_k) are placed on the vertical and radial interfaces of the soil cells. Figure 4.2 shows a schematic description of the spatial discretisation for the one-dimensional model and for the two dimensional model version.

The conductive heat fluxes are calculated from the temperature gradient between the adjacent soil cells, the thermal conductivities and the area of the interfaces

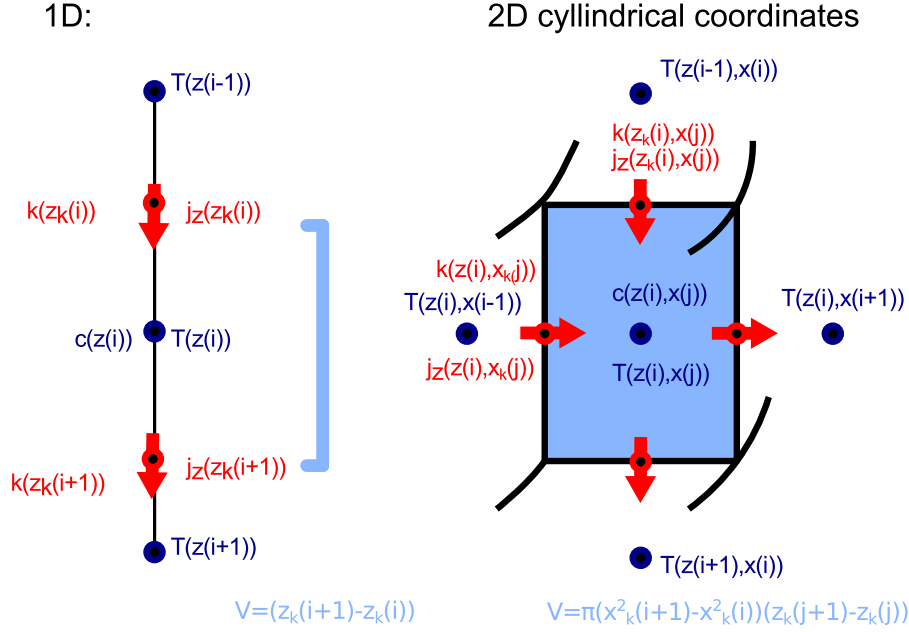


Figure 4.2: Model discretisation in the one-dimensional model (left) and in the two-dimensional model in cylindrical coordinates (right). The blue colour denotes quantities that are calculated on the main grid, such as temperature and heat capacity. The red colours stand for the variables in the additional grids such as thermal conductivity and the heat fluxes between the soil cells. The model cell in the two-dimensional model have the shape of complete rings, only a fraction of such a ring is displayed here.

between two model cells .

$$j_z(z_k(i), x(j)) = -k(z_k(i), x(j))(\pi(x_k^2(j) - x_k^2(j-1))) \frac{T(z(i), x(j)) - T(z(i-1), x(j))}{z(i) - z(i-1)} \quad (4.12)$$

$$j_r(z(i), x_k(j)) = -k(z(i), x_k(j))2\pi(x_k(j)) \frac{T(z(i), x(j)) - T(z(i), x(j-1))}{x(j) - x(j-1)}. \quad (4.13)$$

The volume of the model cell

$$V(i, j) = \pi(x_k^2(j+1) - x_k^2(j)) \cdot (z(i+1) - z(i)) \quad (4.14)$$

is taken into account for the effective heat capacity in equation (4.16).

Snow cover and microtopography

The implementation of the pronounced microtopography in the model makes use of the scheme that has been introduced to describe the dynamic snow layer in the

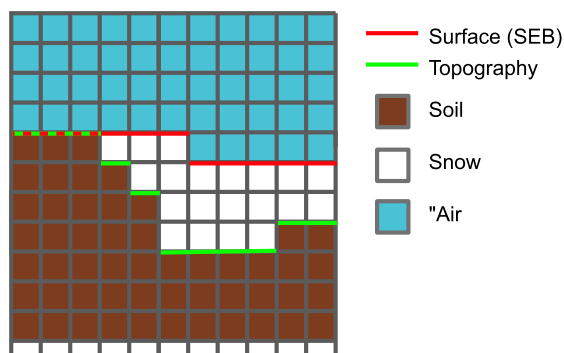


Figure 4.3: Schematic depiction of the scheme used for the description of the snow cover and surface topography. Each snow cell is set to one of the three states soil, snow or air. This is based on the position of the two interfaces at the ground surface (topography) or at the surface to the atmosphere (surface (SEB)), where the surface energy balance is calculated. The interface describing the surface topography is kept fixed for the whole model run, the snow surface can change dynamically

one-dimensional model. The position of the interface between the soil and the air or snow cells for each soil column is set in the initialisation and kept fixed throughout the entire modelling period. The vertical resolution of 2 cm in this part of the model domain allows for a smooth representation of the surface topography. The snow cover development is simulated separately for each ring-shaped part of the model domain, which makes it possible to account for a heterogeneous snow cover. Lateral and vertical conductive heat fluxes are calculated between neighbouring snow cells. Wind-drift is a very important process at the study site which dominates the build-up of the snow cover (Boike et al., 2013). Together with the pronounced microtopography this leads to strong heterogeneities in the snow depth with high snow cover in the centres of the polygons and thin snow cover on the polygonal rims. In the two dimensional model, this process is included in a simple approach preventing the snow cover on the elevated rims from exceeding a threshold snow depth d_{th} . This value is set to 4 cm, which equals two cells of snow in most simulations. The same threshold value for the snow depth is applied in the one-dimensional simulations for the rim of the polygon.

Surface energy balance

In the two-dimensional model configuration, the surface energy balance is calculated for each surface cell separately according to the surface properties and the current surface temperature of the cell. However, the atmospheric stability conditions have to be derived for the entire model surface because it cannot be defined as a local property at the scale of the horizontal resolution of the model. This is based on the assumption that the average over the simulated polygon can be used as a good approximation of the average over a larger surface area. The surface temperature and the turbulent heat fluxes are averaged over the entire circular surface of the

modelling domain with a weighted averaging according to

$$\langle a \rangle_{\text{radial}} = \frac{\sum_{i=m}^n a_i A_i}{A_{\text{tot}}}, \quad (4.15)$$

where a is the averaged variable, A_i is the surface area of the respective ring and A_{tot} denotes the surface area of the entire model domain. These averaged properties are used to calculate the Monin-Obhukov-length L that is used for the surface energy balance calculation in the following time step.

4.4 Numerical solution

The model is implemented in the numerical software Matlab (The Mathworks, USA). The version Matlab R2013a has been used for all calculations presented in this thesis. The partial differential equation is discretised in space to obtain a set of ordinary differential equations in time. In this thesis the solution of the ODE is obtained using an explicit Euler-Integration scheme of first order accuracy with adaptive time-stepping.

For each time step the temperature field is updated according to:

$$T = T + \frac{1}{c_{\text{eff}}(T)} \frac{dE}{dt} \Delta t. \quad (4.16)$$

The rate of energy change dE/dt of each cell is given by the sum of all energy fluxes at the boundaries, i.e. conductive heat fluxes according to equations (4.12) and (4.13) as well as boundary fluxes. In the snow cells this also includes the energy transformed in the melting of snow as a source term.

The time step has to be chosen small enough to ensure both the stability of the numerical solution scheme and the accuracy in the calculation of the freezing and thawing of the soil water content. The CFL-condition (Courant-Friedrichs-Levy) (Courant et al., 1928) is a necessary condition for the stability of a finite difference solution scheme. The Courant number μ has to be smaller than some critical value μ_{crit} , that is dependent on the solution scheme and depends on the grid spacing Δx , the time step Δt and the velocity u at which a front can propagate in the system

$$\mu = u \frac{\Delta t}{\Delta x}. \quad (4.17)$$

In the case of the heat transfer equation solved in this model, the characteristic velocity can be calculated from the heat diffusivity $D_h = \frac{c_h}{\rho k_h}$ and the grid spacing Δx to $u = D_h/\Delta x$, so that the Courant number reads

$$\mu = D_h \frac{\Delta t}{(\Delta x)^2}. \quad (4.18)$$

For the Euler-scheme used in this thesis the Courant number is set to 1/2. This means that a front in the system can only move by less than half a grid spacing during one time step to prevent instability. Thus, the maximum time step is

$$\Delta t \leq \frac{1}{2} \frac{1}{D_h} (\Delta x)^2. \quad (4.19)$$

and

$$\Delta t \leq \frac{1}{2} \frac{1}{D_h} \frac{1}{1/(\Delta x)^2 + 1/(\Delta y)^2} \quad (4.20)$$

in the two-dimensional simulations. As the grid spacing in lateral direction is always chosen about a magnitude coarser than the vertical one, the time stepping is mainly determined by the resolution of the vertical grid.

Short time steps are necessary during periods in which soil cells with a high spatial grid resolution show a high thermal diffusivity. This is the case for the completely frozen soil cells in the upper soil layer with both small grid spacings and a high conductivity resulting in a high thermal diffusivity.

In the periods of freezing and thawing, the effective thermal capacity is high which leads to a low thermal diffusivity. Hence, freezing and thawing soil cells are not critical for the numerical stability of the solution scheme. During these periods, however, the change in the inner energy of each cell is determined by the phase change of water which is included in the model in the form of the freezing curve. The time steps have to be chosen small enough to represent the changes the effective heat capacity with temperature and avoid violations of the energy conservation in the model. This applies mainly to the end of the freezing curve at the transition to the completely thawed soil around 0 °C, where the liquid water content changes strongly with temperature. Thus, a maximum energy change in each time step is set to

$$\Delta t \frac{\partial E}{\partial t} \leq \Delta E_{th}, \quad (4.21)$$

where $\Delta E_{th} = 200 \text{ kJ m}^{-2} = c_{h,water} \Delta T_{th}$ corresponds to the energy that is needed to warm pure water by $\Delta T_{th} = 0.05 \text{ °C}$. For a vertical resolution of $\Delta z = 2 \text{ cm}$ in the uppermost soil layer, the time steps calculated according to these criteria are in the range of 20–200 s for most of the model period. The maximum time step of the model is set to 300 s independently from the calculations above.

4.5 Model set-up

Soil composition and initial temperature field

In this study, the measured soil temperatures and soil water contents at the soil profiles are used to determine the total water content and the residual water content

	heat capacity c_h [$\text{J m}^{-3} \text{K}^{-1}$]	thermal conductivity k_h [$\text{W m}^{-1} \text{K}^{-1}$]	density ρ [kg m^{-3}]
water	$4.188 \cdot 10^6$	0.57	1000
ice	$2.117 \cdot 10^6$	2.2	-
mineral material	$2 \cdot 10^6$	2.9	-
organic material	$2.5 \cdot 10^6$	0.25	-
air	$1.25 \cdot 10^3$	0.025	-
snow	$1.016 \cdot 10^6$	0.11	243

Table 4.1: Thermal properties of the materials in the model according to Hillel (1982) for the soil constituents and Langer et al. (2013) for snow.

at low temperatures. The measured soil freezing characteristics for all sensors are shown in Figures A.1 - A.3 for the three soil profiles in the polygon. The parameters $a = 19$ and $b = 4$ describing the shape of the freezing curve have been chosen equal for the whole modelling domain according to the values obtained by (Langer et al., 2011b). This is justified as the curves are in sufficient accordance with the measured relationship. The uppermost sensor in the polygon centre is the only sensor that shows a distinct difference in water content between the two summers. All other sensors show a stable plateau in the water content as the soil is completely thawed, which supports the assumption of constant total water content in the soil. The soil survey performed during the set-up of the soil monitoring station (Kutzbach, 2006) is used to set the porosity, the mineral content and organic content at the different depths in the instrumented soil profiles. A soil core taken close to the study site shows a soil composition of about 50 % ice and 50 % mineral material in depths of up to 4 m. The deeper sediment layers represent the river sediments with 20 % ice or water and 80 % mineral material (Langer et al., 2013). From these points, all soil parameters are interpolated linearly to the model grid. Table 4.1 gives the physical properties of the soil constituents a used in the model. The thermal properties of the soil constituents are chosen according to (Hillel, 1982) and are displayed in Table 4.1. The thermal properties of the snow are based in a Monte-Carlo analysis of the snow cover performed for the same study site in Langer et al. (2013). The surface properties for the centre and for the rim of the polygon as well as for the snow cover are given in Table 4.2. These parameters are based on earlier studies at the study site (Kutzbach, 2006; Langer et al., 2011a,b; Kattenstroth, 2009) and literature values for tundra landscapes and snow (Weller, 1972; Weller and Holmgren, 1974).

The initial temperature distribution in the soil is calculated based on the available temperature measurements described in detail in Chapter 3.2. This includes the three temperature profiles up to a depth of 42 cm (centre/slope) and 71 cm (rim) and temperature measurements in a nearby borehole up to a depth of 27 m. For the soil below the lowest sensor of the borehole, the initial temperature is based on the assumption of a steady state according to the geothermal gradient. The lower boundary of the model domain is set at a depth of 1000 m, where a constant heat

Surface parameter	centre	rim	snow
Albedo A	0.15	0.2	0.8
Emissivity ϵ	0.95	0.95	0.95
Roughness length z_0 [m]	0.05	0.02	5e-4
Surface resistance r_s [m/s]	50	100	0

Table 4.2: Surface parameters for the surface energy balance calculations for the three surface types considered in the model (centre of the polygon, rim of the polygon, snow)

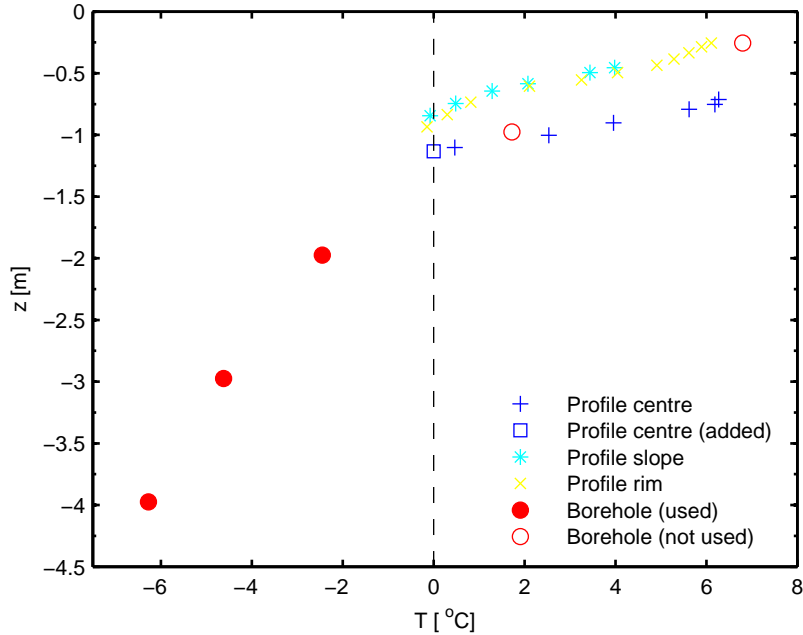


Figure 4.4: Soil temperature at the three profiles in the polygon along with the temperature of the uppermost borehole sensors at the beginning of the modelling period on 1 August 2010. The initial temperature distribution is obtained from a linear interpolation of these values. For the profile at the polygon centre an additional point (blue square) has been added manually at the temperature of 0 °C based on a linear interpolation of the temperature gradient in the unfrozen soil to avoid overestimation of the thaw depth

flux equivalent to the geothermal heat flux can be assumed. A world heat flow data set (Pollack et al., 1993) gives a value of $Q_{\text{geo}} = -0.053 \text{ W m}^{-2}$ for a deep borehole in Tiksi, about 120 km south-east of the study site. This value is chosen for the study site, assuming comparable geological conditions.

At the beginning of the modelling period on 1 August 2010, the deepest sensors of the temperature profiles at the rim and at the slope of the polygon are still in frozen ground. These profiles do not cause a problem for the interpolation of the initial temperature field, since the thaw depth can be confined between two soil temperature sensors. In the polygon centre, however, the deepest sensor is already in thawed

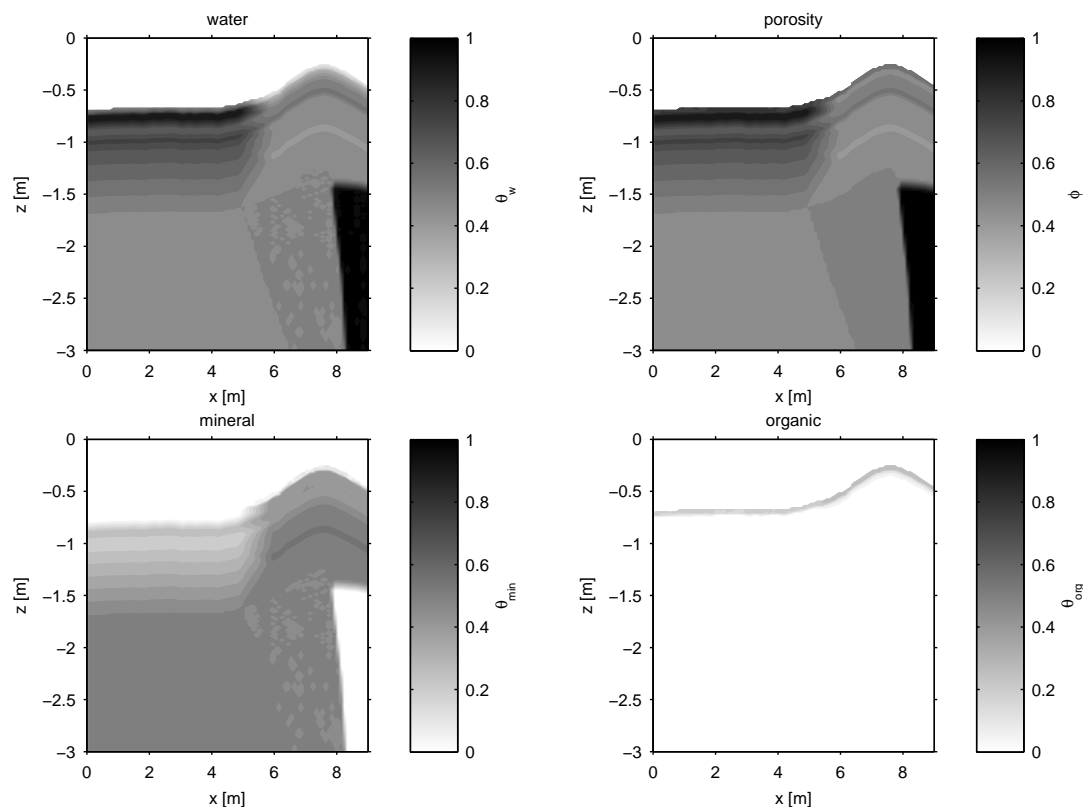


Figure 4.5: Soil composition for the two-dimensional simulation inside the polygon: Total water content (*top, left*), porosity (*top, right*), mineral material (*bottom, left*) and organic material (*bottom right*).

soil at that time. Linear interpolation between the lowest temperature sensor in the profile and the following sensor in the borehole yields to a position of the freezing front at a depth of 63 cm for that time. Figure 4.4 shows that the temperature profiles are approximately linear in the frozen and the thawed soil, respectively, but with different slopes. The actual thaw depth at the profile in the polygonal centre at the beginning of the modelling period can be estimated to 45 cm by an extrapolation of the temperature profile in the active layer to a temperature of 0 °C. The resulting difference of 18 cm can be related to a change in the latent energy storage of the active layer. For the polygon centre at that depth ($\theta_w = 0.5$) this amounts to about 27 MJ m^{-2} , which is an energy storage equivalent to a warming of the thawed active layer by almost 10 K.

In the two dimensional model configuration, the initial conditions and the soil composition are set based on information from the measurements at distinct positions in the polygon and assumptions about the structure of the polygon which is described in more detail in Chapter 2.4. The surface topography is set according to a detailed surveying that has been performed during the set-up of the soil measurements in Summer 2002. The reference line used during these measurements will be set as the origin of the z-axis pointing downwards into the soil in all two-dimensional calcula-

tions in this thesis.

The active layer composition is interpolated from the soil compositions at the temperature profiles. The transition between the centre of the polygon and the polygonal rim is set at the point where the microtopography changes from the relatively even surface of the polygon centre to the elevated rim at a distance of 5.65 m from the central point of the polygon (see Fig. 3.3).

Figure 4.5 shows the soil composition for the two-dimensional simulations. The surface properties described in Table 4.2 are used for surfaces of the rim and the centre of the polygon. The surface types are connected by a smooth transition over a relatively small length of about 50 cm. The ice-wedge under the rim of the polygon at the outer border of the model domain is assumed to consist of pure ice. The shape of the ice wedge is set with a rather simple triangular shape according to the information available from the set-up of the monitoring station (Kutzbach, 2006). The initial temperature conditions are linearly interpolated from the measurements at the three soil profiles and the borehole temperatures. A steady state solution is calculated for the deeper soil layers. This is based on the temperature of the lowest temperature sensor in the borehole and the thermal properties of the deeper soil layers.

5 Model quality assessment

The numerical model is composed of two coupled components. The main component is the soil heat transfer model that solves the non-linear diffusion equation for heat conduction including the phase change of water in the soil. The surface energy balance model is added to this model as an upper boundary condition. The two models are coupled via the surface temperature and the ground heat flux. Several steps of one-dimensional simulations are conducted to investigate the performance of the model in different configurations. The assessment of the model scheme involves the following steps:

- i) The numerical accuracy of the simulations of conductive heat transfer with phase change of water is validated based on the comparison of numerical model solutions to analytical solutions. This can be done in the case of simplified problems, for which analytical solutions exist.
- ii) The accuracy of the simulation of the thermal dynamics in a heterogeneous soil is validated based on simulations with a boundary forcing provided by temperature sensors in the soil. Thus, the model scheme is evaluated with field data without taking into account the surface energy balance calculations. The simulated heat soil temperatures are compared to measurements to judge the quality of the representation of the heat transfer processes in the soil.
- iii) The surface energy balance model cannot be validated separately. Therefore, coupled simulation of surface energy balance and soil heat transfer are investigated in different steps. Simulated soil temperatures are compared to measurements in a comparable set-up to the simulations in the previous step. This yields an assessment of the influence of the surface energy balance forcing on the soil temperatures. It also allows to identify how well the different processes and events are represented in the modelling scheme. Furthermore, the simulated heat fluxes are compared with heat fluxes measured in the ground and at the surface.

This procedure makes it possible to investigate how well different physical processes are reflected in the model at different levels of model complexity. Hence, an assessment of the quality of the simulation results with regard to the intended use in the two-dimensional simulations of heat transfer in a polygon is provided in this chapter.

5.1 Comparison of the simulations with analytical solutions

Conductive heat transfer with phase changes is a non-linear problem that cannot be analytically solved in general. This is certainly the case for freezing and thawing heterogeneous porous media that are studied in this thesis. However, there are special cases for which analytical solutions can be found. These cases can be used to validate the capability of the numerical scheme and its accuracy. Stefan problems are a special types of heat transfer problems with a moving phase boundary that often have analytical solutions. The calculations were first used by Stefan (1890) to explain the build-up and thawing of Arctic Sea Ice . The problem is characterised by the two phases ice and water showing a phase transition at the temperature of 0°C at which $\Delta H = \rho_w L_{s,l}$ is converted between sensible and latent heat. $\rho_w = 1000 \text{ kg m}^{-3}$ is the density of water and $L_{s,l} = 334 \text{ kJ kg}^{-1}$ denotes the latent heat of fusion of water. The system is treated in a one-dimensional way and described by the following initial and boundary conditions:

$$T(x = 0, t > 0) = T_0 \quad (5.1)$$

$$T(x, t = 0) = T_f = 0^\circ\text{C} \quad (5.2)$$

$$T(x = \infty, t) = T_f = 0^\circ\text{C}. \quad (5.3)$$

The thermal conductivity k and the heat capacity c have two different values for the two phases water and ice. The density is assumed to be equal in both phases. Effects of volume change are thus not considered in this approach. Carslaw and Jaeger (1959) give an analytical solution for the position of the freezing front s with time, given an initial position of the freezing front at s_0 .

$$s = s_0 + 2\lambda\sqrt{D_{\text{liq}}t}, \quad (5.4)$$

where D_{liq} denotes the thermal diffusivity of the liquid phase. The parameter λ is obtained from a solution of the equation

$$\frac{\text{Ste}_{\text{liq}}}{\text{erf}(\lambda) \exp(\lambda^2)} - \frac{\text{Ste}_{\text{sol}}}{\nu \text{erfc}(\nu\lambda) \exp(\nu^2\lambda^2)} - \lambda\sqrt{\pi}. \quad (5.5)$$

with the root of ratio of the thermal diffusivities of water and ice $\nu = \sqrt{D_{\text{liq}}/D_{\text{sol}}}$. The Stefan numbers for the two phases are

$$\text{Ste}_{\text{liq}} = \frac{c_{\text{liq}}(T_{\text{liq}} - T_f)}{\rho L} \quad \text{Ste}_{\text{sol}} = \frac{c_{\text{sol}}(T_f - T_{\text{sol}})}{\rho L}. \quad (5.6)$$

The solution of the transient equation (5.5) has to be calculated using a numerical scheme. This makes the solution only semi-analytical in practice, even though the whole derivation is completely based on analytical calculations.

In the numerical model, this situation is approached by changing the freezing curve from equation (4.2) to a steep arctangent-shaped function with zero water content for pure ice and $\theta_w = 1$ for water

$$\theta_{w,\text{liq}}(T) = \frac{\arctan(1000 T)}{\pi} + \frac{1}{2}. \quad (5.7)$$

The effective heat capacity is then calculated according to equation (2.15). The transition between water and ice in the thermal conductivity is implemented in a function of comparable shape.

The semi-infinite domain of the analytical solution cannot be represented explicitly in the discrete numerical model. Hence, a modelling domain of 1000 m with zero-flux boundary at the bottom is chosen, which approaches the semi-infinite boundary conditions of the analytical solution sufficiently well for the time scale studied here.

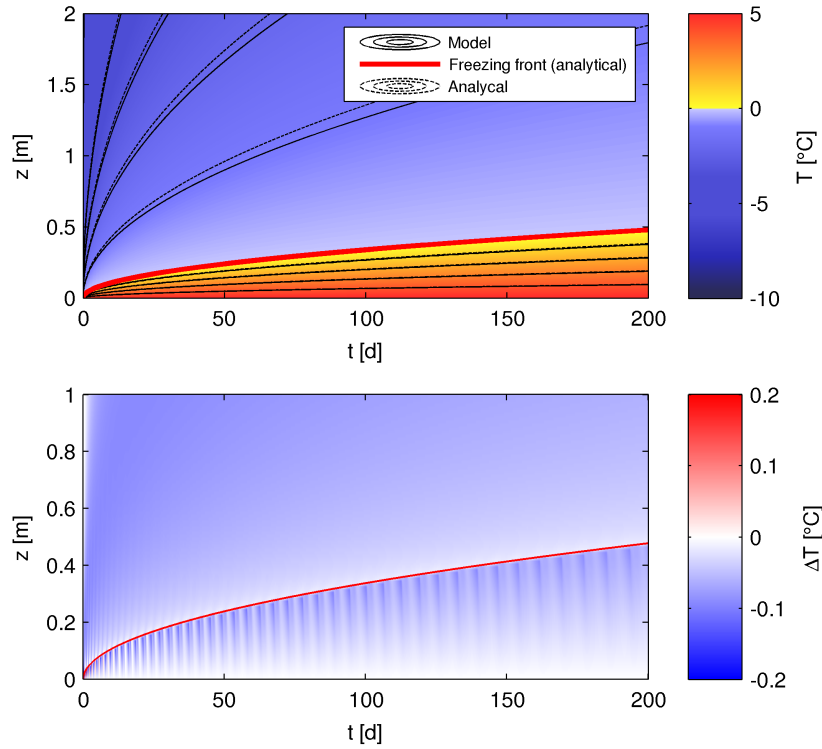


Figure 5.1: Comparison of the numerical solution of a one-dimensional Stefan problem with the respective analytical solution. The initial conditions are given by ice at -5°C in the whole model domain. The boundary conditions are a temperature of 5°C at the top and zero heat flux at the bottom. *Top:* Modelled temperature field with contour lines (black, solid), analytically calculated freezing front (red) and contour lines of the analytical temperature field (black, dashed).

Bottom: Difference between the modelled temperature field and the analytical solution. The colour saturation is proportional to the intensity of the deviation, the colour (red/blue) gives the sign of the difference

Figure 5.1 shows the results of the numerical simulation of the progression of a thawing front into the ice. The initial temperature is $-5\text{ }^{\circ}\text{C}$ throughout the entire model domain. The temperature at the top is set to $5\text{ }^{\circ}\text{C}$ and kept constant over time. The advance of the thawing front is simulated accurately by the numerical model. The deviations in the temperature fields are smaller than $0.1\text{ }^{\circ}\text{C}$ and can be attributed to the implementation of the freezing front in the numerical calculations. This limits the heat transfer due to the smaller temperature gradients within the material that is at a temperature around the freezing point. The error plot shows deviations on the order of $0.2\text{ }^{\circ}\text{C}$ in a very regular pattern in the thawed soil. This is an artefact of the spatial discretisation in the model with a grid size of 1 cm . Instead of a continuously moving thawing front the freezing front in the numerical model can only move stepwise from one grid cell to the next one, which also slightly inhibits the heat transfer towards the freezing front.

A second example of a phase change problem with an analytical solution provided by Carslaw and Jaeger (1959) can be used for the numerical assessment of the two-dimensional model configuration in cylindrical coordinates.

A cylinder of infinite size in radial direction is treated under the same assumptions as in the previous example. At $t = 0$ the water in the cylinder is at a temperature $T_{\text{liq}} > T_f$.

For $t > 0$, heat is extracted at the central axis of rotation with a constant rate Q that is given as a heat flux per length in W m^{-1} . A freezing front penetrates into

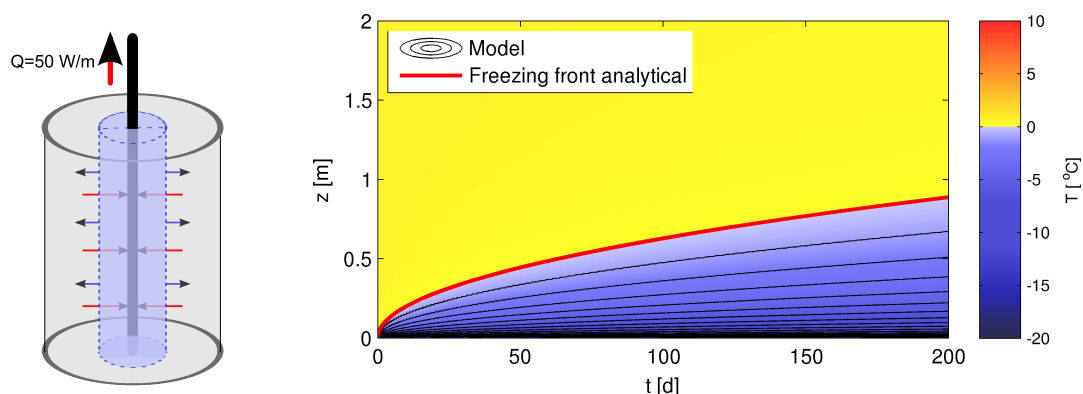


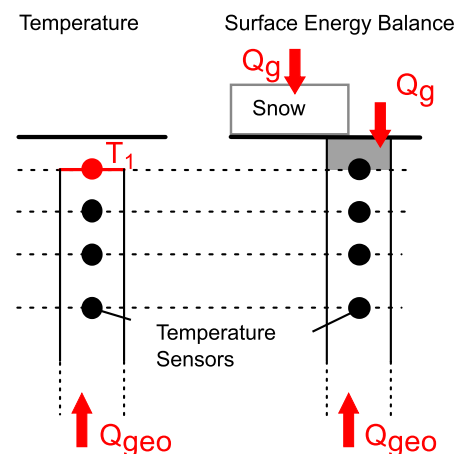
Figure 5.2: Comparison of the of simulations for the two-dimensional cylindrical Stefan problem with the respective analytical solution. *Left:* Schematic illustration of the simulated problem in the semi infinite cylinder. The red arrows indicate the direction of the heat fluxes, while the blue arrows show the movement of the freezing front. *Right:* Simulation result and analytically calculated freezing front. The simulated temperature field is displayed by the colour and with black contour lines. The analytically calculated freezing front is depicted by the red line. The initial conditions are given by liquid water at $0.5\text{ }^{\circ}\text{C}$. The boundary conditions are a heat flux density of $j_{\text{centre}} = 50\text{ W m}^{-1}$ along the central axis of the cylinder and zero heat flux at the top, at the bottom and at the outside of the cylinder

the liquid water. The heat transfer is assumed to be purely conductive in both phases. Carslaw and Jaeger (1959) provide a formula to calculate the advance of the freezing front that is similar to equation (5.5). The equations for the analytical temperature field given there, however, do not yield reasonable results and are thus discarded here. Hence, the comparison of the simulation and the analytical solution is restricted to the development of the freezing shown in Figure 5.2. As in the case of the one-dimensional simulation, the freezing front from the analytical solution is represented well in the numerical model.

5.2 Soil model with forcing from soil temperature measurements

To evaluate the model for conductive heat transfer the simulation results are compared to measured soil temperatures at the study site. The one-dimensional soil model can be run based on upper boundary forcing from the soil temperature sensors closest to the surface at a depth of 3 cm. This leads to a model configuration that does not include the energy exchange processes at the soil surface. Nevertheless, the daily cycle of the temperature dynamics is still present in the uppermost layers of the model as it is not completely damped out at that shallow depth. The lower boundary is given by the geothermal heat flux at a large depth. One-dimensional simulations are performed for both temperature profiles in the centre of the polygon and at the rim of the polygon. The initial temperature distribution and the soil composition are set based on measurement data (see Chapter 4). Figure 5.4 shows the simulated temperature over the two year model period for both profiles. The maximum thaw depth reaches a value of 46 cm on 24 August 2011 in the centre and 58 cm on 1 September 2011 in the rim of the polygon. A comparison of the simulated soil temperatures with the measured values for several sensors in the profiles at the rim and at the centre of the polygon is given in Figure 5.5 and Figure 5.6. The measured and simulated temperatures at the other sensor depths for both profiles

Figure 5.3: Schematic overview of the two types of one-dimensional simulation in this study. *Left:* Temperature measurements from the uppermost sensor as the upper boundary condition to the soil heat transfer model. *Right:* Forcing from the surface energy balance model (see Figure 4.1). The calculated ground heat flux is applied as a flux boundary either at the ground surface or at the surface of the snow layer. Temperature sensors are in the same depth for both simulation types, so the results are directly comparable between these simulations. The geothermal heat flux Q_{geo} gives the lower boundary in both cases.



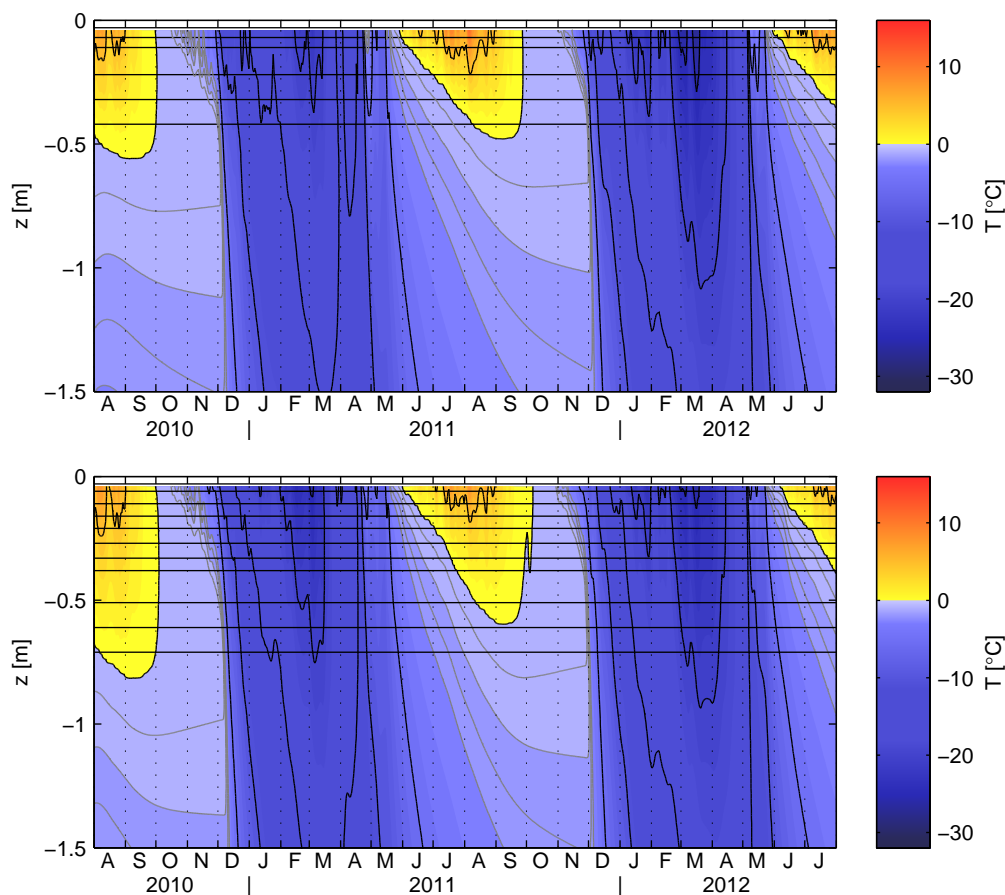


Figure 5.4: Simulated soil temperature for the simulations driven with soil temperature sensors 3 cm below the surface- for the centre of the polygon (*top*) and the rim of the polygon (*bottom*). Black contour lines are given in 5 °C distance. The grey contour lines in 0.5 °C distance depict the isotherms between -2°C and 0°C . The horizontal black lines show the positions of the soil temperature sensors in the profiles.

and the corresponding deviations are presented in the Appendix A.4 in Figure A.8 and Figure A.9.

In the polygon centre, the simulated soil temperature is in good accordance with the measured data. The mean absolute error (MAE) is smaller than 0.5°C and maximal deviations are on the order of $2\text{--}3^{\circ}\text{C}$. The largest differences occur in very distinct peaks during the onset of freezing and thawing. In both depths the summer temperatures are slightly underestimated. The lowest sensor is thawed in both summers both in the measurement data and in the model. However, a slight underestimation of the thaw depth by a few cm can be inferred from the temperature differences in summer.

Comparing the simulated soil temperatures with the measurements in the profile at the rim of the polygon (see Figure 5.6) shows stronger deviations than in the polygon centre. As the profile stretches down to a larger depth due to the larger

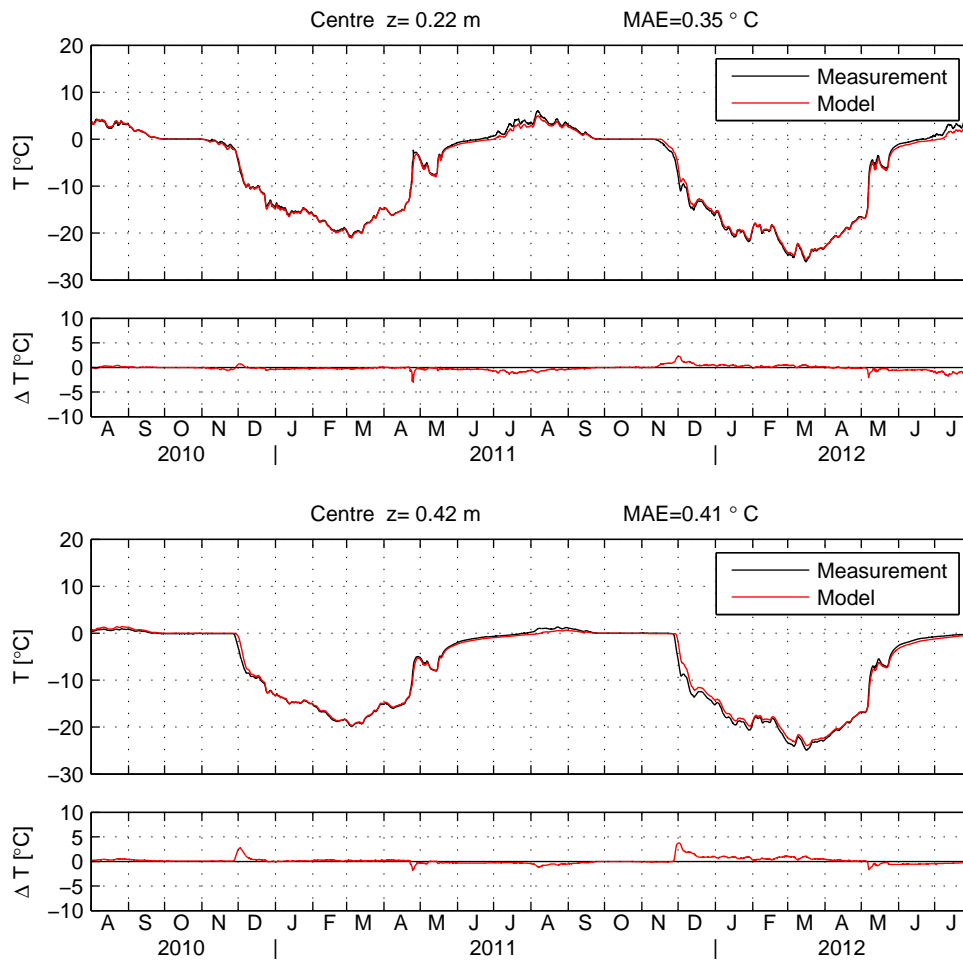


Figure 5.5: Simulated soil temperatures (*red*) based on forcing with soil temperature sensors 3 cm below the surface and measured temperature at two depths in the polygon centre. *Top:* 22 cm. *Bottom:* 42 cm, close to the permafrost table. The difference ΔT between modelled and measured temperatures is shown below the temperature curves for each sensor.

active layer thickness of about 70 cm, three different sensor depths are examined here. The mean absolute error between the model and the measurements is up to 1°C over the two year period. Maximum deviations reach up to 5°C during the onset of the freezing in November and December 2010. The temperature is slightly overestimated in both winters at all sensors. The summer temperatures are underestimated by a comparable amount for both upper sensors. In contrast to the model, the measurement of the sensor at 71 cm shows thawed soil in both summers. This indicates that the maximum thaw depth is underestimated in the polygonal rim.

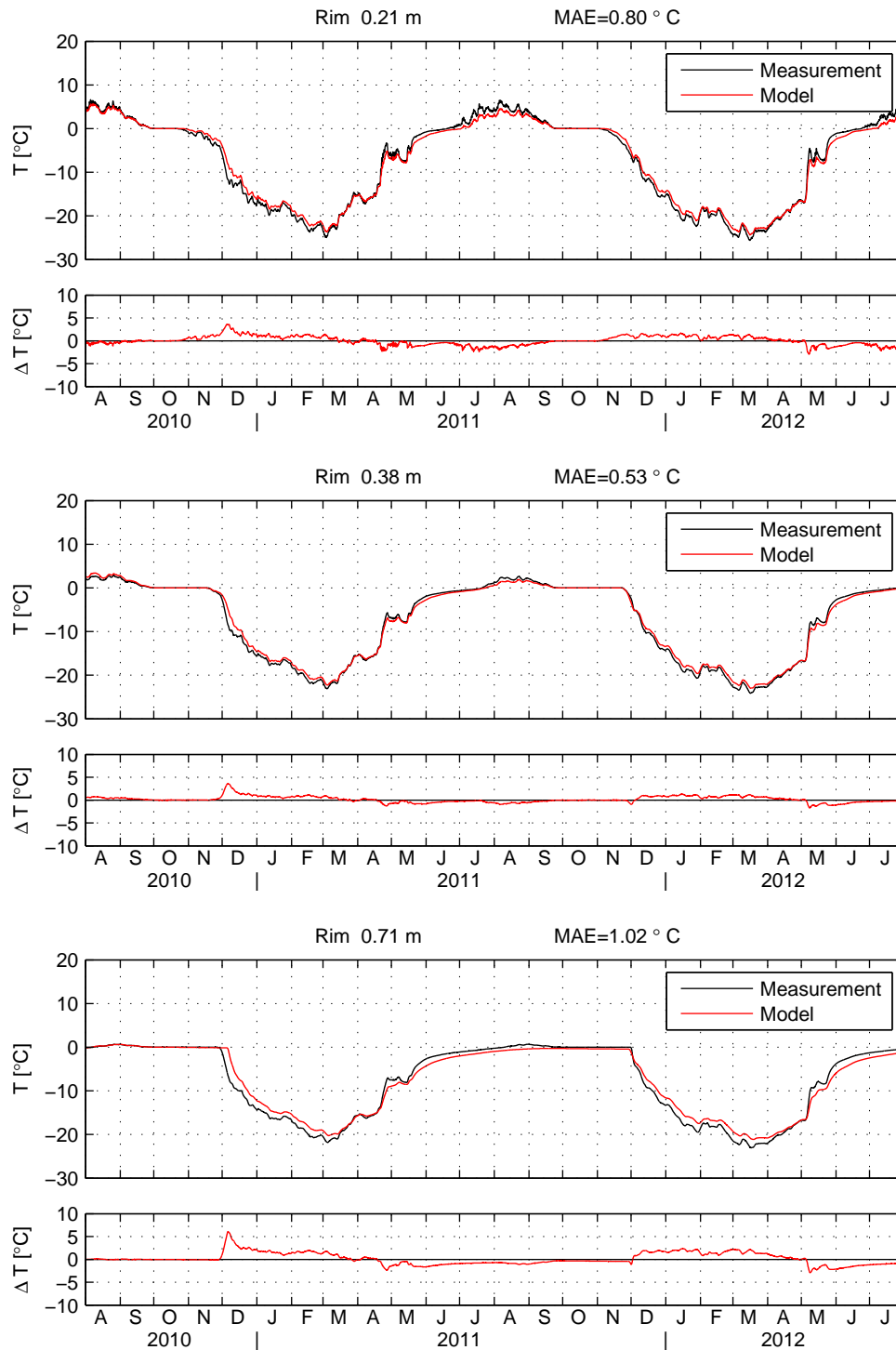


Figure 5.6: Simulated soil temperatures (*red*) based on forcing with soil temperature sensors 3 cm below the surface and soil temperature measurements (*black*) at three depths in the polygon rim. *Top:* 21 cm. *Centre:* 38 cm. *Bottom:* 71 cm, close to the permafrost table. The difference ΔT between modelled and measured temperatures is shown below the temperature curves for each sensor.

5.3 Simulations with the coupled surface energy balance

The coupled model consists of the soil heat transfer model and the model scheme for the calculation of the surface energy balance and the snow layer. Figure 5.3 shows a schematic overview of the two model configurations used for the soil heat transfer simulations in Section 5.2 and the coupled simulations in this Section. The two model set-ups are identical in the entire modelling domain below the uppermost soil temperature sensor. This includes soil composition, initial conditions and the lower boundary condition. The grid is set up such that the depths are equal for the simulated soil temperatures to be directly comparable.

The model configuration studied in this section adds several components to the simulation of heat transfer in the soil. An additional soil layer above the uppermost temperature sensors is added to the model description. This is a predominantly organic layer of living and dead mosses with high porosity. As there are no TDR probes installed above 7 cm in the soil profiles, there is no measurement value of water content that can be used for the determinations of the model parameters. Furthermore determination of the exact distance between the sensors and the soil surface is not certain for all sensors. These difficulties can be attributed to surface topography, vegetation cover and possible vertical movement of the soil that the sensor is placed in. In Figure A.12 and Figure A.13 in the Appendix A.6 the results of model runs with a variation of surface cover thickness and total water content in the uppermost soil layer are displayed both at the centre of the polygon and at the polygonal rim. The influences on the soil temperature in a depth of about 20 cm are used as a reference here, since soil heat transfer in the model is reliable at that depth (see Section 5.2). The distances of the sensors to the surface can be assumed to be correct, since changes in the thickness of the organic layer above the uppermost temperature sensors do not lead to improvements in the accordance between model and measurements. The variation of the water content in the near-surface moss layer reveals that the temperature measurements in the active layer are best represented with a water content in the surface layer of 30% at the centre of the polygon and 25% at the the rim of the polygon.

Figure 5.7 shows the simulated soil temperatures over the course of the modelling period in the upper 1.5 m for the centre and the rim of the polygon. The maximum thaw depth in the second summer is reached at 44 cm on 4 September 2011 in the centre of the polygon. In the polygonal rim, the maximum thaw depth of 49 cm is reached on 3 September 2011. Both simulations represent the typical annual cycle of the permafrost according to the description in Chapter 2.4. In comparison to the simulations based on temperature measurements in the soil in Section 5.2, the temperatures of the permafrost below the active layer are considerably smaller during summer in both profiles.

A comparison of the simulated temperature curves with measurements in the polygon centre is displayed in Figure 5.8. The sensor depths are the same as in the

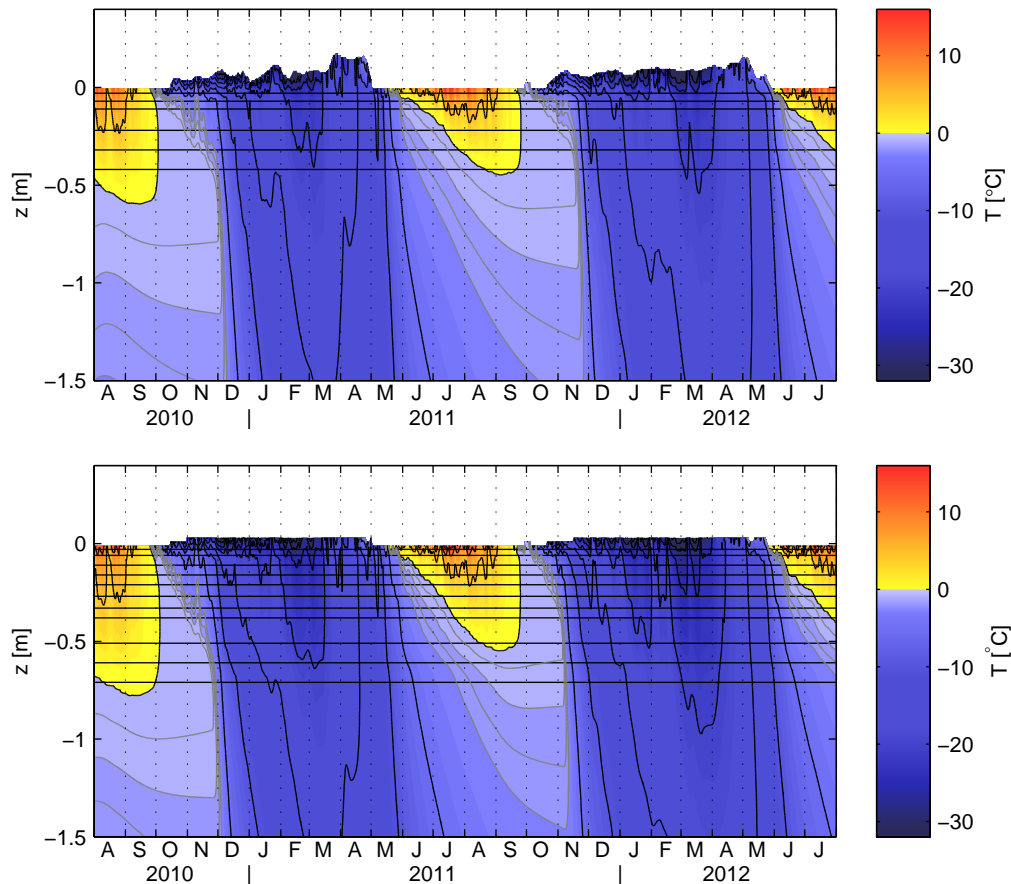


Figure 5.7: Coupled simulations of the surface energy balance and the soil heat transfer at the centre of the polygon (*top*) and at the rim of the polygon (*bottom*). Black contour lines are given in 5°C distance. The grey contour lines in 0.5°C distance depict the isotherms between -2°C and 0°C . The horizontal lines show the positions of the soil temperature sensors. The snow height is different due to the threshold snow depth set for the simulation at the rim of the polygon to account for wind drift effects (see Chapter 4).

simulation with forcing from the uppermost soil temperature sensor displayed in Figure 5.5. The model is able to reproduce the measurement with a mean absolute error (MAE) of about 1.5°C for the two sensors in 22 cm and 42 cm depth.

Deviations of up to 10°C occur during the strong warming periods in the spring of 2011 and 2012. While the measured temperature rises by about 10°C in the course of a few days, this temperature change is not represented in the model. The freezing period is represented comparatively well in the first winter, with deviations of up to 2°C at both sensors. That also leads to a good representation of the cold winter temperatures. However, the freezing period during the second winter does not agree to a comparable degree. In both depths, the length of the zero curtain is under-represented by about two weeks. This leads to a shift in the rapid cooling in the following period, which leads to differences of up to 5°C between modelled and

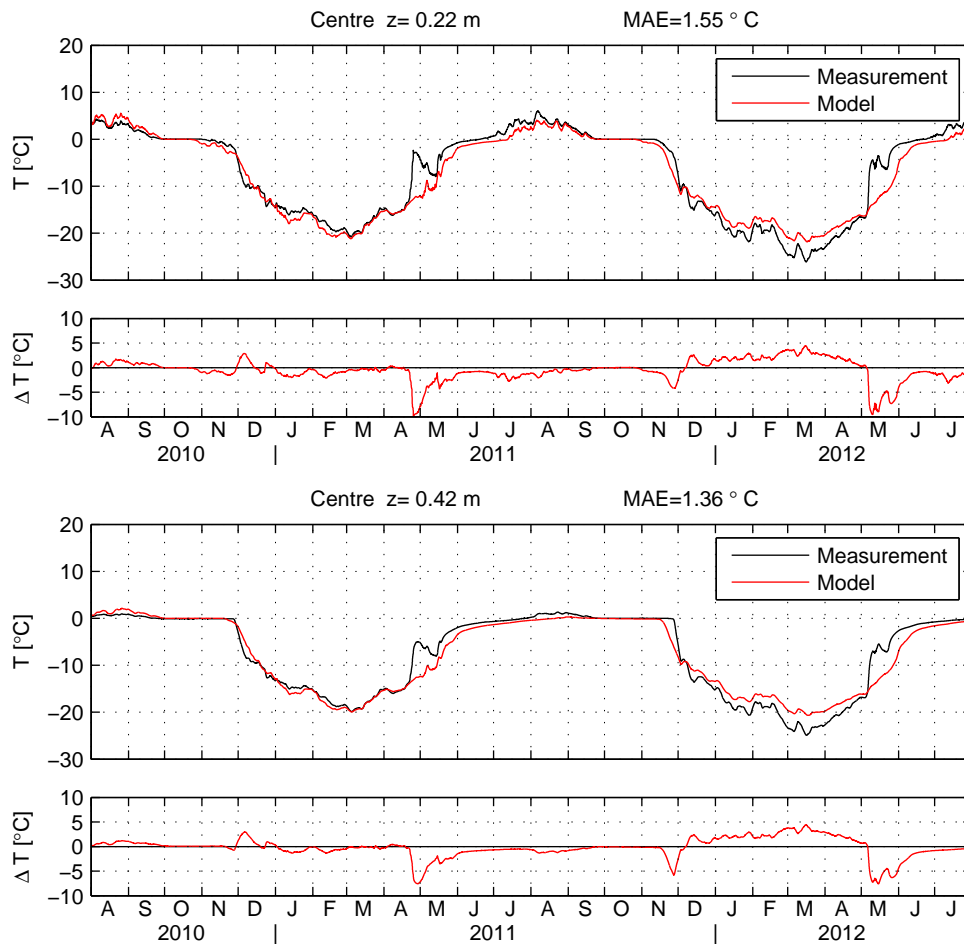


Figure 5.8: Simulation with forcing from the surface energy balance model and measurement at two depths in the polygon centre *Top*: 22 cm, *bottom*: 42 cm, close to the permafrost table. The difference ΔT between modelled and measured temperatures is shown below the temperature curves for each sensor.

measured temperatures. The winter temperatures, however, are overestimated from December 2011 to April 2013 after the end of the rapid cooling period in November/December 2011. The simulated soil temperature remains constantly above the measured temperature by about 2–3 °C.

In the profile in the rim of the polygon (Fig. 5.9) the accordance between the model and the measurements is comparable to that in the centre. The average absolute deviations are 1.38 °C and 1.31 °C for the two upper sensors. The temperature curve at the lowest sensor is reproduced considerably worse. The MAE is about 2 °C. This sensor shows temperatures above 0 °C during the summer of 2011 that are not reproduced in the simulation, which means that the thaw depth is underestimated by the model simulation.

The events that show the maximum deviations between the model and the measurements are the same as in the centre of the polygon. The measurement data

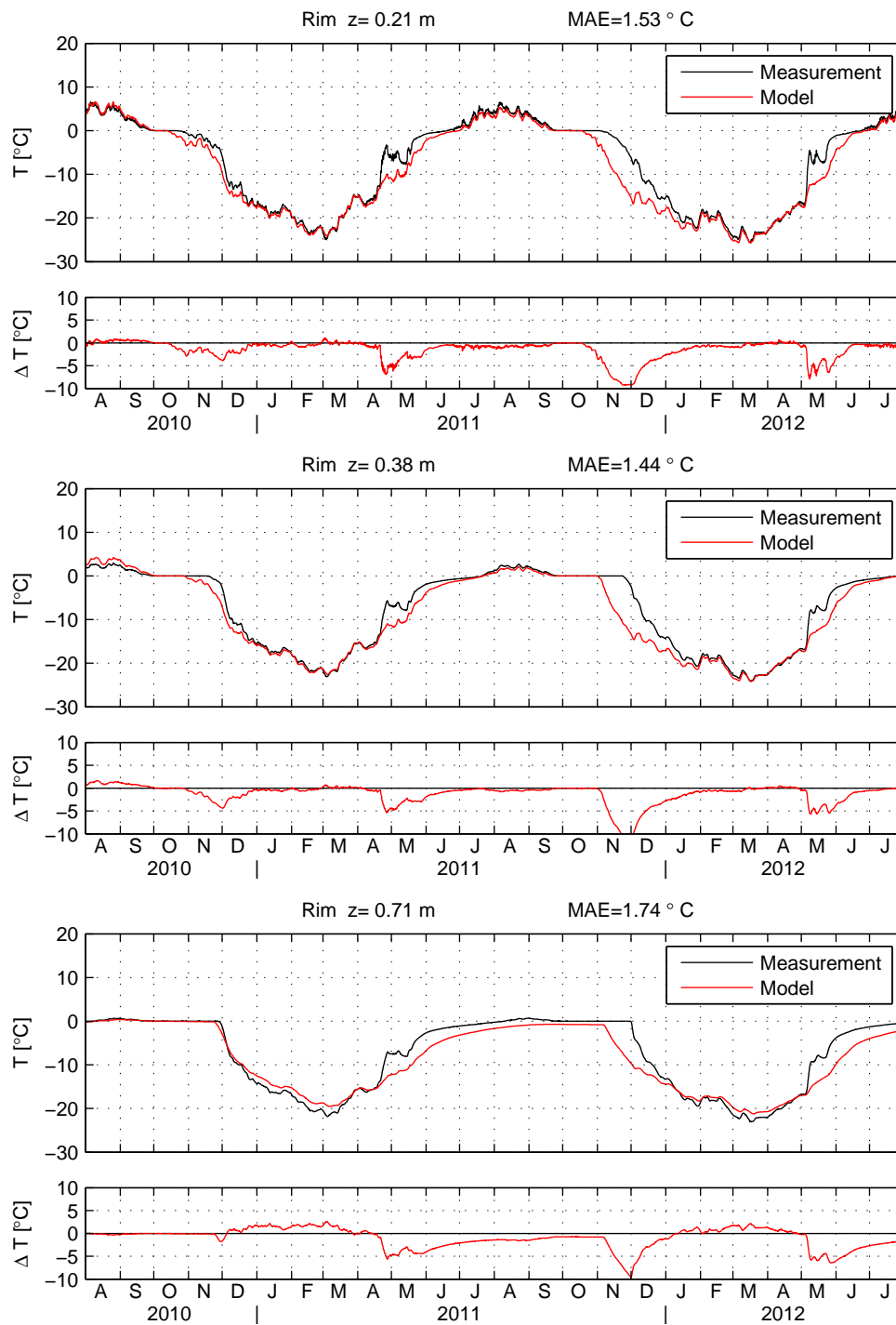


Figure 5.9: Simulation with forcing from the surface energy balance model and measurement at three depths in the polygon rim. *Top:* 21 cm, *centre:* 38 cm, *bottom:* 71 cm, close to the permafrost table. The difference ΔT between modelled and measured temperatures is shown below the temperature curves for each sensor.

shows distinct warming events at the end of April 2011 and at the beginning of May in 2012. The soil temperature rises by about $10\text{ }^{\circ}\text{C}$ within only a few days before remaining relatively constant at around $-8\text{ }^{\circ}\text{C}$ to $-6\text{ }^{\circ}\text{C}$ over the course of about two weeks. This feature is not represented in the modelled soil temperature. In the freezing period at the beginning of the winter in 2011, the length of the zero curtain is underestimated by about two weeks in the simulations. The deviation between the soil temperatures and the measurements does not exceed $2\text{ }^{\circ}\text{C}$. During the second winter of the modelling period, the deviations between model and measurement is of the same magnitude in the centre of the polygon. In the profile at the rim of the polygon however, the deviations are markedly worse. Although the difference between modelled and measured length of the isothermal period is comparable to the presuming winter, the temperature differences reach up to $10\text{ }^{\circ}\text{C}$ for a period of about a month. The winter temperatures afterwards, however, are in rather good agreement with the measurements.

Modelled and measured soil heat flux:

The heat flux plates installed at 7 cm depth both in the centre and at the rim of the polygon offer a direct measurement value of the heat flux in the soil layer below the soil surface. The measured heat fluxes both in the rim and in the centre

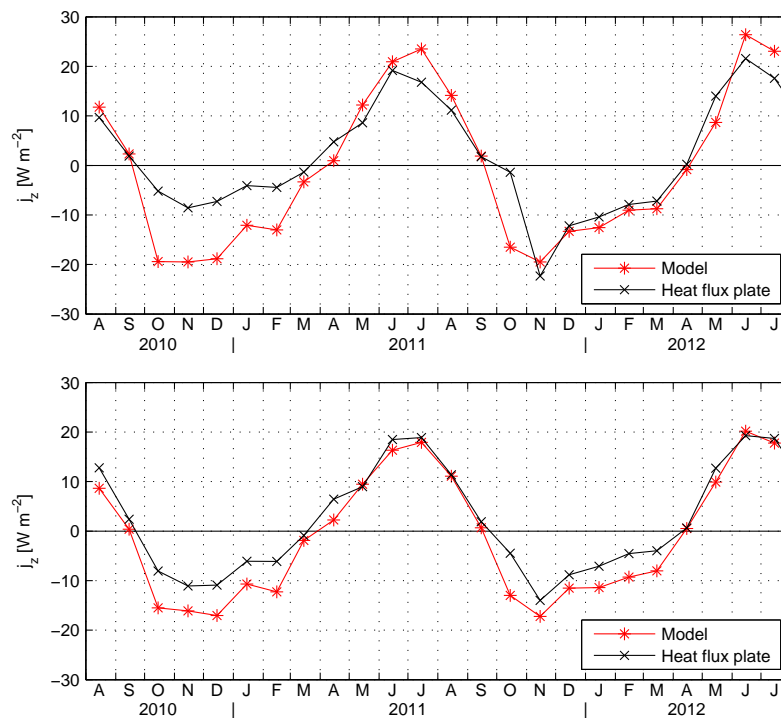


Figure 5.10: Heat flux in the soil at a depth of 7 cm for the centre of the polygon (top) and for the rim of the polygon (bottom). The model results in red and measurements of the heat flux plates in black.

are visualised together with the simulated conductive heat fluxes interpolated to that depth in Figure 5.10. At both measurement points a comparable distribution of negative and positive heat fluxes occurs over the course of the two year model period, both for the measurements and the simulation results. In the winter months from October to March there is a negative conductive heat flux, i.e. a flux of sensible heat towards the surface. The other six months of the year, April to September, are characterised by positive heat fluxes with only very small average values in April and September.

In the centre of the polygon, a strong deviation between the measured soil heat flux and the simulated heat flux is found during the winter months of the first year. The measured heat flux never exceeds an average of -8 W m^{-2} during the six month period of negative heat balance of the soil. The simulated heat fluxes reach almost three times that value, with maximal heat fluxes of -20 W m^{-2} from October to December 2010 and about -10 W m^{-2} during January and February 2011. In the following year, however, measured and modelled heat fluxes agree better, with an average heat flux of around 12 W m^{-2} over the course of the winter. October 2011 forms an exception. The modelled heat flux reaches large values of almost 20 W m^{-2} while the average measured heat flux is almost zero. In late summer the modelled heat fluxes in the centre exceed the measured values by up to $5 \text{ }^\circ\text{C}$.

In the rim of the polygon, the measured and modelled heat fluxes show a comparable temporal course during the two years of the model period. During the summer months, the measurements and the simulations are in good agreement. During the winter months, the simulated fluxes at the rim are smaller than the fluxes in the centre of the polygon with heat fluxes of -15 W m^{-2} during the freezing period. The measured heat fluxes are considerably smaller and only reach -10 W m^{-2} during the early winter period.

Surface energy balance components:

The heat flux components calculated in the simulations can be compared with direct measurements of the atmospheric flux components, i.e. radiation and turbulent heat fluxes. This comparison is done based on the simulation at the centre of the polygon as the radiation sensor is placed above wet tundra surface.

The outgoing radiation in the two different wavelength bands and the net radiation balance of the surface are available from the four component radiation sensor that also delivers the radiation components of the forcing dataset. Figure 5.11 shows the modelled outgoing radiation components and the respective values measured by the four component radiation sensor. For the short-wave radiation most data points are scattered around the line of equal values, implying that the albedo is chosen right for the respective surface. Two additional line-shaped clusters of data can be identified at two symmetrical positions of the central line of agreement. These depict periods during which the surface albedo in the model does not reflect the real conditions. The albedo is either over- or underestimated by about a factor of six which corresponds to the albedo difference between the snow cover and the vegetation surface in the

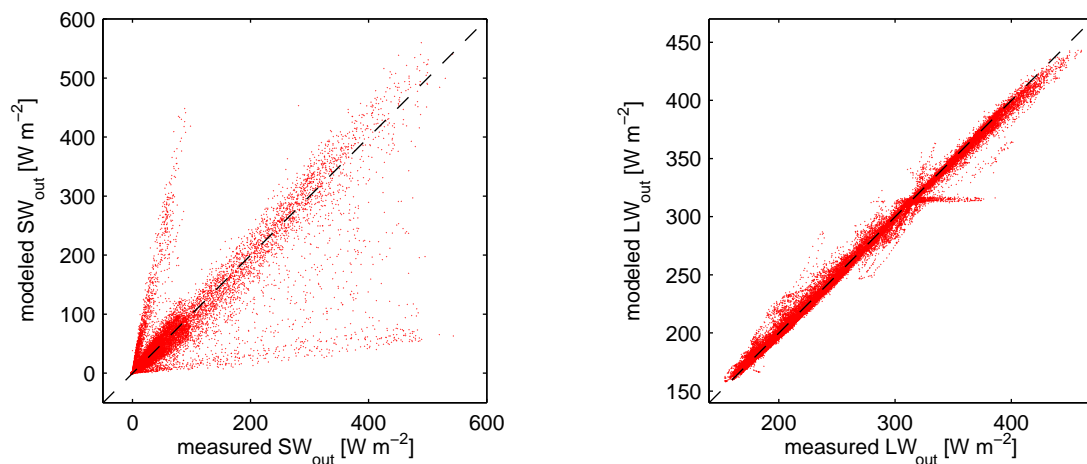


Figure 5.11: Modelled and measured outgoing radiation in the short-wave range (left) and in the long-wave range (right).

centre of the polygon. Additional data points reveal periods during which the model underestimates the short-wave radiation less strongly. These can be attributed to periods during which the model simulated a snow cover while the measurements indicate a partial snow cover.

Outgoing long-wave radiation is closely coupled to the surface temperatures by a correction for the small fraction of reflected incoming thermal radiation and the different scaling due to the fourth power in Stefan-Boltzmann's law according to equation (2.4). There is a good agreement between the model in the range of up to about 300 W m^{-2} , which corresponds to negative surface temperatures. For stronger outgoing radiation in the summer periods there is an underestimation of the outgoing long-wave radiation, i.e. an underestimation of the surface temperature. Several distinct stronger deviations between measured and simulated long-wave radiation can be identified. At a simulated outgoing radiation of 315 W m^{-2} , corresponding to a surface temperature of 0°C , the measured values spread widely while the simulated values remain constant. This corresponds to the freezing and thawing periods of the uppermost soil cell in the model.

The simulated components of the surface energy balance for the two-year model period are shown in Figure 5.12. The net radiation is characterised by positive fluxes until September in both years and then decreases to negative values of around -15 W m^{-2} to -20 W m^{-2} during the winter months (October to March). This includes the periods of polar night and the adjacent weeks of low incoming solar radiation. In April of both years the radiation components balance each other almost completely. During May a small positive flux of 30 W m^{-2} occurs in both years, despite the already strong incoming solar radiation. The net radiation reaches its maximum during June and then slightly decreases over the course of the summer along with the decrease in the incoming solar radiation.

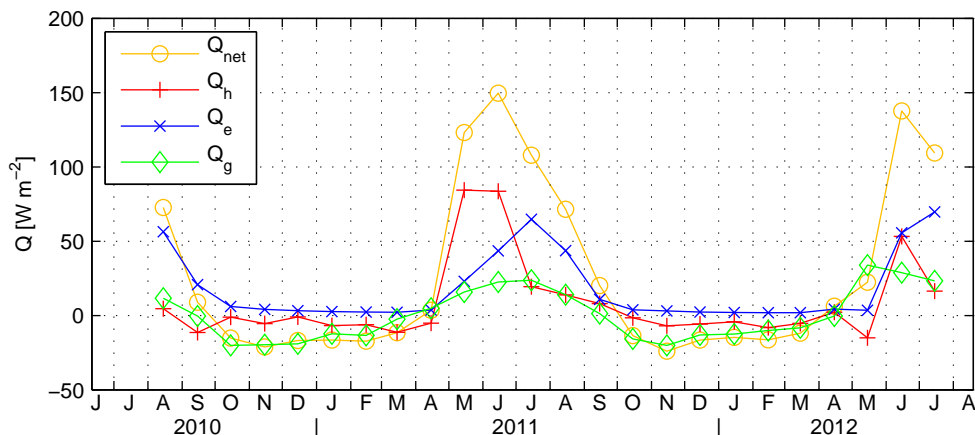


Figure 5.12: Components of the simulated surface energy balance over the course of the two year model period, including net radiation Q_{net} (yellow), sensible heat flux Q_{h} (red), latent heat flux Q_{e} (blue) and ground heat flux Q_{g} (green).

The sensible heat flux Q_{h} is negative during all months of the snow covered period that spans from October until April or May with average fluxes of -5 W m^{-2} to -10 W m^{-2} . During May and June 2011 a maximal positive sensible heat flux of 84 W m^{-2} occurs. The later summer months are characterised by lower sensible heat fluxes of less than 20 W m^{-2} . The turbulent flux of latent heat Q_{e} shows a constant positive flux of less than 5 W m^{-2} during the snow covered period from October to April in both years. Hence, there is a small but constant flux of water vapour from the surface to the atmosphere and thus a sublimation from the snow surface. The flux is only slightly stronger in May in both years (10 W m^{-2}). During the three summer months (June, July, August) the averaged flux of latent heat reaches its maximum of about 70 W m^{-2} before it decreases again in September. The turbulent heat fluxes balance each other partly during the winter months, resulting in a slightly negative heat flux, i.e. directed from the atmosphere to the ground for the period from October to May.

The ground heat flux Q_{g} , which is calculated as the residuum of the other energy balance components, features a rather smooth curve compared to the other heat fluxes. During the winter months the ground heat flux mostly follows the course of the net radiation with maximum negative heat fluxes of -20 W m^{-2} and a slight decrease over the winter months. In April almost no average ground heat flux is present in both years. In the summer months, the heat flux into the ground reaches a maximum of 25 W m^{-2} in June/July and decreases to a value around zero in September in both years. The ground heat flux shows a distinct difference between the two years in May, with 20 W m^{-2} in 2011 and 35 W m^{-2} in 2012.

The modelled surface energy balance components displayed in Figure 5.12 can be compared with previous studies (Kutzbach, 2006; Langer et al., 2011a,b) at the same study site. The respective measurements of the turbulent heat fluxes have not been taken continuously during the model period. Furthermore, the data processing of

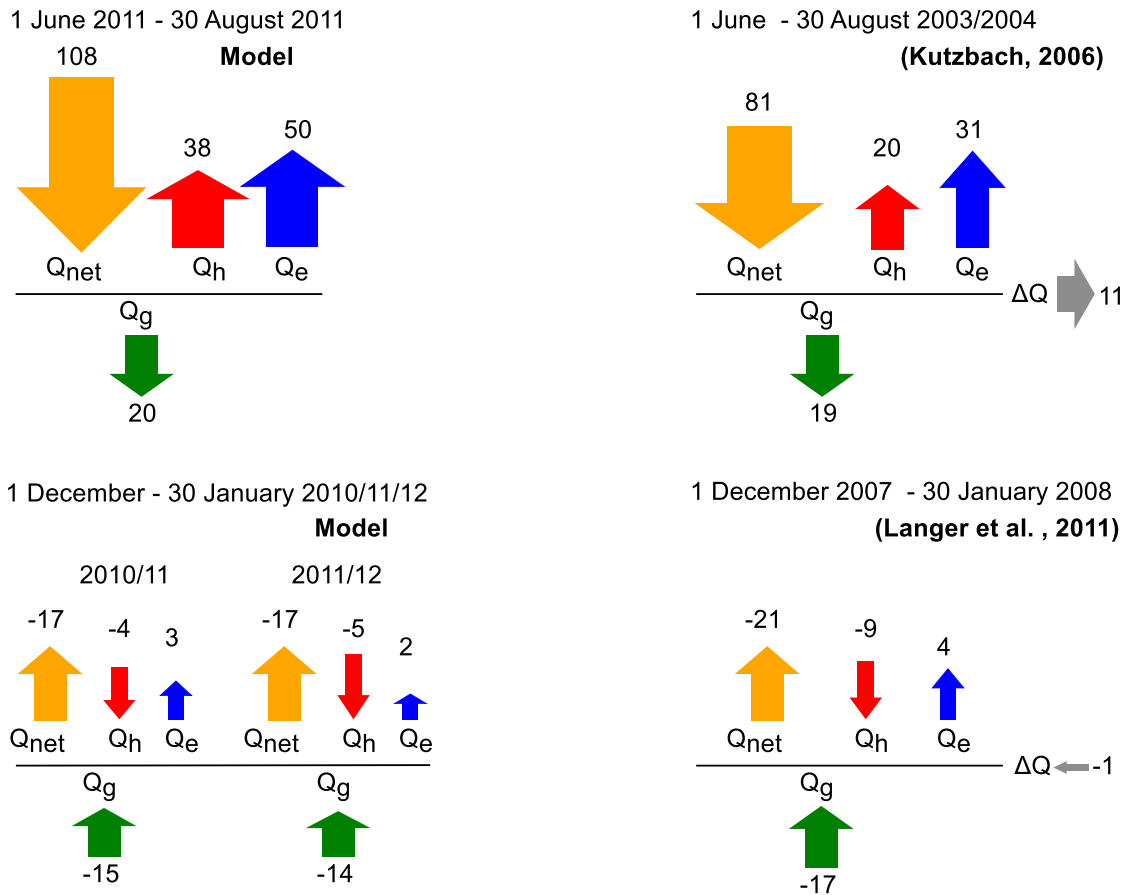


Figure 5.13: Mean surface energy balance components for a summer and a winter period compared to measurement studies in previous years. *Top:* Surface energy balance simulation for the summer period June-August 2011 compared to same months in 2003/2004 from Kutzbach (2006). *Right:* Surface energy balance simulation for the polar winter period December-January 2010/2011 and 2011/12 compared to same months in 2007/2008 from Langer et al. (2011b). Net radiation Q_{net} in yellow, sensible heat flux Q_h in red, latent heat flux Q_e in blue, ground heat flux Q_g in green, and energy balance closure C in grey.

the existing raw data during parts of the model period was not in the scope of this thesis.

Therefore, the assessment of the surface energy balance components has to be based on measurements in previous years. In these studies all four components of the net radiation were directly measured with net radiometers, the eddy covariance method and the evaluation of the data from soil temperature sensors. The modelled heat fluxes are compared to measured heat fluxes during a summer period and a winter period during polar night. These periods are expected to yield the most informative results in a comparison between different years. In contrast, strong differences between the years can be expected for spring and autumn periods due to the timing of the snow cover and more variable weather conditions.

Figure 5.13 displays heat flux measurements from Kutzbach (2006) for a summer period (1 June to 31 August) in the years 2003 and 2004. Furthermore measured heat fluxes from Langer et al. (2011b) for the polar winter from 1 December 2007 to 30 January 2008 are presented. These measurements are compared with the simulated surface energy balance for the respective times during the model period.

In the three summer months, the atmospheric heat fluxes in the model are exceeding the heat fluxes in the measurement period substantially. The ratio of the other heat flux components to the net radiation, which is the main driver of the temperature changes at the surface, is more comparable ($Q_h/Q_{\text{net}} = 0.18$, $Q_e/Q_{\text{net}} = 0.18$ in the simulations; $Q_h/Q_{\text{net}} = 0.25$, $Q_e/Q_{\text{net}} = 0.41$ from the measurements in 2003/2004). The Bowen ratio Q_h/Q_{net} shows a dominant contribution of latent heat flux over sensible heat flux both for the simulations (0.75) and the measurement dataset (0.63) during the summer months. The ground heat flux is almost equal in the two datasets. The energy balance closure term ΔQ of the measured surface energy balance is 11 W m^{-2} .

The comparison of the winter periods shows a consistent picture for the two simulated winter periods with almost equal values for the surface energy balance components. The measured surface energy balance in the winter 2007/2008 is characterised by slightly higher fluxes for all components of the surface energy balance. This especially applies to the turbulent heat fluxes that are about twice as high as the values obtained for the two winters of the modelling period. The energy balance closure of the measurements during the winter period is low (-1 W m^{-2}).

5.4 Discussion

Numerical model scheme

The comparison of the simulated model results with the analytical solution of the Stefan problem shows that the model is capable of a numerically correct simulation of the heat transfer equation with phase change in a homogeneous medium. This applies both for the one-dimensional model set-up and for a cylindrical case with radial symmetry. The observed minor deviations can be directly attributed to two different aspects of the numerical discretisation in the model. They do not have direct implications for the application of the model in the soil. The deviations introduced by the artificial freezing curve in the system of pure water and ice are not relevant for the simulations in the soil, because a pronounced freezing characteristic is intentionally used here. The effects of the spatial discretisation of the model on the freezing front that are clearly visible in Figure 5.1 are not relevant for the application of the numerical scheme, since they do not have an impact on the development of the freezing front.

Heat transfer in the soil

The simulated soil temperatures in the model runs forced with the temperature of the uppermost soil temperature sensors (Fig. 5.5 and Fig. 5.6) is in good accordance with the soil temperature measurements at different depths. The simulation for the centre of the polygon shows a better agreement, which can be attributed to the rather homogeneous soil composition and water saturation up to the top of the model domain. This leads to a soil composition that is described very well in terms of the heat capacity and the heat conductivity based on the measurement data. The rim features a stronger heterogeneity in the soil composition and an unsaturated part at the top of the model domain. Furthermore, larger fractions of mineral material are present, for which the thermal conductivity has been set to a standard value in Table 4.1, which might also add deviations to the calculated heat conductivities.

In both profiles, the measured thaw depth is not reached in the summer months of 2011 and the simulated temperatures are lower than the measured temperatures in larger depths. That could be attributed to two different factors. The temperature in the lower part of the active layer is not only determined by the heat transfer processes inside the active layer during the thawing in summer. The temperature in the perennally frozen permafrost below the freezing front also determines the speed of the front to a certain extend. Hence, a stronger cooling of the lower soil layers during the preceding winter can also be a cause of the underestimation of the maximum thaw depth. The soil composition in the permafrost is set based on less detailed measurements than inside the active layer, which can explain some deviation at the lower boundary of the active layer.

Besides these smaller deviations, the heat transfer in the soil is described very well by the model with mean absolute deviations of less than 1 °C for most of the sensors. This confirms that the heat transfer in the soil layers below the depth of the first temperature sensor (3 cm) can be accurately described by heat conduction and the effects of the phase change of water. Thus, non-conductive heat transfer processes such as convective transport or water vapour diffusion, can be neglected at these depths. This might be completely different for the uppermost soil layer. This layer could not be investigated in the same detail in terms of heat transfer in this study, since processes close to the surface can only be regarded in combination with the effects of the snow cover and of the surface energy balance based on the data available in this thesis.

Organic moss layer at the surface

The results of the variation of the surface position (see Fig. A.12 and Fig. A.13) on the soil temperatures indicate that the distance to the surface set during the installation of the sensors in the polygon is consistent. The variations of the surface position do not lead to an increased agreement between the simulation and the measurement.

The water content of the uppermost soil layer has a strong influence on the soil temperature in the active layer. Although the changes in water content only apply

to a thin layer of about 5 cm thickness, the variations are on the order of several degrees centigrade at a depth of 20 cm. In winter, the insulation effect is combined with that of the snow cover which has a comparably low heat conductivity. However, these two effects cannot be easily separated in this simple consideration. In summer, the temperatures are also influenced by the surface parameters such as roughness length and resistance to evaporation. Hence, the chosen water contents of 30 % in the centre and 25 % in the rim of the polygon must be seen as an estimate with large influence from these surface parameters.

The importance of the correct representation of the near-surface organic layer of Arctic soils has also been shown on a regional to global scale (Rinke et al., 2008; Beringer et al., 2001). On the one hand, that includes the direct influence on the soil temperatures and soil moisture due to different fluxes of heat and water at the surface. On the other hand, influences on the atmospheric circulations could be found in model simulations by Rinke et al. (2008), which can be explained by the large area of Arctic and subarctic landmass where the surface conditions are dominated by such a moss layer. Furthermore, the important role of the ground heat flux in the surface energy balance in cold permafrost areas such as Northern Siberia, especially during the polar winter (see Figure 5.12), enhances such feedbacks of soil surface properties on atmospheric dynamics.

Heat flux through the surface layer

Average heat fluxes at shallow depths in the soil can be expected to follow the surface heat flux with a certain lag that is based on the thermal diffusivity of the overlaying soil layer. When considering heat fluxes averaged over periods longer than a few days, the values become comparable because the daily cycle is averaged out. This assumes that the storage of energy in the overlaying soil layer is small against the heat fluxes over that period. This is not the case for periods of freezing and thawing of the soil when the transformation of latent heat in that layer accounts for most of the transported thermal energy.

The simulated and measured heat fluxes in the soil displayed in Figure 5.10 can be set into comparison with the energy turnover in the active layer. The latent heat that is transformed during freezing and thawing of the entire active layer can be calculated according to (2.13). The maximum thaw depth is around 45 cm in the centre of the polygon and 0.75 cm in the rim of the polygon, which can be inferred from the results of Chapter 5.2. The average soil water contents in the active layer are $\langle \theta_w \rangle_z = 0.70$ in the centre and $\langle \theta_w \rangle_z = 0.45$ in the rim of the polygon. This leads to an almost equal energy turnover of about $1 \cdot 10^8 \text{ J m}^{-2}$ at both profiles in the phase change of the active layer. Assuming heat fluxes of 10 W m^{-2} that calculation yields a time span of four months to freeze or thaw the entire active layer at the site while a heat flux of 20 W m^{-2} implies a freezing period of two entire months. It is assumed that there is no heat flux from or to deeper soil layers into the isothermal plateau. This is approximately the case due to the small temperature gradients at that depth (see also Fig. 5.4).

The length of the zero curtain in the soil temperature measurements (see Figure 5.5 and Figure 5.6) is slightly longer than two month at both profiles and in both years of the model period. The simulated heat fluxes of 15 W m^{-2} at the rim of the polygon and 20 W m^{-2} at the centre of the polygon consequently have the right magnitude. Thus, the strong difference in the timing of the refreezing between the simulations and the measurements at the rim of the polygon during the second winter (see Figure 5.9) cannot be directly attributed to a wrong description of the soil heat flux during the refreezing period in autumn.

The heat fluxes of less than 10 W m^{-2} measured by the heat-flux plates, however, are not large enough to be consistent with the observed timing of the freezing of the active layer. The problems of the application of this method in several types of soil have been discussed in the literature (Sauer et al., 2003; Halliwell and Rouse, 1987) and can be predominantly attributed to the difference in thermal diffusivity between the material of the heat flux plate and the surrounding soil. Furthermore, latent heat transfer is not captured. The thermal conductivity of the heat flux plate is specified with $0.8 \text{ W K}^{-1} \text{ m}^{-1}$, which is in the range of the thermal conductivities that are obtained in the unfrozen soils (Williams and Smith, 1989). This explains the good accordance between measurements and modelled values for the summer months. The thermal conductivity of the frozen soil, however, is much higher due to the higher conductivity of ice compared to water. Hence, the measured heat fluxes during the winter months are underestimated because the measurement method is based on the assumption of comparable heat conductivity in the sensor and in the surrounding material. Thus, the measurements of the heat flux plates are discarded for the periods of frozen ground in the analysis of the model performance. A correction of the measured heat fluxes may be possible based on the soil temperature measurement close by and assumptions on the composition of the surrounding soil.

Snow cover

Several aspects of the simulated temperature dynamics can be directly attributed to the description of the snow cover in the model.

The comparison of the outgoing short-wave radiation to the corresponding measurements in Figure 5.11 indicates that the surface albedo simulated in the model is reflecting the measured value accurately for most of the year, which includes both vegetation cover in summer and snow cover in winter. Due to the symmetric shape these data points can be attributed to periods during which the existence of a snow cover does not agree with the real situation. The data points with underestimated outgoing short-wave radiation in between these three linear clusters describe periods of incomplete snow cover during which the simulations do not show any snow cover at all. These situations can be found in the daily images by an automatic camera both during the on-set of the snow cover in October and November and in the melt period from April to June.

For both profiles the measurements show a strong warming peak in late winter. The temperature increase is visible in all sensors and penetrates down to the lowest

sensors at depths of more than 70 cm. These events are reproduced very well in the simulation based on the upper boundary forcing from temperature measurements at 3 cm depth. Thus, it can be ruled out that a wrong description of the heat transfer processes in the deeper soil layers causes these deviations. In the simulations with the surface energy balance calculation coupled to the soil model as an upper boundary, these events are not represented. Hence, this feature can be identified as a process at the surface or in the uppermost soil layer. The strong warming leads to strong deviations of about 10 °C between the measured soil temperatures and the model results for a period of about half a month. The temperature curves reach the same summer temperatures as in the measurements. This can be explained by the fact that the latent heat conversion during the thawing of the soil includes a much larger heat exchange than the pure heating of frozen ground. However, these deviations have a distinct influence on the mean annual soil temperature. According to the time scale and the temperature deviations during these events a change of the mean annual soil temperature of 0.5 °C can be expected.

The outgoing short-wave radiation shows distinct periods of low values that occur at the same dates as the warming events in the soil. Therefore, these events can be clearly attributed to abrupt changes in the snow layer, that lead to both a higher albedo and increased heat fluxes into the soil. The images of the automatic camera reveal, that these periods are characterised by a partial melt of the snow cover. This includes snow free areas on the rims of the polygons and clearly visible changes of the snow cover in the centre of the polygon, including some standing water. The underestimation of the heat transfer into the soil can be explained by the drastically lower albedo of the snow free surface on the rim of the polygons and enhanced heat transfer in the uppermost soil layer. Here infiltrating melt water leads both to convective heat transfer and to an increased heat conductivity. These effects are limited to the uppermost 3 cm of the soil as the simulations of heat transfer below the uppermost soil sensors shows no influences of these processes.

The measurement data used for the forcing of the snow layer in this study only consists of the snow depth measurements at one specific spot in the centre of the polygon. Therefore, the effect of the microtopography on the snow layer cannot be represented based on direct measurement data. The choice of a threshold snow depth of 4 cm on the rim of the polygon has proven to be reasonable since the soil temperatures are represented well during the course of the first winter and during the later period of the second winter. However, the second winter shows a strong overestimation of the soil cooling during the early freezing period. Test runs with a higher threshold for the snow cover on the rim shows a comparable overestimation of the freezing in autumn. However, the soil temperatures over the course of the later winter are simulated to high in these runs, so that the threshold value chosen here seems appropriate and is not the cause of the temperature deviations. The images from the automatic camera indicate that the rims of the polygons were partly snow covered during large periods of September and October 2011, which adds additional insulation to the ground surface during the initial cooling period at the transition from summer to winter. This is not covered by the snow depth measurements and

can be seen as the main reason for the deviations in the rim of the polygon during the freezing period.

Surface energy balance and energy partition

The comparison of the surface energy balance components from the coupled model simulations in Figure 4.1 with two measurement studies of energy partition at the surface for the study site shows, that the model is capable of representing the characteristics of the energy fluxes at the surface for the examined periods in the summer months and during the polar winter conditions. The comparison of the simulations results with the measurements from the two previous studies (Kutzbach, 2006; Langer et al., 2011b) is limited due to the consideration the same periods in different years. Furthermore the errors of the measured surface energy balance components (up to 30 %) have to be taken into account.

However, the strong average sensible heat flux of more than 80 W m^{-2} that is obtained in May 2011 seems overestimated and can be attributed to a mismatch between simulated and measured snow cover. This leads to a situation where the measured air temperature over snow or melting snow and the simulated temperature of the snow-free surface lead to an overestimation of the temperature gradient that the calculation of the sensible heat is based on. During the winter period, the thermal regime at the surface is dominated by the negative net radiation due to the emission of long-wave radiation from the surface. This flux is mainly controlled by the strong ground heat flux whereas the turbulent fluxes are comparatively small and partially cancel each other. The situation is represented well by the modelled surface energy balance. However, both the sensible and the latent heat fluxes are relatively small compared to the fluxes in the examined measurement study. This can be explained by differences in the air temperature, where a warmer average temperature would lead to both an increase in sensible heat flux towards the surface and stronger latent heat flux due to increased sublimation.

The derivation of the equations for the surface energy balance calculation assumes a completely flat surface for all descriptions of the physical processes of heat exchange. In reality this strict assumption is violated on different scales. The microtopography of the landscape described in 2.4 is not a flat or homogeneous surface. It introduces variations to the surface, that are on a length scale much larger than the one of the variations described by the roughness length z_0 . Furthermore, there is a distinct lateral variation in the surface properties that is not part of the assumptions of the theory.

The structure on a scale of centimetres to millimetres is highly variable due to the vegetation cover that includes both mosses and higher grass plants. This affects different parts of the surface energy balance calculation. Furthermore the actual position of the soil surface is difficult to determine as almost all the surface is covered by moss layer without any bare soil in direct contact to the atmosphere that could be chosen as a distinct surface position. In this study the upper surface of continuous moss cover is chosen as the soil surface. A certain fraction of the incom-

ing radiation in both wavelength bands is not reaching the soil, but is absorbed and remitted from parts of the vegetation cover above the ground. All these processes are not explicitly covered in the model description. However, these processes are incorporated to some extent into the effective surface properties such as albedo, surface resistance to evapotranspiration, roughness length, and emissivity.

Summary

The soil heat transfer below the surface layer is represented accurately by the model scheme with mean absolute errors of less than 1 °C. The annual cycle of the soil temperatures is represented reasonably by the coupled model for most periods of the year. Yet, the model shows strong deviations from the measurements during spring and early winter, with temperature deviations of up to 10 °C for limited periods. This is especially the case for the simulations at the rim of the polygon. These deviations lead to an underestimation of the mean annual temperature in the ground, that is on the order of 1–1.5 °C depending on the depth. These can be mainly attributed to the limitations in the description of the variable and heterogeneous snow layer. This includes the simplified approach of constant thermal properties and the limited data basis of only one snow depth measurement in the centre of the polygon. The energy balance calculation based on the radiative and turbulent heat fluxes yields good results for periods of the year that are not affected by the description of the snow cover and is in good agreement with the measured energy partition during previous years.

It can be expected that the two-dimensional version of the model can be used to simulate realistic thermal dynamics inside the polygon. That allows to identify and quantify the importance of the effects of lateral heterogeneity in the studied landscape elements. However, the deviations during the freezing period and prior to the thawing period that appeared in this model assessment have to be taken into account in the analysis of the results of the two-dimensional model.

6 Two-dimensional simulations of the thermal dynamics of a polygon

The two-dimensional version of the coupled model describing soil heat transfer, snow cover and surface energy balance in the polygon is used to study the influence of lateral variations and lateral heat transfer processes on the thermal dynamics of the system. These effects can not be described explicitly in one-dimensional models. On the one hand, this includes the actual transfer of heat by conductive processes in horizontal directions due to lateral temperature differences inside the soil. On the other hand, the lateral variations of soil and surface properties can lead to strong lateral differences in the vertical heat transfer processes. The influence of these differences are not trivial since several nonlinear processes play an important role in the system, e.g. the phase change of water in the soil or the energy partition at the surface.

- i) A two-dimensional simulation of the thermal dynamics of the polygon is used for the direct investigations of the pathways of heat fluxes to detect periods of strong lateral heat transfer and to quantify the importance of the lateral fluxes.
- ii) The influence of the representation of both lateral variations in the vertical heat transfer processes and direct lateral heat fluxes in model formulations of the thermal dynamics is investigated by comparing simulations of different complexity. This includes a detailed two-dimensional model with lateral heat fluxes and two simplified one-dimensional model descriptions with laterally averaged parameters.

6.1 Two-dimensional heat fluxes in the polygon

The two-dimensional model configuration is used based on the description of the model set-up in Chapter 4. The conductive heat fluxes are calculated from the resulting temperature field after the model simulation. The flux at each node is derived from the temperature gradient between the neighbouring cells and the thermal conductivity, that is calculated based on the temperature field with the same function used in the simulations. The magnitudes of the lateral heat fluxes and the vertical fluxes are compared on a time scale of months. Thus, the sum over the heat fluxes is not influenced by the diurnal cycle in the upper soil layer. The monthly average heat fluxes inside the polygon for the twelve months of the year 2011 are shown in Figure 6.1 (January to April), Figure 6.2 (May to August), and Figure 6.3 (September to December) with absolute value and local direction of the heat flux.

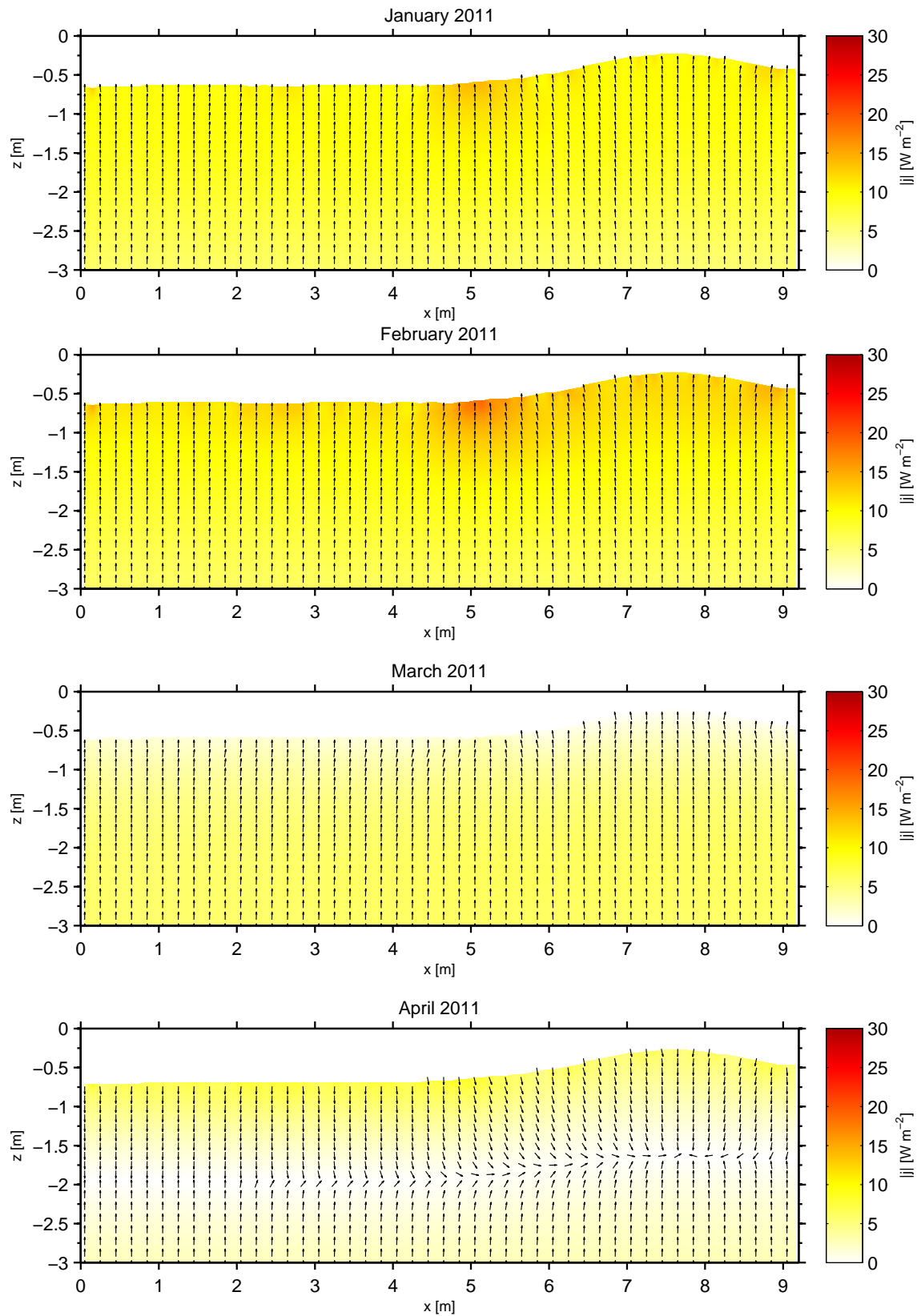


Figure 6.1: Monthly averaged conductive heat fluxes inside the polygon during January to April 2011. The colour denotes the magnitude of the absolute flux. The arrows show the flux and have equal length at all points.

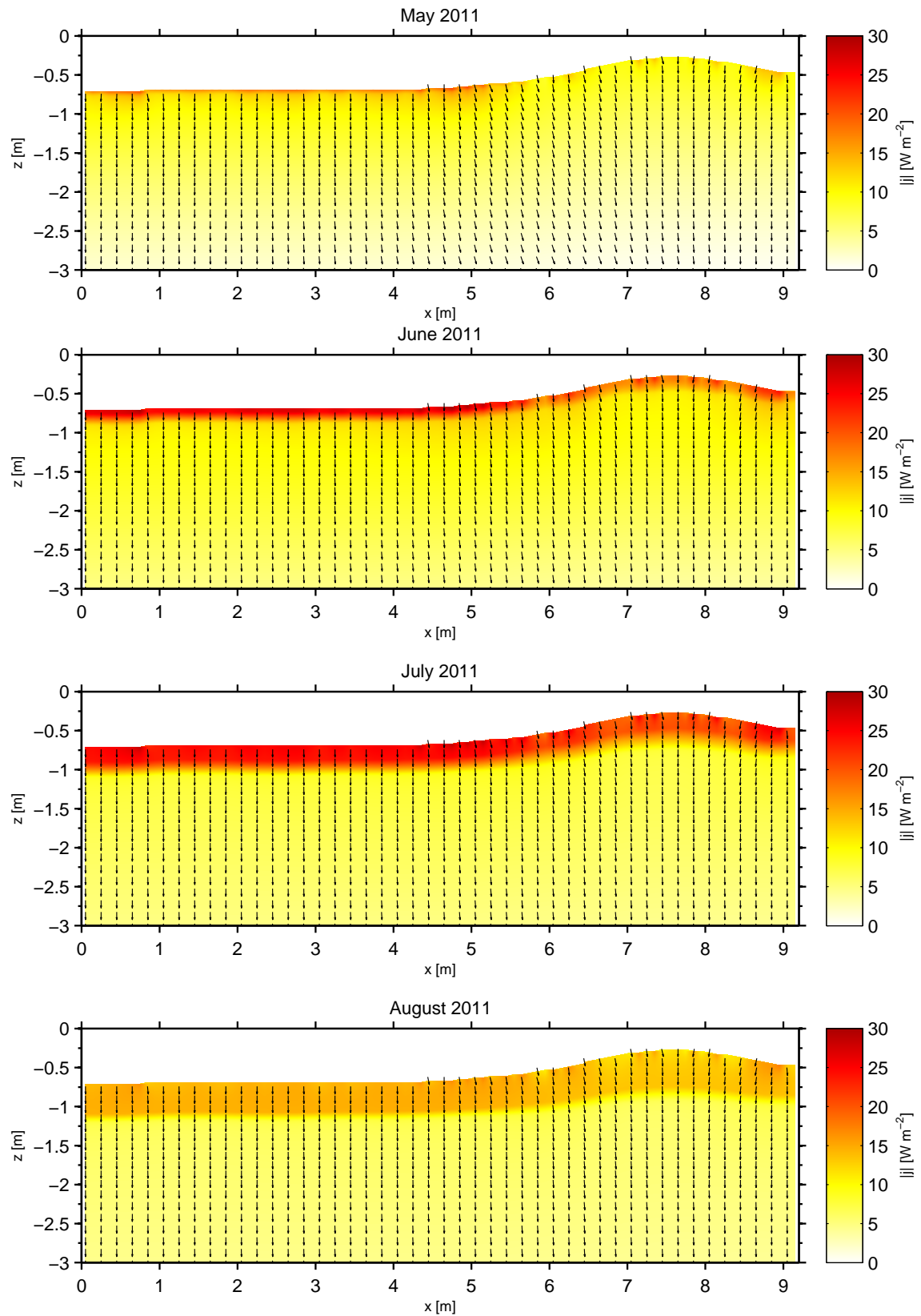


Figure 6.2: Monthly averaged conductive heat fluxes inside the polygon during May to August 2011. The colour denotes the magnitude of the absolute flux. The denote show the flux direction and have equal length at all points.

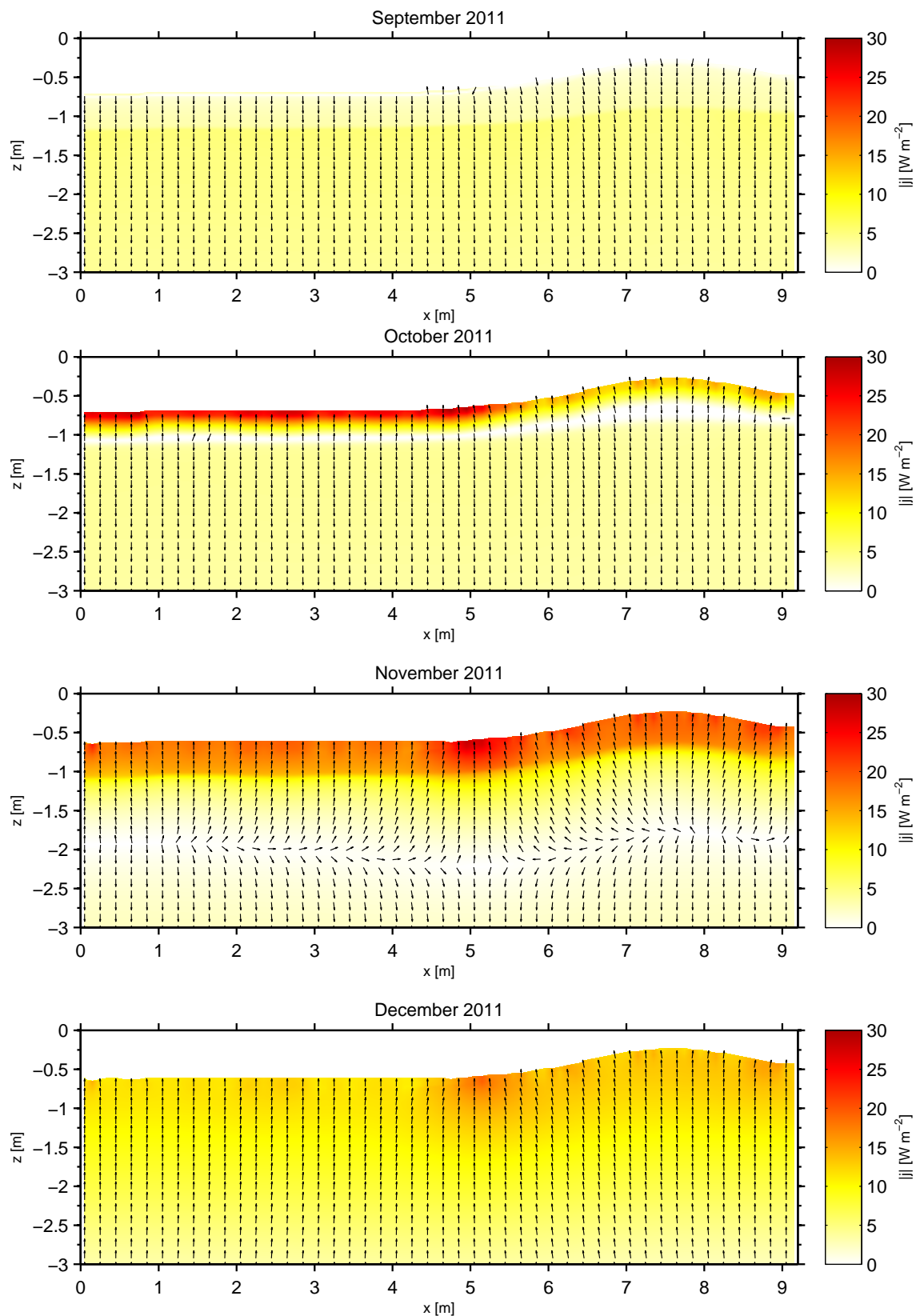


Figure 6.3: Monthly averaged conductive heat fluxes inside the polygon during September to December 2011. The colour denotes the magnitude of the absolute flux. The arrows show the flux direction and have equal length at all points.

The first three months of the year form the high winter with constantly low air temperature -20°C to -40°C (see Chapter 3.4). The soil is completely frozen during that period so that phase change processes in the soil do not play a role in the thermal dynamics of the system. The heat flux field is laterally very homogeneous showing a constant outflow of thermal energy towards the atmosphere at a rate of about 10 W m^{-2} . A stronger heat flux with some lateral components can be identified at the transition from the centre of the polygon to the polygonal rim.

In April, the averaged heat flux changes its sign in the upper soil layer with a warming at a rate of about 10 W m^{-2} . During the summer months the heat fluxes in the upper soil layer of the centre strongly exceed the heat fluxes at the same depths of the rim due to the higher conductivity of the top soil layer. Furthermore, the temperature gradient is larger due to the shallower thaw depth (see Chapter 5.3). August and September show a laterally homogeneous downward flux of energy with a distinct difference between the active layer and the frozen permafrost below. In October the refreezing of the active layer with heat fluxes towards the surface and to higher depths takes place, while November is already characterised by an average upward flux well below the active layer. Although only monthly averaged values are observed, a clear time delay in the refreezing between the centre and the rim of the polygon can be identified. While the average heat fluxes close to the surface reach values above 20 W m^{-2} in the centre during October, fluxes are only about half as large in the rim. In November the flux field is characterised by strong heat fluxes towards the surface in the active layer where the lateral heat exchange in the freezing process delivers a lot of energy. In contrast, December already shows a comparable picture to the following winter months with a rather homogeneous flux field and no influences of the conversion of latent heat in the active layer.

Purely lateral heat fluxes occur mainly at the stages when the vertical heat flux vanishes during the transition from upwards directed heat fluxes to fluxes directed downwards and vice versa. However, these situations are also characterised by low absolute heat fluxes. Thus, the lateral heat flux components during these periods are not significant compared to the heat fluxes during the rest of the year.

Figure 6.4 shows the laterally averaged lateral heat fluxes. The value given is the mean of the thermal energy transported through all ring-shaped radial cell interfaces per unit time. The values are given as the mean for each month and separately for both inward and outward direction. The maximum lateral heat fluxes are reached close to the surface with values of up to 40 W m^{-1} in both radial directions. The maximum lateral heat fluxes in the one-month periods decrease with depth and do not exceed 10 W m^{-1} at depths of more than 3 m. The averaged values over the two year period are very symmetric around the z-axis, indicating that the fluxes balance each other over the course of the year. Close to the surface of the polygon, average lateral heat fluxes of 15 W m^{-1} are present in both directions and decrease strongly with depth. These heat fluxes must be compared to the sum of the vertical heat fluxes over the entire polygon with a surface area of $\pi(9.2\text{ m})^2 = 265\text{ m}^2$ and average surface heat fluxes on the order of 10 W m^{-2} . Thus, the vertical fluxes are on the order of two magnitudes larger than the average lateral heat fluxes.

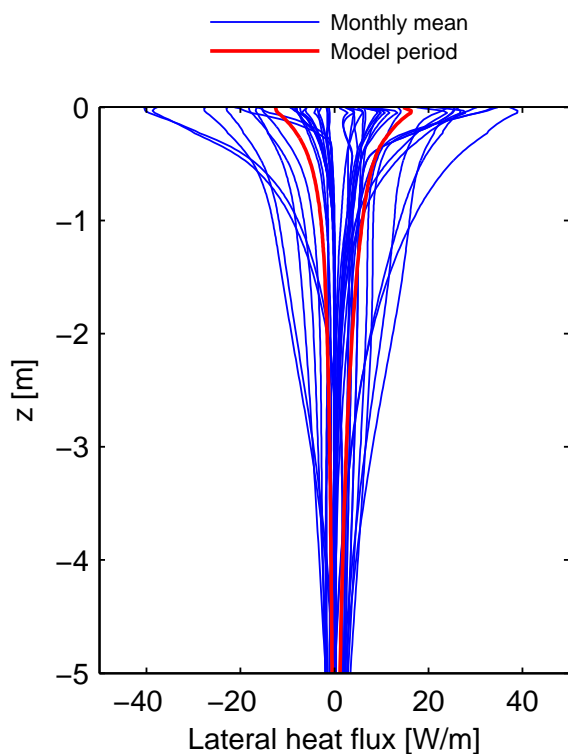


Figure 6.4: Monthly averaged lateral heat fluxes inside the polygon. Fluxes directed from the centre outwards (positive values) and fluxes inwards towards the centre of the cylindrical model domain (negative values) are averaged separately. The fluxes are given as mean values for the 24 individual months of the modelling period (blue). The averaged values over the two-year modelling period of is shown by the two red lines.

6.2 Comparison of model configurations of different complexity

The detailed two-dimensional simulation, as applied in the previous section, can be compared to modelling schemes that only feature one-dimensional heat transfer which are usually used for the simulation of permafrost at larger scales. This allows to investigate if the simplifications lead to deviations from the more complex model due to non-represented physical processes. The different models examined here are schematically displayed in Figure 6.5.

- Model **A** is the two-dimensional model in cylindrical coordinates with lateral heat fluxes used in the previous section. This includes a heterogeneous soil composition that varies both with depth and in the lateral dimension, i.e. with the radius in this model formulation. The microtopography is represented by a fixed surface position for each column of the model. The snow cover development and the surface energy balance are calculated for each lateral coordinate separately. Averaged heat fluxes are used for the determination of the atmospheric stability conditions (see detailed description in Chapter 4).
- The second model configuration, Model **B**, features two distinct soil columns, one for the centre of the polygon and one for the rim of the polygon. These two columns are simulated separately with one-dimensional heat transfer in the soil. However, the two model compartments are coupled by a common

snow cover and surface energy balance scheme comparable to the one used in the 2D model.

- Model C is a single one-dimensional model configuration as used in 5.3.

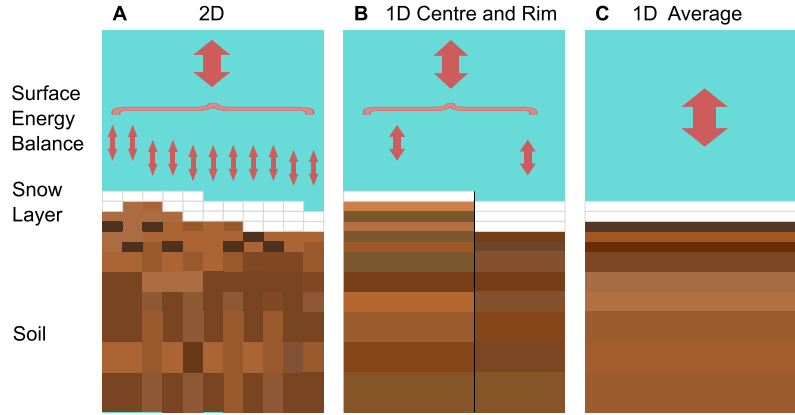


Figure 6.5: Schematic description of the three models used for the comparison of the performance of the models of different complexity.

A: Two-dimensional soil heat transfer with heterogeneous soil in cylindrical coordinates (radially symmetric), surface energy balance and snow depth for each surface grid cell.

B: One-dimensional simulations for the two characteristic compartments, centre and rim of the polygon, with averaged parameters for each compartment and coupled surface energy balance as well as snow cover calculations

C: One-dimensional simulation for horizontally averaged soil and surface parameters

All three models are initialised using the same data for temperature initial conditions, soil composition and surface characteristics. For the two-dimensional model the initialisation is set as described in Chapter 4 using the data depicted in Figure 4.5 and Figure 4.4. For the two simplified model configurations, soil composition, surface characteristics, and temperature initial conditions are set by horizontally averaging over the two-dimensional model domain of Model A at each depth. For Model B this is performed separately for the centre and the rim of the polygon. The initialisation of Model C is based on averages over the whole model domain. The weighted averages are calculated according to equation (4.15), which takes the cylindrical shape of the model domain into account. The vertical grid is chosen equal in all three model configurations. In Model C, the effect of the microtopography in the snow cover is realised by restricting the current snow depth d_{snow} such that a fraction corresponding to the rim of the polygon is kept at the threshold snow depth $d_{\text{snow,th}}$

$$d_{\text{snow}} < \frac{A_{\text{centre}}d_{\text{snow,centre}} + A_{\text{rim}}d_{\text{snow,th}}}{A_{\text{centre}} + A_{\text{rim}}}. \quad (6.1)$$

A_{centre} and A_{rim} denote the areas assigned to the centre or to the rim of the polygon in Model B and $d_{\text{snow,centre}}$ is the measured snow depth in the centre of the polygon.

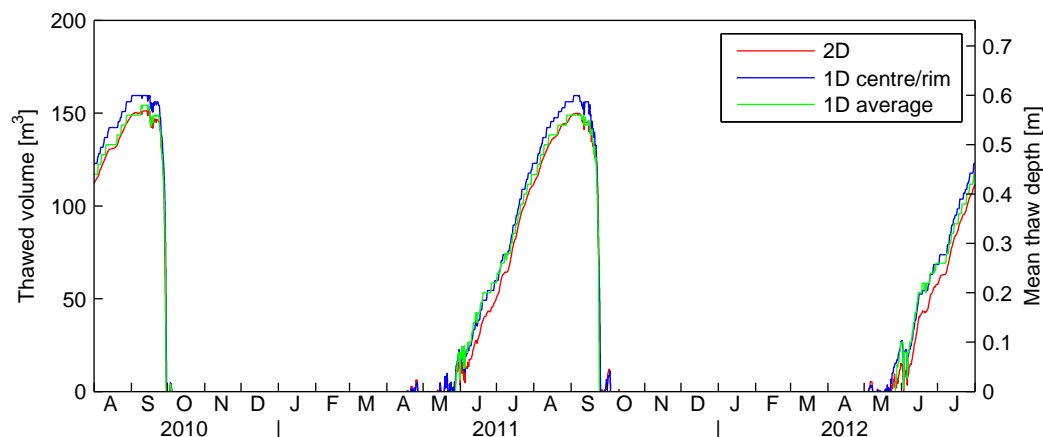


Figure 6.6: Volume of thawed soil inside the polygon and average thaw depth for the three different model configuration. Model A (2D simulation) in red, Model B (1D simulation for centre and rim separately) in blue and Model C (1D simulation) in green.

The actual modelling period of two years is the same as in the previous simulations. However, the model is run for a spin-up period of 10 years after the initialisation with the measured temperature data. Due to the restricted data the forcing during this period is composed of randomly combining the two years of the modelling period for a total period of 10 years. This allows for an investigation of the differences between the simulated soil temperatures on a longer time scale. Furthermore the analysis of the results is not dominated by the effects of the initial temperature conditions, which might be rather non-physical for the simplified models due to the averaging process. This approach seems appropriate since the focus is set on the direct comparison of the three model configurations. However, this means that the simulation results cannot be directly compared to measurements in the soil and at the surface.

Figure 6.6 shows the total volume of thawed soil in the cylindrical model domain for all three model configurations. This directly converts to the mean thaw depth by taking into account surface area of the model domain. The three models show a very consistent behaviour. The two-dimensional simulation (Model A) and the one-dimensional (Model C) show almost equal maximum thaw depth of 0.57 m in both years. For Model B the thaw depth is about 3% larger, reaching 60 cm in both years. During the first weeks of the thawing until the end of June, the two simplified model simulations (Model B and Model C) show an almost equal development of the thawed volume.

The mean annual soil temperature for the three different models is displayed in Figure 6.7. It is calculated as the lateral mean temperature over the two years of the target period for each depth with weighted averaging according to equation (4.15). The mean annual surface temperature, which is defined as the mean temperature of the interface to the atmosphere, i.e. the top of the ground in summer and the top of the snow layer in winter, shows comparable temperatures of about $-11.1\text{ }^{\circ}\text{C}$

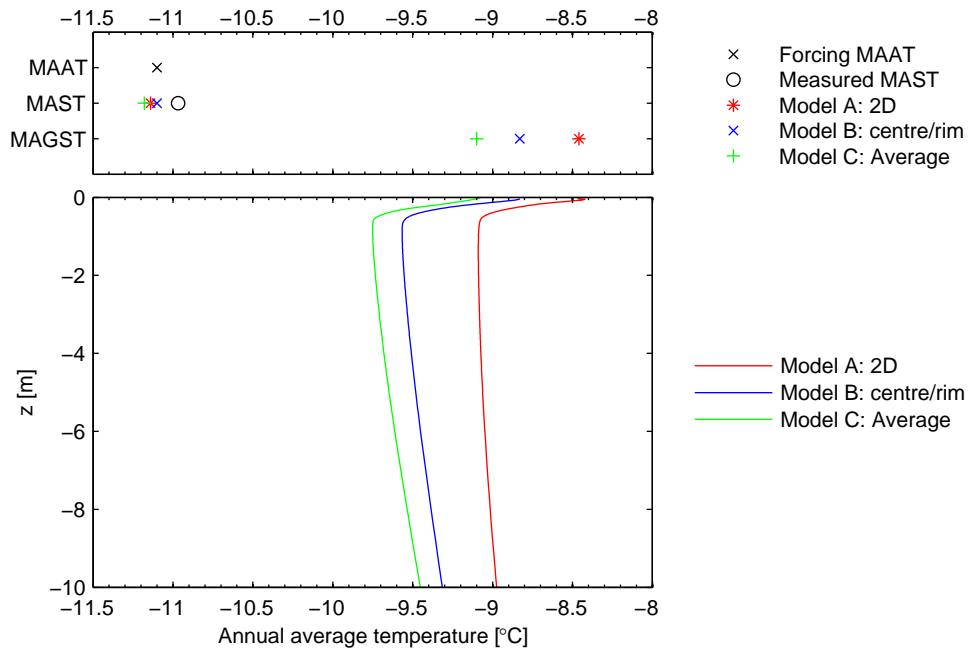


Figure 6.7: *Top:* Mean annual temperatures for the three model configurations, including the mean annual air temperature (MAAT), which is equal for all models as part of the forcing data, the mean annual surface temperature (MAST), i.e. the temperature at the surface of the ground or the snow cover, and mean annual ground surface temperature (MAGST) at the top of the soil domain.

Bottom: Mean annual soil temperature with depth over the two year target period for the three different models. Model A (2D simulation) in red, Model B (1D simulation for centre and rim separately) in blue, Model C (1D simulation) in green

to -11.2°C for all three model configurations. These temperatures are in good accordance with the MAST of -11.0°C that is derived from measurements of the four component radiation sensor and the mean annual air temperature (MAAT) of -11.1°C of the forcing data.

For Model A, the two-dimensional simulation, the mean annual ground surface temperature (MAGST) is -8.5°C . The temperature decreases with depth and reaches a minimum of about -9.1°C at a depth corresponding to the active layer thickness. For larger depths, the temperature slightly increases reaching -9°C at a depth of 10 m. The two other models show colder temperatures over the whole profile. The simulation with separate 1D-calculations for the centre and the rim of the polygon (Model B) shows a MAGST of -8.8°C . The permafrost right below the active layer has a minimum average temperature of around -9.6°C and increases to -9.3°C at 10 m. The simulation of one single soil column with averaged parameters (Model C) leads to an average temperature that is lower in the active layer, with a mean annual ground surface temperature of -9.1°C and -9.8°C at the top of the permafrost. The annual average temperature increases with depth and reaches -9.4°C at 10 m.

The difference in mean annual ground surface temperature reaches its maximum at a depth of about 0.5–1 m with a difference of 0.5 °C between Model A and Model B and 0.7 °C between Model A and Model C.

The mean annual temperature at the ground surface can be differentiated further into two distinct periods of the year. During the snow free summer months the surface temperature is identical to the ground surface temperature. Over the two year modelling period this value is almost identical for all three model configurations (Model A: 5.44 °C, Model B: 5.45 °C, Model C: 5.45 °C). During the snow covered period of the year, the surface temperature is taken at the surface of the snow cover and thus differs from the ground surface temperature at the bottom of the snow pack. The three models differ substantially in the average ground surface temperature during these parts of the modelling period (Model A: –18.27 °C, Model B: –18.75 °C, Model C: –19.16 °C).

A control run is performed with the same model scheme as Model A without lateral fluxes in the soil and snow compartment. Hence, the thermal dynamics are calculated one-dimensionally within each soil column/ring comparable to Model B, while the detailed description of the surface topography and the soil composition is retained. This simulation shows a mean temperature profile that is not distinguishable from the results obtained in Model A for most depths, with an identical MAST and slightly warmer average temperature at the top of the permafrost (by less than 0.05 °C).

Figure 6.8 compares the mean soil temperatures from the three different models as

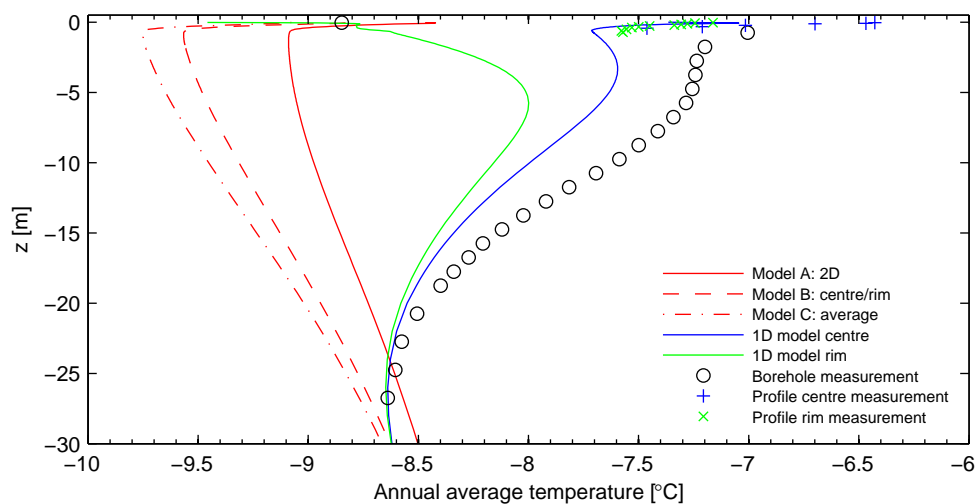


Figure 6.8: Mean annual surface temperature in a depth up to 20 m for different simulations and from measurements. The red curves are the three model configurations compared in this section as displayed in Figure 6.7. The blue and green curves show the results of the one-dimensional simulations in the centre and in the rim of the polygon. The markers give the mean temperature over the modelling period from the measurements in the borehole (black circles) and in the two soil profiles (blue: centre, green: rim).

in Figure 6.7 with averaged temperature measurements in the borehole and in the soil profiles in the active layer over the same period. Furthermore, the mean annual temperature profiles that evolve in the one-dimensional simulations in Chapter 5.3 are added.

These different average temperature profiles are not all directly comparable. The measured temperatures and the one dimensional simulation are showing the two year modeling period from summer 2010 to summer 2012. The average temperatures from the model comparison in this chapter, however, result from a simulation with the same forcing data after a 10 year initialisation. This explains the linear temperature gradient throughout the uppermost 30 m of the permafrost. The uppermost soil layers are in equilibrium with the surface forcing due to the 10 year initialisation period. The slope of the temperature curves differs according to the difference between the average temperature at the top of the permafrost and the temperature at a depth of about 30 m that is still determined by the initial temperature profile.

The three model simulations show a distinctly colder thermal regime than the measurements. The borehole temperatures are characterised by a strong temperature increase from -8.6°C at the deepest measurement point to about -7° at a depth of 1.75 m. The uppermost sensor of the borehole right at the surface is not taken into account. It cannot be expected to yield temperature values that are representative for the uppermost soil layer due to a stronger coupling to the air temperature via the metal rod of the borehole. The simulated mean annual temperatures derived from the one-dimensional simulations feature a distinct difference between the rim and the centre of the polygon. The mean annual temperature profile at the centre of the polygon is in rather good agreement with the measurements in the active layer and shows a comparable but shifted shape to the borehole measurements for larger depths. The average of the simulated soil temperatures at the rim of the polygon, however, is distinctly lower than the measurements. The temperature profile decreases towards the surface with a MAGST of -9.5°C . This value is distinctly colder than the average ground surface temperatures of the three models covering the whole cylindrical model domain that were discussed in detail in this section.

6.3 Discussion

Lateral heat fluxes inside the polygon

The detailed study of the monthly heat flux fields in Chapter 6.1 shows that lateral heat fluxes within the polygon are found at very distinct areas and only during limited periods. Strong lateral fluxes only occur at smaller depths corresponding to the active layer. Relevant lateral heat flux components can be found at two positions in the polygon. On the one hand, the pronounced topography of the polygonal rim with slanting surfaces leads to a lateral component of the strong heat fluxes near the surface even though these fluxes are directed orthogonal to the surface at that

specific point. On the other hand, the transition zone between the centre and the rim of the polygon acts as a kind of heat bridge during winter. This induces lateral heat fluxes from both the centre and the rim of the polygon towards that zone. The effect can be attributed to the strong insulation of both the comparatively thick snow cover above the centre of the polygon and the low conducting organic layer on top of the polygonal rim.

The explicit examination of the mean lateral heat fluxes in both directions in Figure 6.4 shows that the magnitude of the lateral fluxes over the course of the year is negligible compared with the vertical fluxes for the entire polygon. The measured snow cover in the polygon centre has been rather low during the two winters of the modelling period 2010-2012. A higher snow cover, however, which has been observed at the study site during several winters in previous years (Boike et al., 2013; Langer et al., 2011b), can be expected to enhance the lateral heat flux processes by forming a stronger barrier to heat flux in the centre of the polygon during the winter months. The same effect results from the formation of depth hoar in the snow cover, which can lead to a strongly decreased thermal conductivity as low as $0.02 \text{ W m}^{-1} \text{ K}^{-1}$ (Zhang et al., 1996; Sturm and Johnson, 1992). This process is not covered by the model scheme with constant and uniform snow thermal properties. Lateral heat fluxes are most pronounced in the transition zone between the rim and the centre of the polygon, where the freezing front and the thawing front show a sloping shape. Water filled polygon centres and polygonal ponds feature even stronger lateral variations in the thaw depth Langer et al. (2011b), leading to completely vertical freezing fronts due to the large storage of latent heat in the water bodies. Thus polygonal structures of comparable size that feature open water in the form of ponds can be expected to show a strongly increased influence of lateral heat fluxes on the thermal dynamics.

Ippisch (2001) performed two- and three-dimensional coupled simulations of heat and water transfer in soil structures on the scale of metres at a permafrost site on Svalbard. He did not find strong influences of lateral heat fluxes on the simulated results, either.

The influence of model complexity on the thermal dynamics

All three models show a distinct thermal offset between the temperature in the subsurface and the mean air temperature over the modelling period ($11.1 \text{ }^\circ\text{C}$) that can be traced back to the two different processes described in Chapter 2.4. The offset between ground surface temperature and the temperature at the top of the permafrost is of a comparable magnitude in all three models ($0.6\text{--}0.7 \text{ }^\circ\text{C}$). This indicates that the effects of latent heat and seasonal differences in heat conductivity creating this offset are represented consistently in all models.

The simulated surface temperatures of the different models over the course of the modelling period, however, are very consistent and agree within a range of $0.2 \text{ }^\circ\text{C}$. The measured mean annual surface temperature is slightly higher than the simulated values. This measurement is performed at one spot in the polygon. Thus, it is

not representative for the average over the entire polygon. It can be concluded that the surface energy balance is simulated coherently by the different models and not causing the temperature bias in the subsurface.

The mean annual ground surface temperature (MAGST) shows distinctly colder values of 0.65°C and 0.35°C for the two simplified models. These differences can be almost entirely attributed to differences in the mean ground surface temperature during the snow covered winter months that reach 0.8°C between Model A and Model C, whereas the surface temperatures in the snow-free periods differ between the three models by less than 0.05°C .

The deviations in the MAGST are almost equal to the offset between the temperatures in the soil for the three models. Therefore, the cold bias between the modelled permafrost temperatures can be attributed largely to differences in the simulation of the snow layer. This includes both the heat conduction through the snow layer and the timing of the snow covered period. The laterally averaged snow depth over the whole polygon differs little between the three models over most periods of the winter. The cold bias due to the representation of the heterogeneous snow cover in the microtopography of the landscape surface is added to the error that has to be expected from the uncertainties of the snow thermal properties (Langer et al., 2013; Goodrich, 1982) in modelling approaches. It has been shown that the correct representation of the Arctic tundra snow in model simulations has an impact on the simulated results regarding different aspects of the ecosystem such as carbon dynamics (Gouttevin et al., 2012). Furthermore, several studies indicate that the expected warming of the Arctic climate will be dominated by changes in the winter temperatures (Moritz et al., 2002; Johannessen et al., 2004). This adds further importance to the description of the thermal dynamics of the snow cover in permafrost models.

Due to the spin-up used in the simulations in this chapter, the resulting soil temperatures for the three different models cannot be compared directly to the soil temperatures measured in the soil profiles in the active layer and the borehole during the modelling period 2010-2012. However, the temperature profiles in 6.8 reveal, that the three model simulations yield soil temperatures that are distinctly colder than the measurements. The colder temperatures in the active layer and the upper permafrost layer can be attributed to the underestimation of the soil temperature introduced in coupled model simulations, that were discussed in detail in Chapter 5.2. These deviations affect two periods of the annual temperature cycle in the ground. During the early thawing period, the measured temperature increase in the soil is not represented in the simulations for both the centre and the rim of the polygon. Therefore, this effect is not expected to have a strong influence on the lateral dynamics in the polygon. The deviations during the freezing period, however are more pronounced for the rim of the polygon. This could influence on the lateral dynamics in the polygon. It has to be taken into account that the strong differences between the simulations and the measurement only occur during one winter, which means that the deviation must not be seen as a general weakness of the model. It

must rather be understood as the result of a situation in which the model forcing data does not reflect the real conditions properly.

The temperature at a larger depth of about 30 m depth can be expected to represent the mean annual temperature at the top of the permafrost over the course of a longer period. Therefore, the difference between this value and the measured temperatures at the top of the permafrost for the period 2010-2012 can be regarded as a lower boundary to the natural variation in the average soil temperature at the site. This difference amounts to about 1.5 °C. Thus, the simulated temperatures for the three models compared in this section lie within that range of the natural variation of the temperature dynamics at the study site. In summary, it can be concluded, that the comparison of the three models can yield meaningful conclusions about the influence of the model simplification on heat transfer.

The thawing process in the summer is simulated consistently by all three models with deviations of about 3 % in the thawed volume or average thaw depth. The good accordance between the three models can be explained by the linear relationship between the latent energy input needed to thaw the soil to a certain depth and the soil water content of the overlaying soil layer according to equation (2.13). The soil composition of the three models is based on the same interpolation of measurement data. The averaging preserves the total amount of water in the soil. The minor deviation between the models can be attributed to differences in the subsurface temperatures at the onset of thawing. The simulated mean active layer thickness of 55–60 cm is higher than the averaged active layer thickness of 50 cm that has been obtained over the course of several years in a mess plot close to the study site (Boike et al., 2013). However, variations of the thaw depth between individual polygons have to be expected due to the variability in soil composition and vegetation cover between the different polygons of the landscape unit (Kutzbach, 2006).

Langer et al. (2013) performed a sensitivity study for permafrost monitoring based on remote sensing data for the same study site. The variations of the mean annual soil temperature in the permafrost were found to be mainly determined by the properties of the snow cover during winter times. They show that the active layer thickness is predominantly tied to the soil composition, especially to the soil water content that determines the latent heat exchange during thawing. Goodrich (1982) has shown that summer thaw depth of permafrost is only slightly affected by the differences in the snow cover, whereas mean soil temperatures and the thermal offset are strongly affected by changes in the snow layer properties. Hence, the results of these two studies are in good agreement with the results obtained from the model comparison in this Chapter.

In large scale models, such as global or regional climate models, the effects of land surface heterogeneities on sub-grid scales are treated with different approaches. Calculations are often based on averaged surface and subsurface parameters for a whole grid cell, which corresponds to Model C in this study (Roeckner et al., 2003; Ekici et al., 2013). A large number of models feature sub-grid schemes in their land surface schemes that include the surface energy balance (Ducoudré et al., 1993). Such

sub-grid methods are comparable to the approach of Model B in this study in that the different compartments of the grid cell are treated independently and then averaged in terms of the relevant output data or model variables.

The results of the model comparison show that the representation of the heterogeneous snow cover in terrain with pronounced microtopography can lead to a bias in permafrost temperature simulations of 0.5–1 K. This deviations are relevant for midterm projections on the development of the thermal state of permafrost where temperature changes of the same magnitude can be expected (Romanovsky et al., 2010a,b; Smith et al., 2010). Thus, a correct representation of the energy balance of the ground during the winter months in landscapes with comparable topography heavily relies on a correct description of the snow cover in the models. The heterogeneity in the soil composition and lateral heat fluxes within the polygonal soil structures do not show a substantial influence on the thermal dynamics for the specific case studied here. However, stronger variations of the soil compartment, such as the presence of open water surfaces in the system and a stronger insulating snow cover, could lead to a well-marked influence of these processes.

7 Conclusions and outlook

In this thesis, a numerical model has been used to study the thermal dynamics of permafrost soil in a typical polygonal tundra landscape in the Siberian Arctic. An existing permafrost model including conductive heat transfer and the phase change of water has been extended in several aspects to simulate laterally extended soil and surface structures. A two dimensional formulation of the model in cylindrical coordinates has been developed assuming radial symmetry of the polygons. The model has been coupled to a surface energy balance calculation based on meteorological measurements. Hence, the model is capable of representing lateral variations in soil and surface parameters and includes the explicit calculation of lateral heat fluxes.

The quality of the model simulations has been assessed in several steps with regard to the intended use in the two-dimensional simulations. The numerical model reproduces the analytical solutions of Stefan problems both in a one-dimensional and in a two-dimensional cylindrical case. The model simulations of conductive soil heat transfer excluding the processes at the soil surface show a good agreement with measured soil temperatures and mean absolute errors of less than 1 °C. Hence, the thermal dynamics in the subsurface at the study site can be described accurately by heat conduction and the phase change of water with the chosen parametrisation of the soil. The coupled simulations of soil heat transfer, surface energy balance and snow cover development show a larger deviation from the measurements, especially at the polygonal rim. Strong deviations occur for limited time during the freezing process and at the onset of the thawing period. The description of the snow cover has been identified as the main cause of these deviations. This includes the insufficient representation of the lateral heterogeneity of the snow depth in the model forcing and the assumption of constant thermal properties. The model description of the surface energy balance yields an accurate description of the energy partition at the surface and of the ground heat flux during the periods of the year that are not affected deviations in the snow cover. The correct description of the organic layer at the top of the soil is crucial to correctly simulate the subsurface temperatures. This demand is not restricted to the specific site studied here, but also applies for large fractions of the Arctic that are characterised by a comparable surface vegetation. The two-dimensional simulations of the thermal dynamic in the polygon reveal that lateral heat fluxes inside the polygon only occur very localised and during restricted periods. The average lateral fluxes are very small compared to the vertical fluxes. The effect on the thermal state of the permafrost has proven to be almost negligible. A comparison of three model configurations of different complexity shows, that a simplified description of the thermal dynamics in one-dimensional model schemes with averaged soil and surface parameters leads to a cold bias of up to 0.7 °C in

the simulated mean annual permafrost temperatures. This can be attributed to the representation of the strongly heterogeneous snow cover in the different model schemes. The average thaw depth in the active layer is represented consistently by the different models. The results of this study have implications for representation of patterned ground structures in large scale permafrost modelling. This is, for instance, relevant to the description of the carbon cycle in global climate models or assessments of the influences of climatic changes to the Arctic ecosystems. Given an appropriate averaging of the soil parameters, the mean active layer thickness can be represented well even for strongly heterogeneous landscapes such as the polygonal tundra. The heterogeneity of the snow cover has to be taken into account in the model calculations to avoid biases in the simulations of the thermal state of permafrost. This is not restricted to the polygonal tundra, but also applies to heterogeneities in the snow cover on larger scales. Lateral heat fluxes on the scale of metres, however, can be safely neglected for the landscape type of polygonal tundra.

Two main implications for further research arise from the limitations that have shown up in the course of the work or from additional physical processes that have not been covered in the scope of this thesis:

A new soil monitoring station comparable to the measurement set-up used in this study has been set up on Samoylov Island in 2012. This will provide the opportunity to conduct similar studies at an additional site with slightly different conditions and additional measurement sensors. This includes, for instance, separate four-component radiation sensors above the rim and the centre of the polygon and temperature sensors down to the uppermost permafrost layers. Furthermore, a measurement set-up for detailed monitoring of the spatial and temporal variations in the snow cover thickness, snow properties and surface temperature has been established. These data sources can be used for a better determination of different model parameters. The implementation of an enhanced modelling scheme for the snow cover can include variations in the thermal properties and a better description of the influence of the microtopography on the snow depth.

In this study, the heterogeneity of the surface and subsurface properties has been restricted to the differences between the wet polygon centres and the dry rims of the polygons. In high latitude lowlands, water bodies of different scale are an important feature of the heterogeneous surface cover (Muster et al., 2013). In the polygonal tundra, these water bodies occur in the form of polygonal ponds. The additional physical compartment of the water body adds physical processes to the system, which could lead to a stronger influence of the lateral structure on the thermal dynamics of the ground (Langer et al., 2011b; Wischnewski, 2013). The two-dimensional model configuration with surface-energy balance coupling developed in this thesis can be extended by a basic description of the thermal dynamics in the water bodies to investigate the thermal dynamics of these systems.

Acknowledgements

At this point I would like to thank a number of people who played an important role during my work on this thesis. I will stick to German here since that would be the natural way of addressing most of the people mentioned here.

An dieser Stelle möchte ich einer Reihe von Personen danken, die während der Bearbeitungszeit dieser Masterarbeit eine wichtige Rolle gespielt haben und auf ihre ganz unterschiedliche Weise zum ihrem Gelingen beigetragen haben.

- Ich bedanke mich bei Kurt Roth für die anregenden, fordernden und motivierenden Diskussion über die Fragestellungen dieser Arbeit, die nötigen Freiheiten bei der Umsetzung des Themas und die Unterstützung wann immer diese nötig war.
- Ganz besonders danke ich Moritz Langer für die umfassende Betreuung dieser Masterarbeit. Das reicht von der gemeinsamen Ausarbeitung des Themas über die Einführung in die Feldarbeit in der Tundra, die großartigen Motivationskünste bis hin zu all den Unterstützungen und Anregungen, auf die man immer sich verlassen konnte.
- Julia Boike danke ich ganz herzlich für die Begleitung dieser Masterarbeit und viele anregende Diskussionen, besonders im Rahmen der gemeinsamen Feldarbeit in Sibirien.
- Die Expedition ins Lena-Delta im Sommer 2012 wird für mich immer eine prägende Erfahrung bleiben - nicht nur wegen der beeindruckenden Landschaft im Norden Sibiriens, sondern ganz besonders wegen der übrigen Expeditionsteilnehmer, die diesen Sommer am Ende der Welt zu einer besonderen Erinnerung gemacht haben.
- Bei Ingeborg Levin möchte ich mich für die Übernahme der Zweitkorrektur meiner Arbeit und das Interesse am bearbeiteten Thema bedanken.
- Den SPARCs am AWI in Potsdam, Karo, Sina, Niko, Konny, Sebastian,... danke ich ganz herzlich für inzwischen zweieinhalb Jahre mit spannender Polarforschung, toller Atmosphäre, lebhaften Diskussionen und der nötigen Menge Spaß.
- Ich möchte mich ganz herzlich meinen Eltern und meiner Schwester bedanken, die mich zu allen Zeiten hervorragend unterstützt und motiviert haben.
- Ein besonderer Dank geht an Freya, Steffi, Jonas, Daniel, Axel und viele weitere, die in den vergangenen beiden Jahren von Kommilitonen zu guten Freunden geworden sind. Danke für die tolle Zeit mit euch und dafür, dass ihr immer da wart, wenn ich euch gebraucht habe.
- Bei der Bodenphysikgruppe am IUP möchte ich für die angenehme und - bis auf die eiskalte GPR-Einführung - warme Arbeitsatmosphäre während Bearbeitungszeit meiner Masterarbeit bedanken.
- Alle, die mit beim Korrekturlesen dieser Arbeit geholfen haben, sollten sich jeweils schon irgendwo in dieser Auflistung wieder finden können und somit ein zweites Mal angesprochen fühlen.

8 Lists

8.1 List of Figures

2.1	Schematic Profile of a permafrost site	12
2.2	Annual cycle of permafrost soil	14
2.3	Heat transfer in a polygon	15
3.1	Location of the study site	18
3.2	Measurement site in different seasons	19
3.3	Topography and sensor positions in the polygon	20
3.4	Forcing data series	25
4.1	Surface energy balance scheme	29
4.2	Model discretisation	33
4.3	Snow and topography scheme	34
4.4	Initial temperature distribution in the polygon	38
4.5	Soil composition in the polygon for the two-dimensional simulations	39
5.1	One-dimensional Stefan problem	43
5.2	Two-dimensional Stefan problem	44
5.3	Schematic overview of the one-dimensional simulations	45
5.4	Temperature field for simulations forced with soil temperature data	46
5.5	Soil temperature in the polygon centre (forcing with soil temperature)	47
5.6	Soil temperature in the polygon rim (forcing with soil temperature)	48
5.7	Temperature fields for simulation forced with surface energy balance	50
5.8	Soil temperature in the polygon centre (forcing with SEB)	51
5.9	Soil temperature in the polygon rim (forcing with SEB)	52
5.10	Simulations and measurements of heat flux in the soil	53
5.11	Modelled and measured outgoing radiation	55
5.12	Components of the surface energy balance	56
5.13	Surface energy balance compared to previous studies	57
6.1	Heat fluxes inside the polygon (January to April 2011)	66
6.2	Heat fluxes inside the polygon (May to August 2011)	67
6.3	Heat fluxes inside the polygon (September to December 2011)	68
6.4	Lateral heat fluxes inside the polygon	70
6.5	Schematic description of the models of different complexity	71
6.6	Thawed volume and active layer thickness the model comparison	72
6.7	Mean annual temperature for the model comparison	73

6.8	Mean annual soil temperature, simulations and measurements	74
A.1	Freezing characteristics centre	97
A.2	Freezing characteristics rim I	98
A.3	Freezing characteristics rim II	99
A.4	Freezing characteristics slope	100
A.5	Temperature offset correction centre	101
A.6	Temperature offset correction rim	102
A.7	Temperature offset correction slope	102
A.8	Simulations and measurements of soil temperature in the rim (all sensors, forcing from temperature sensors)	103
A.9	Simulations and measurements of soil temperature in the rim (all sensors, forcing from temperature sensors)	104
A.10	Comparison modelled and measured soil temperature in the centre (all sensors, forcing from the surface energy balance)	105
A.11	Simulations and measurements of soil temperature in the rim (all sensors, forcing from surface energy balance)	106
A.12	Soil temperature with changes in surface layer (centre)	107
A.13	Soil temperature with changes in surface layer (rim)	108

8.2 List of Tables

3.1	Measurement sensors	21
4.1	Thermal properties of materials	37
4.2	Surface parameters used in the model	38

8.3 List of abbreviations and variables

variable	unit	quantity
ϕ	-	porosity
θ_w	-	soil water content
θ_{org}	-	soil ice content
θ_{min}	-	soil mineral content
θ_{org}	-	soil organic content
$\theta_{w,\text{min}}$	-	minimum liquid water content (below T_f)
a	K^{-1}	empirical constant in the freezing curve
b	K^{-1}	empirical constant in the freezing curve
T_f	K	temperature below which only $\theta_{w,\text{min}}$ liquid
T_{th}	K	temperature at which all water is liquid
k_h	$\text{J K}^{-1} \text{m}^{-1}$	volumetric thermal conductivity
c_h	$\text{J m}^{-3} \text{K}^{-1}$	volumetric heat capacity
c_{eff}	$\text{J m}^{-3} \text{K}^{-1}$	effective heat capacity
T	K, °C	temperature
RH	%	relative humidity
q	—	absolute humidity
u	m s^{-1}	wind speed
SEB		surface energy balance
Θ	K	potential temperature
Θ_v	K	potential virtual temperature
L	m	(Monin-)Obhukov length
u_*	m s^{-1}	shear velocity
ζ	-	dimensionless stability parameter
Q_{net}	W m^{-2}	net radiation
Q_{SW}	W m^{-2}	short-wave radiation (350–2800 nm (measurements))
Q_{LW}	W m^{-2}	long-wave radiation (4.5–50 μm (measurements))
Q_h	W m^{-2}	turbulent sensible heat flux
Q_e	W m^{-2}	turbulent latent heat flux
Q_g	W m^{-2}	ground heat flux (heat flux through soil/snow surface)
A	—	albedo (vegetation cover/snow)
ε	—	surface emissivity (vegetation cover/snow)
z_0	m	surface roughness length
r_s	—	surface resistance to evapotranspiration

MAAT	°C	mean annual air temperature
MAST	°C	mean annual surface temperature
MAGST	°C	mean annual ground surface temperature
TTOP	°C	temperature at the top of permafrost
j_z	W m^{-2}	vertical heat flux in the soil
j_x	W m^{-2}	horizontal heat flux in the soil
g	m s^{-2}	gravitational acceleration

Natural constants and material properties

$\sigma = 5.670 \cdot 10^{-8} \text{ W m}^{-2} \text{ K}^{-4}$	Stefan-Boltzmann constant
$L_{s,l} = 0 \text{ J}$	latent heat of fusion of water
$L_{l,g} = 0 \text{ J}$	latent heat of evaporation of water
$\kappa = 0.4$	von Kármán constant

Orientation of directed properties:

In this thesis the z -axis is always chosen pointing downwards into the soil. The fluxes of heat or any other quantity in the soil are given according to that. The heat fluxes at the surface are given such that, with the exception of the radiative fluxes, where all components are chosen positive with a positive net radiation denoting energy transfer towards the surface.

9 Bibliography

- ACIA (2004). Impacts of a Warming Arctic-Arctic Climate Impact Assessments. *Impacts of a Warming Arctic-Arctic Climate Impact Assessment, by Arctic Climate Impact Assessment, Cambridge, UK: Cambridge University Press, December 2004.*, 1.
- Avissar, R. and Pielke, R. A. (1989). A parameterization of heterogeneous land surfaces for atmospheric numerical models and its impact on regional meteorology. *Monthly Weather Review*, 117(10):2113–2136.
- Barry, R. and Gan, T. Y. (2011). *The global cryosphere: past, present and future*. Cambridge University Press.
- Beringer, J., Lynch, A. H., Chapin III, F. S., Mack, M., and Bonan, G. B. (2001). The representation of arctic soils in the land surface model: the importance of mosses. *Journal of Climate*, 14(15):3324–3335.
- Boike, J., Ippisch, O., Overduin, P. P., Hagedorn, B., and Roth, K. (2008). Water, heat and solute dynamics of a mud boil, Spitsbergen. *Geomorphology*, 95(1):61–73.
- Boike, J., Kattenstroth, B., Abramova, K., Bornemann, N., Chetverova, A., Fedorova, I., Fröb, K., Grigoriev, M., Grüber, M., Kutzbach, L., Langer, M., Minke, M., Muster, S., Piel, K., Pfeiffer, E.-M., Stoof, G., Westermann, S., Wischniewski, K., Wille, C., and Hubberten, H.-W. (2013). Baseline characteristics of climate, permafrost and land cover from a new permafrost observatory in the Lena River Delta, Siberia (1998-2011). *Biogeosciences*, 10(3):2105–2128.
- Brown, J., Ferrians, O. J., Heginbottom, J., and Melnikov, E. (1997). *Circum-Arctic map of permafrost and ground-ice conditions*. US Geological Survey Reston.
- Brun, E., Martin, E., Simon, V., Gendre, C., and Coleou, C. (1989). An energy and mass model of snow cover suitable for operational avalanche forecasting. *Journal of Glaciology*, 35(12):1.
- Buckingham, E. (1914). On physically similar systems; illustrations of the use of dimensional equations. *Physical Review*, 4(4):345–376.
- Burn, C. and Smith, C. (1988). Observations of the "thermal offset" in near-surface mean annual ground temperatures at several sites near Mayo, Yukon Territory, Canada. *Arctic*, pages 99–104.
- Businger, J., Wyngaard, J., Izumi, Y., and Bradley, E. F. (1971). Flux-profile relationships in the atmospheric surface layer. *Journal of the Atmospheric Sciences*, 28(2):181–189.
- Campbell, G., Jungbauer Jr, J., Bidlake, W., and Hungerford, R. (1994). Predicting the effect of temperature on soil thermal conductivity. *Soil Science*, 158(5):307–313.
- Carslaw, H. S. and Jaeger, J. C. (1959). *Conduction of heat in solids*. Clarendon Press, Oxford, 2. ed. edition.
- Christiansen, H. H., Eitzelmüller, B., Isaksen, K., Juliussen, H., Farbrøt, H., Humlum, O., Johansson, M., Ingeman-Nielsen, T., Kristensen, L., Hjort, J., et al. (2010). The thermal state of permafrost in the nordic area during the international polar year 2007–2009. *Permafrost and Periglacial Processes*, 21(2):156–181.
- Courant, R., Friedrichs, K., and Lewy, H. (1928). Über die partiellen Differenzgleichungen der mathematischen Physik. *Mathematische Annalen*, 100(1):32–74.
- de Vries, D. (1963). Thermal properties of soils. *Physics of plant environment*, 1:57–109.

- Ducoudré, N. I., Laval, K., and Perrier, A. (1993). SECHIBA, a new set of parameterizations of the hydrologic exchanges at the land-atmosphere interface within the LMD atmospheric general circulation model. *Journal of Climate*, 6(2):248–273.
- Ekici, A., Beer, C., Hagemann, S., and Hauck, C. (2013). Improved soil physics for simulating high latitude permafrost regions by the JSBACH terrestrial ecosystem model. *Geoscientific Model Development Discussions*, 6(2):2655–2698.
- Foken, T. (2006). 50 Years of the Monin–Obukhov Similarity Theory. *Boundary-Layer Meteorology*, 119(3):431–447.
- Foken, T. (2008a). *Micrometeorology*. Springer, Berlin ; Heidelberg. Literaturverz. S. 265 - 293.
- Foken, T. (2008b). The energy balance closure problem: An overview. *Ecological Applications*, 18(6):1351–1367.
- French, H. M. (2007). *The periglacial environment*. Wiley, Chichester ; Weinheim [u.a.], 3. ed. edition. Includes bibliographical references and index.
- Giorgi, F. and Avissar, R. (1997). Representation of heterogeneity effects in earth system modeling: Experience from land surface modeling. *Reviews of Geophysics*, 35(4):413–437.
- Goodrich, L. (1982). The influence of snow cover on the ground thermal regime. *Canadian Geotechnical Journal*, 19(4):421–432.
- Gouttevin, I., Menegoz, M., Dominé, F., Krinner, G., Koven, C., Ciais, P., Tarnocai, C., and Boike, J. (2012). How the insulating properties of snow affect soil carbon distribution in the continental pan-Arctic area. *Journal of Geophysical Research: Biogeosciences (2005–2012)*, 117(G2).
- Grachev, A. A., Andreas, E. L., Fairall, C. W., Guest, P. S., and Persson, P. O. G. (2007). SHEBA flux–profile relationships in the stable atmospheric boundary layer. *Boundary-layer meteorology*, 124(3):315–333.
- Grigoriev, N. (1960). The temperature of permafrost in the Lena delta basin–deposit conditions and properties of the permafrost in Yakutia. *Yakutsk*, 2:97–101.
- Halliwell, D. H. and Rouse, W. R. (1987). Soil heat flux in permafrost: characteristics and accuracy of measurement. *Journal of Climatology*, 7(6):571–584.
- Hillel, D. (1982). *Introduction to soil physics*. Academic Press.
- Högström, U. (1988). Non-dimensional wind and temperature profiles in the atmospheric surface layer: A re-evaluation. *Boundary-Layer Meteorology*, 42(1-2):55–78.
- Högström, U. (1996). Review of some basic characteristics of the atmospheric surface layer. *Boundary-Layer Meteorology*, 78(3):215–246.
- IPCC (2007). Climate change 2007: The physical science basis, contribution of working group 1 to the fourth assessment report of the Intergovernmental Panel on Climate Change.
- Ippisch, O. (2001). *Coupled transport in natural porous media*. PhD thesis, Heidelberg, Univ., Diss., 2001.
- Johannessen, O. M., Bengtsson, L., Miles, M. W., Kuzmina, S. I., Semenov, V. A., Alekseev, G. V., Nagurnyi, A. P., Zakharov, V. F., Bobylev, L. P., Pettersson, L. H., et al. (2004). Arctic climate change: Observed and modelled temperature and sea-ice variability. *Tellus A*, 56(4):328–341.
- Kattenstroth, B. (2009). Long term climate, water balance and energy partitioning characteristics of a tundra site in the Lena River Delta, Siberia. Master’s thesis, University Potsdam.
- Kessler, M. and Werner, B. (2003). Self-organization of sorted patterned ground. *Science*, 299(5605):380–383.
- Kraus, H. (2008). *Grundlagen der Grenzschicht-Meteorologie*. SpringerLink : Bücher. Springer Berlin Heidelberg, Berlin, Heidelberg.

- Kutzbach, L. (2006). *The Exchange of Energy, Water and Carbon Dioxide between Wet Arctic Tundra and the Atmosphere at the Lena River Delta, Northern Siberia*. PhD thesis, Universität Hamburg.
- Lachenbruch, A. H. (1962). Mechanics of thermal contraction cracks and ice-wedge polygons in permafrost. *Geological Society of America Special Papers*, 70:1–66.
- Langer, M. (2010). *The Spatial and Temporal Variability of the Energy Balance at an Arctic Polygonal Tundra Site*. PhD thesis, University of Heidelberg, Combined Faculties for Natural Sciences and Mathematics.
- Langer, M., Westermann, S., Heikenfeld, M., Dorn, W., and Boike, J. (2013). Satellite-based modeling of permafrost temperatures in a tundra lowland landscape. *Remote Sensing of Environment*, 135:12–24.
- Langer, M., Westermann, S., Muster, S., Piel, K., and Boike, J. (2011a). The surface energy balance of a polygonal tundra site in northern Siberia - Part 1: Spring to fall. *The Cryosphere*, 5(1):151–171.
- Langer, M., Westermann, S., Muster, S., Piel, K., and Boike, J. (2011b). The surface energy balance of a polygonal tundra site in northern Siberia - Part 2: Winter. *The Cryosphere*, 5(2):509–524.
- Leffingwell, E. d. K. (1915). Ground-ice wedges: The dominant form of ground-ice on the north coast of Alaska. *The Journal of Geology*, 23(7):635–654.
- Ludin, A. R. (2010). Permafrost temperature analysis and projection from Samoylov Island in the Lena River Delta, Siberia. Master’s thesis, Heidelberg, Univ., Diplomarbeit, 2010.
- Mann, D. (2003). On patterned ground. *Science*, 299(5605):354–355.
- Martin, E. and Lejeune, Y. (1998). Turbulent fluxes above the snow surface. *Annals of Glaciology*, 26:179–183.
- Monin, A. and Obukhov, A. (1954). Basic laws of turbulent mixing in the surface layer of the atmosphere. *Trudy Geofiz. Inst. Acad. Nauk SSSR*, 24(151):163–187.
- Moritz, R. E., Bitz, C. M., and Steig, E. J. (2002). Dynamics of recent climate change in the Arctic. *Science*, 297(5586):1497–1502.
- Muster, S., Heim, B., Abnizova, A., and Boike, J. (2013). Water Body Distributions Across Scales: A Remote Sensing Based Comparison of Three Arctic Tundra Wetlands. *Remote Sensing*, 5(4):1498–1523.
- Plug, L. and Werner, B. (1998). A numerical model for the organization of ice-wedge networks. In *Permafrost Seventh International Conference Proceedings*, pages 897–902.
- Pollack, H. N., Hurter, S. J., and Johnson, J. R. (1993). Heat flow from the Earth’s interior: Analysis of the global data set. *Reviews of Geophysics*, 31(3):267–280.
- Prandtl, L. (1925). Bericht über Untersuchungen zur ausgebildeten Turbulenz. *Z. Angew. Math. Mech*, 5(2):136–139.
- Rinke, A., Kuhry, P., and Dethloff, K. (2008). Importance of a soil organic layer for Arctic climate: A sensitivity study with an Arctic RCM. *Geophysical Research Letters*, 35(13).
- Riseborough, D., Shiklomanov, N., Etzelmüller, B., Gruber, S., and Marchenko, S. (2008). Recent advances in permafrost modelling. *Permafrost and Periglacial Processes*, 19(2):137–156.
- Roeckner, E., Bäuml, G., Bonventura, L., Brokopf, R., Esch, M., Giorgetta, M., Hagemann, S., Kirchner, I., Kornbluh, L., Manzini, E., et al. (2003). The atmospheric general circulation model ECHAM5. PART I: Model description, Report 349, Max Planck Institute for Meteorology, Hamburg, Germany.
- Roedel, W. and Wagner, T. (2011). *Physik unserer Umwelt: Die Atmosphäre*. SpringerLink : Bücher. Springer Berlin Heidelberg, Berlin, Heidelberg.

- Rogers, C. A. (1958). The packing of equal spheres. *Proceedings of the London Mathematical Society*, 3(4):609–620.
- Romanovsky, N., Hubberten, H.-W., Gavrillov, A., Tumskey, V., and Kholodov, A. (2004). Permafrost of the east Siberian Arctic shelf and coastal lowlands. *Quaternary Science Reviews*, 23(11):1359–1369.
- Romanovsky, V., Drozdov, D., Oberman, N., Malkova, G., Kholodov, A., Marchenko, S., Moskalenko, N., Sergeev, D., Ukraintseva, N., Abramov, A., et al. (2010a). Thermal state of permafrost in Russia. *Permafrost and Periglacial Processes*, 21(2):136–155.
- Romanovsky, V. and Osterkamp, T. (1995). Interannual variations of the thermal regime of the active layer and near-surface permafrost in northern Alaska. *Permafrost and Periglacial Processes*, 6(4):313–335.
- Romanovsky, V. E., Smith, S. L., and Christiansen, H. H. (2010b). Permafrost thermal state in the polar Northern Hemisphere during the international polar year 2007–2009: A synthesis. *Permafrost and Periglacial Processes*, 21(2):106–116.
- Roth, K. (2012). Soil Physics, Lecture Notes, Institute of Environmental Physics, Heidelberg University.
- Roth, K. and Boike, J. (2001). Quantifying the thermal dynamics of a permafrost site near Ny-Ålesund, Svalbard. *Water Resources Research*, 37(12):2901–2914.
- Roth, K., Schulín, R., Flüher, H., and Attinger, W. (1990). Calibration of time domain reflectometry for water content measurement using a composite dielectric approach. *Water Resources Research*, 26(10):2267–2273.
- Sauer, T., Meek, D., Ochsner, T., Harris, A., and Horton, R. (2003). Errors in heat flux measurement by flux plates of contrasting design and thermal conductivity. *Vadose Zone Journal*, 2(4):580–588.
- Schuur, E. A., Vogel, J. G., Crummer, K. G., Lee, H., Sickman, J. O., and Osterkamp, T. E. (2009). The effect of permafrost thaw on old carbon release and net carbon exchange from tundra. *Nature*, 459(7246):556–559.
- Schwamborn, G., Rachold, V., and Grigoriev, M. N. (2002). Late Quaternary sedimentation history of the Lena Delta. *Quaternary International*, 89(1):119–134.
- Smith, S., Romanovsky, V., Lewkowicz, A., Burn, C., Allard, M., Clow, G., Yoshikawa, K., and Throop, J. (2010). Thermal state of permafrost in North America: A contribution to the International Polar Year. *Permafrost and Periglacial Processes*, 21(2):117–135.
- Stefan, J. (1890). Über die Theorie der Eisbildung. *Monatshefte für Mathematik*, 1(1):1–6.
- Sturm, M. and Johnson, J. B. (1992). Thermal conductivity measurements of depth hoar. *Journal of Geophysical Research: Solid Earth (1978–2012)*, 97(B2):2129–2139.
- Tarnocai, C., Canadell, J., Schuur, E., Kuhry, P., Mazhitova, G., and Zimov, S. (2009). Soil organic carbon pools in the northern circumpolar permafrost region. *Global biogeochemical cycles*, 23(2).
- van Everdingen, R. (1998). Multi-language glossary of permafrost and related ground-ice terms. Boulder, CO: National Snow and Ice Data Center.
- Washburn, A. L. (1980). *Geocryology: a survey of periglacial processes and environments*. Wiley.
- Weismüller, J. (2010). Modeling water and heat transport in permafrost soils. Master’s thesis, Heidelberg, Univ., Diplomarbeit, 2010.
- Weismüller, J., Wollschläger, U., Boike, J., Pan, X., Yu, Q., and Roth, K. (2011). Modeling the thermal dynamics of the active layer at two contrasting permafrost sites on Svalbard and on the Tibetan Plateau. *The Cryosphere*, 5(3):741–757.

- Weller, G. (1972). The tundra microclimate during snow-melt at Barrow, Alaska. *Arctic*, pages 291–300.
- Weller, G. and Holmgren, B. (1974). The microclimates of the Arctic Tundra. *Journal of Applied Meteorology*, 13:854–862.
- Westermann, S. (2010). *Sensitivity of permafrost*. PhD thesis, Heidelberg University.
- Westermann, S., Boike, J., Langer, M., Schuler, T., and Etzelmüller, B. (2011). Modeling the impact of wintertime rain events on the thermal regime of permafrost. *The Cryosphere Discussion*, 5:1697–1736.
- Westermann, S., Schuler, T., Gislås, K., and Etzelmüller, B. (2013). Transient thermal modeling of permafrost conditions in Southern Norway. *The Cryosphere, Volume 7, Issue 2, 2013*, pp. 719–739, 7:719–739.
- Williams, P. J. and Smith, M. W. (1989). *The frozen earth: fundamentals of geocryology*, volume 306. Cambridge University Press Cambridge.
- Wischnewski, K. (2013). Temperature Simulation Model for Small Water Bodies in the Arctic Tundra, Lena River Delta (Siberia, Russia). Master’s thesis, Swiss Federal Institute of Technology Zurich.
- Zhang, T. (2005). Influence of the seasonal snow cover on the ground thermal regime: An overview. *Reviews of Geophysics*, 43(4):RG4002.
- Zhang, T., Osterkamp, T., and Stamnes, K. (1996). Influence of the depth hoar layer of the seasonal snow cover on the ground thermal regime. *Water Resources Research*, 32(7):2075–2086.
- Zimov, S. A., Schuur, E. A., and Chapin III, F. S. (2006). Permafrost and the global carbon budget. *Science*, 312(5780):1612–1613.

A Appendix

A.1 Universal functions

The integrated forms of the stability functions according to (4.4)- (4.7) have been obtained analytically or numerically avoid the numerical integration during model runtime:

Universal functions after Högström (1996) for unstable conditions ($\zeta \leq 0$)

$$\varphi_m = (1 - 19.3\zeta)^{\frac{1}{4}} \quad (\text{A.1})$$

$$\begin{aligned} \psi_m(\zeta) &= \int_{z_0/L}^{z/L} \frac{1 - \phi_m(\zeta)}{\zeta} d\zeta \quad (\text{A.2}) \\ &= \left[-2 \arctan((1 - 19.3\zeta)^{\frac{1}{4}}) + 2 \ln(1 + (1 - 19.3\zeta)^{\frac{1}{4}}) \right. \\ &\quad \left. + \ln(1 + (1 - 19.3\zeta)^{\frac{1}{2}}) \right]_{z_0/L}^{z/L} \end{aligned}$$

$$\varphi_h = 0.95((1 - 11.6\zeta)^{\frac{1}{2}}) \quad (\text{A.3})$$

$$\begin{aligned} \psi_h(\zeta) &= \int_{z_0/L}^{z/L} \frac{1 - \phi_h(\zeta)}{\zeta} d\zeta \quad (\text{A.4}) \\ &= 2 \cdot 0.95 \operatorname{atanh}((1 - 11.6\zeta)^{\frac{1}{2}}) + \ln(\zeta) \end{aligned}$$

Universal functions after Grachev et al. (2007) for stable conditions ($\zeta > 0$)

$$\varphi_m = 1 + \frac{6.5\zeta(1 + \zeta)^{\frac{1}{3}}}{1.3 + \zeta} \quad (\text{A.5})$$

$$\psi_m(\zeta) = \int_{z_0/L}^{z/L} \frac{1 - \phi_m(\zeta)}{\zeta} d\zeta = \int_{z_0/L}^{z/L} \frac{1 - 1 + \frac{6.5\zeta(1+\zeta)^{\frac{1}{3}}}{1.3+\zeta}}{\zeta} d\zeta \quad (\text{A.6})$$

$$= \left[-19.5(1 + \zeta)^{\frac{1}{3}} - 7.5367 \arctan(0.57735 - 1.72489(1 + \zeta)^{\frac{1}{3}}) \right. \\ \left. + 4.35131 \ln(3 + 4.4814(1 + \zeta)^{\frac{1}{3}}) \right. \\ \left. - 2.17566 \ln(3 - 4.4814(1 + \zeta)^{\frac{1}{3}} + 6.69433(1 + \zeta)^{\frac{2}{3}}) \right]_{z_0/L}^{z/L}$$

$$\varphi_h = 1 + \frac{5\zeta(1 + \zeta)}{1 + 3\zeta + \zeta^2} \quad (\text{A.7})$$

$$\psi_h = \int_{z_0/L}^{z/L} \frac{1 - \phi_h(\zeta)}{\zeta} d\zeta = \int_{z_0/L}^{z/L} \frac{1 + \frac{5\zeta(1+\zeta)}{1+3\zeta+\zeta^2}}{\zeta} d\zeta \quad (\text{A.8})$$

$$= \left[(-5 + \sqrt{5}) \ln(-3 + \sqrt{5} - 2\zeta) - \frac{1}{2}(5 + 5\sqrt{5}) \ln(3 + \sqrt{5} + 2\zeta) \right]_{z_0/L}^{z/L}$$

A.2 Freezing characteristics

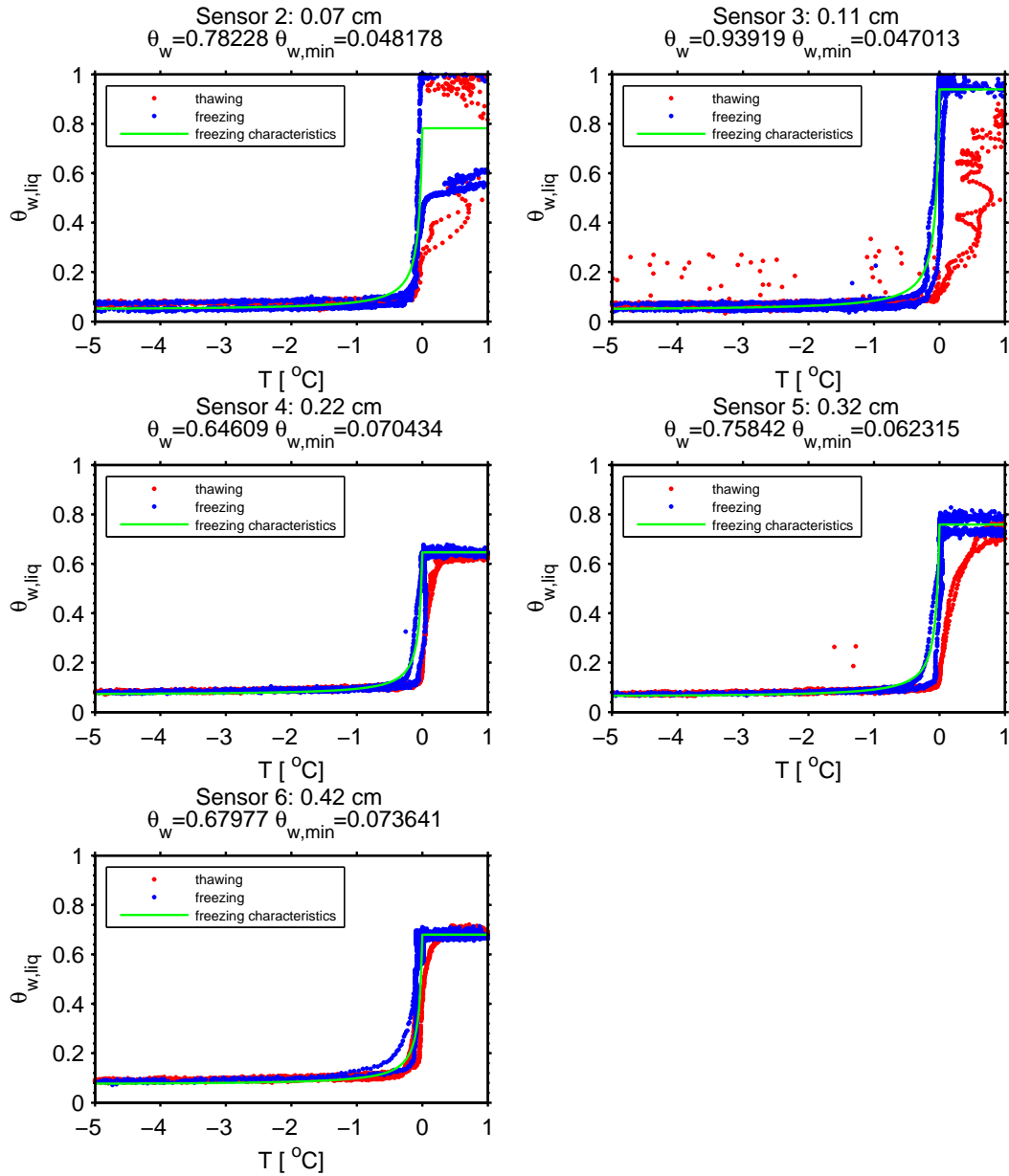


Figure A.1: Freezing characteristics for the five combinations of temperature and TDR sensors in the centre of the polygon. All datapoints of the modelling period August 2010 until August 2012. Function used as freezing characteristics in the model in black. Water content values determines by averaging over the thawed period for the total water content and the period below -10°C for the minimal water content

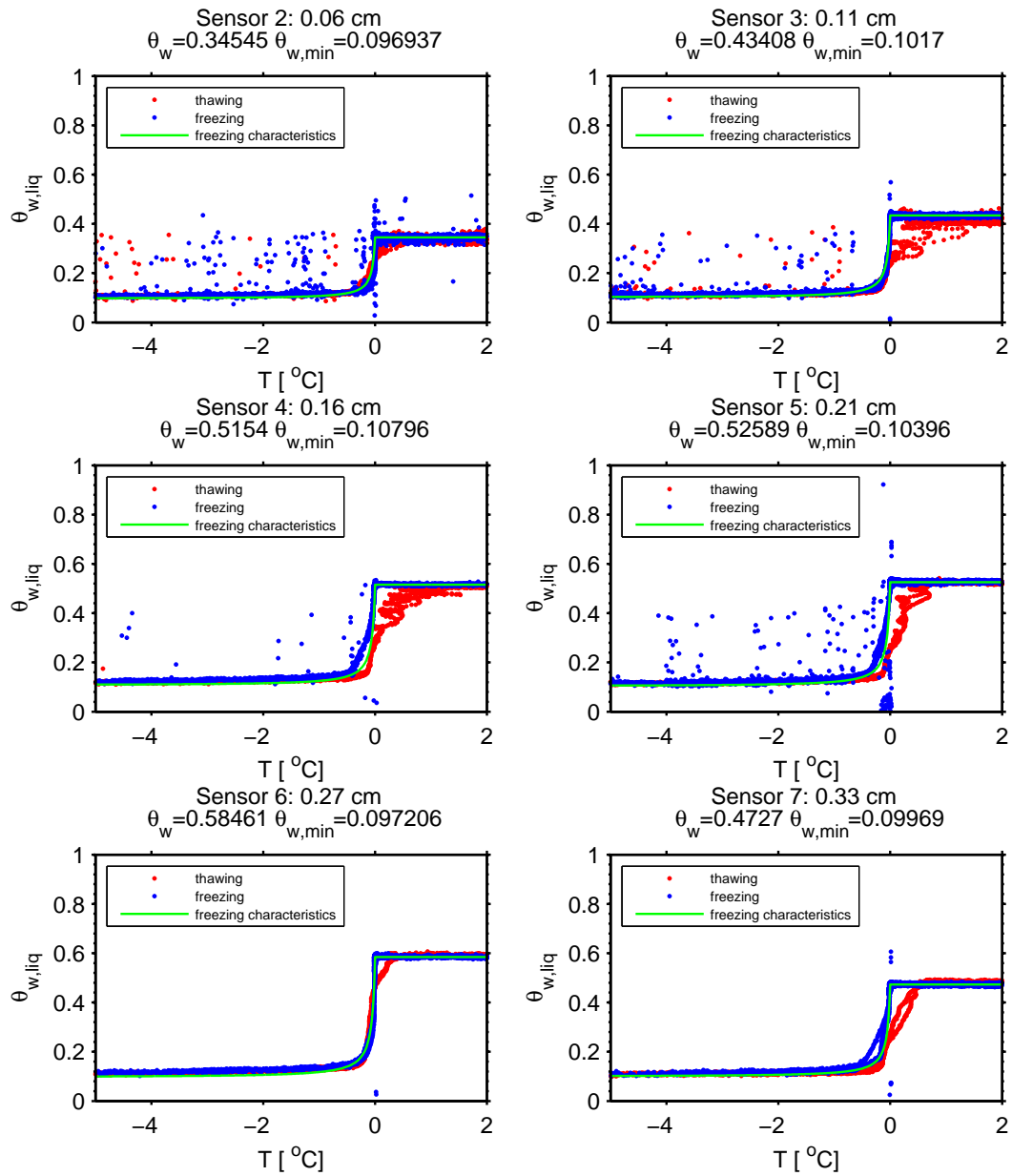


Figure A.2: Freezing characteristics for the six upper combinations of temperature and TDR sensors in the rim of the polygon. All datapoints of the modelling period August 2010 until August 2012. Function used as freezing characteristics in the model in black. Water content values determines by averaging over the thawed period for the total water content and the period below -10 °C for the minimal water content

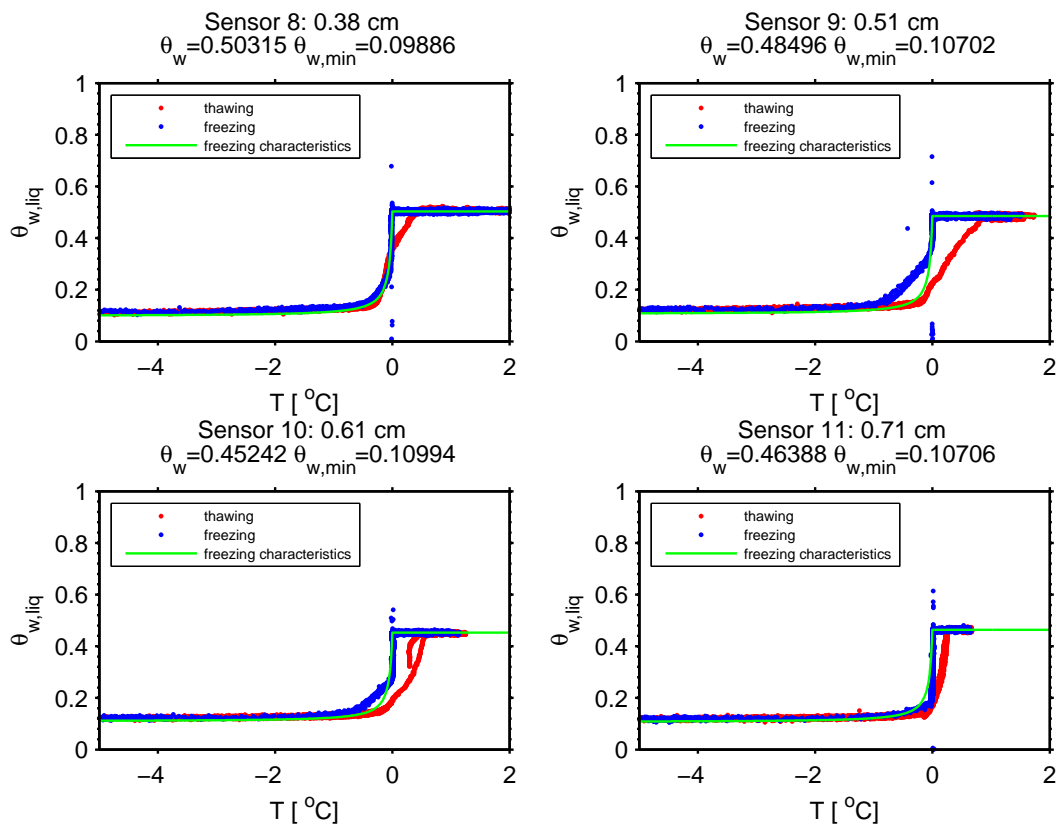


Figure A.3: Freezing characteristics for the four lower TDR sensors in the rim of the polygon. All data points of the modelling period August 2010 until August 2012. Function used as freezing characteristics in the model in black. Water content values determines by averaging over the thawed period for the total water content and the period below -10 °C for the minimal water content

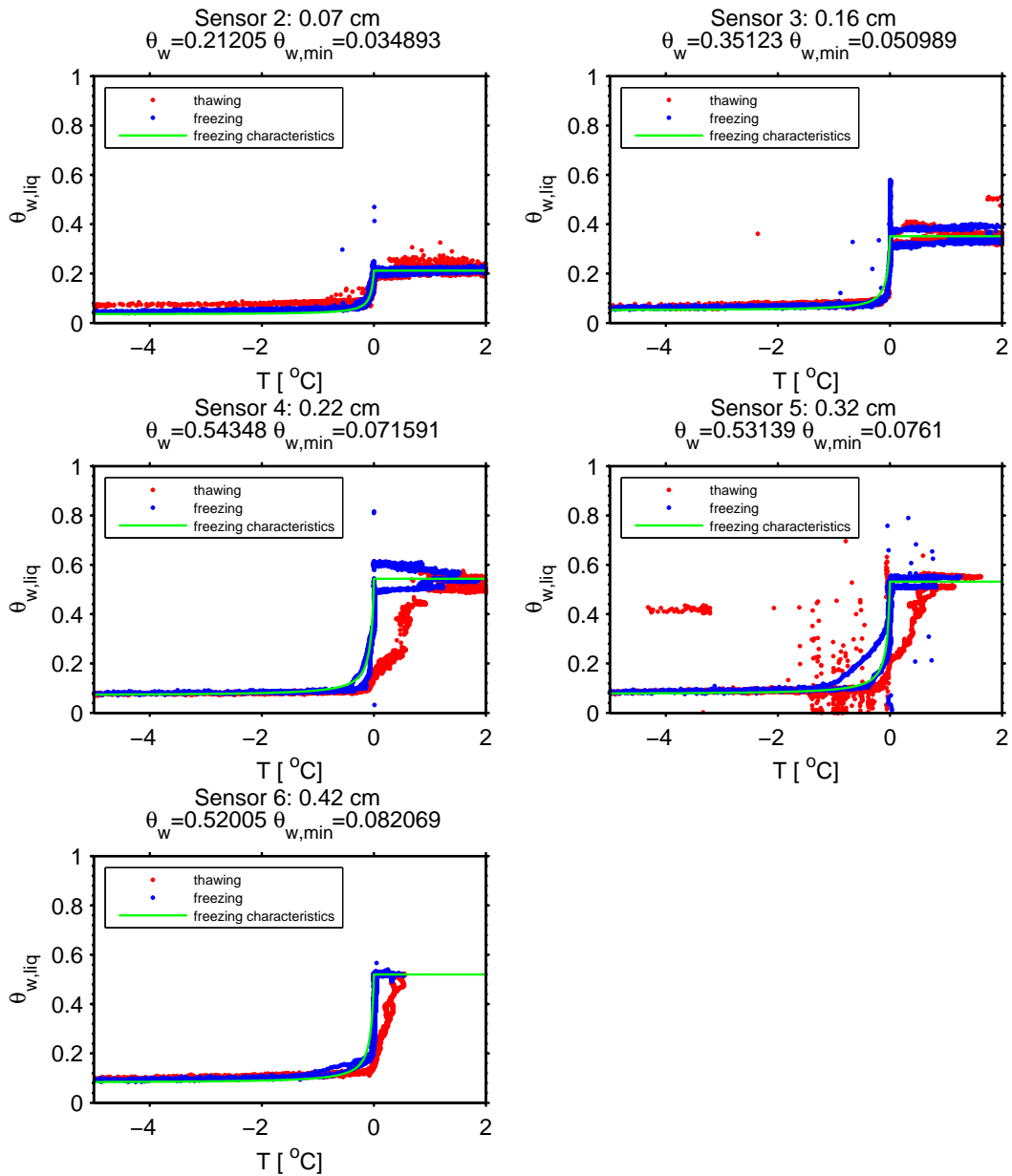


Figure A.4: Freezing characteristics for the five combinations of temperature and TDR sensors in the slope of the polygon. All datapoint of the modelling period August 2010 until August 2012. Function used as freezing characteristics in the model in black. Water content values determines by averaging over the thawed period for the total water content and the period below -10°C for the minimal water content

A.3 Correction of soil temperature offset

The soil temperature data used in this study is taken with sensors that have been installed about ten years ago, so a significant drift in the range of about 1 K can occur. This does not seem very dramatic in comparison to the temperature range of several during the annual cycle in the uppermost soil layers (-35°C to 20°C). But in the range around the 0°C this can have a strong influence on the initial conditions of the model due to the large differences in latent heat of thawed or frozen soil layers. Furthermore a consistent validation of the model results from comparisons to measurement data would definitely fail with temperature curves that show large offsets around the freezing point. The correction procedure is based on the fact, that the freezing period can be clearly identified in the measured temperature curves and must occur at a temperature of 0°C . The response function of the temperature sensors is not linear over the whole measurement range, so the offset from the drift of the sensors will not be constant over the measurement range. This will lead to a possible over- or underestimation of the correction at high and low temperatures. This is accepted as these smaller deviations do not have a strong influence at these temperatures and as there is no better information of the possible sensor drift in these temperature range anyway. Figures A.5, A.7, A.6 shows the uncorrected temperature data for all sensors of the three soil profile during the freezing periods of the years 2010 and 2011.

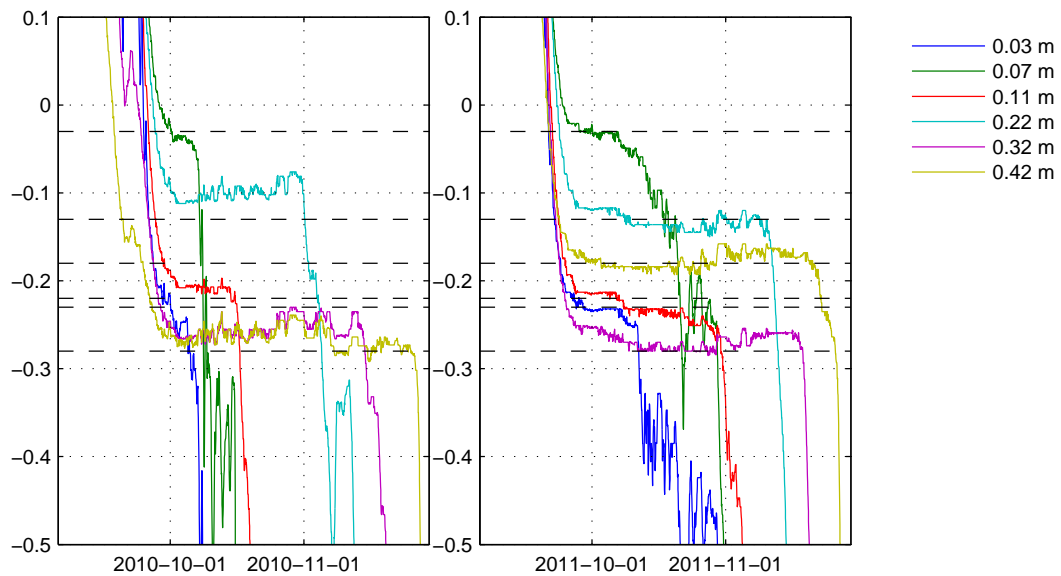


Figure A.5: Temperature data during the freezing periods of 2010 and 2011 before the offset correction for the polygon centre. The dashed lines indicate the offset value chosen and subtracted from the data for the whole modelling period from August 2010 to August 2012

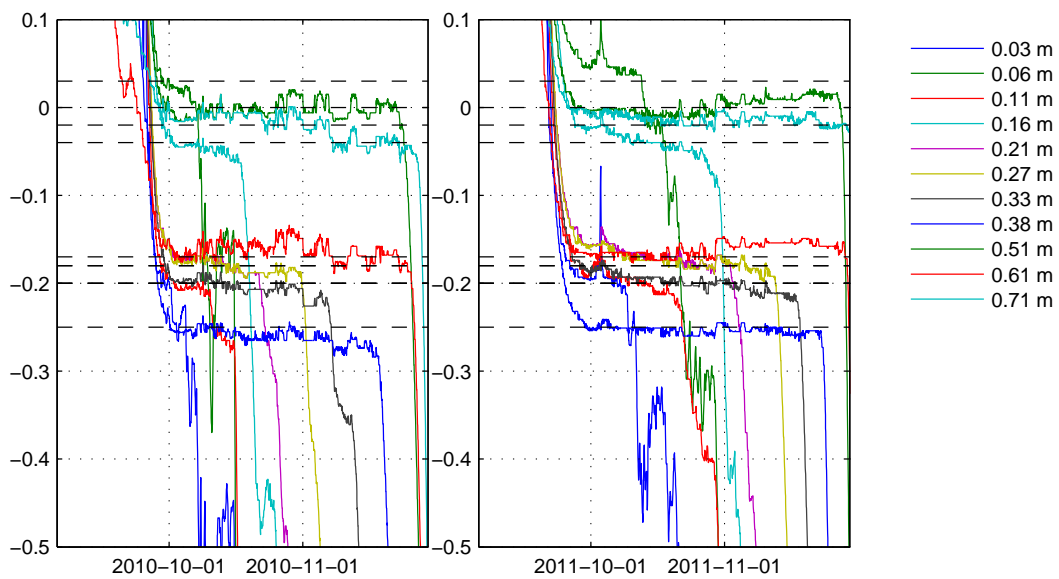


Figure A.6: Temperature data during the freezing periods of 2010 and 2011 before the offset correction for the polygon rim. The dashed lines indicate the offset value chosen and subtracted from the data for the whole modelling period from August 2010 to August 2012

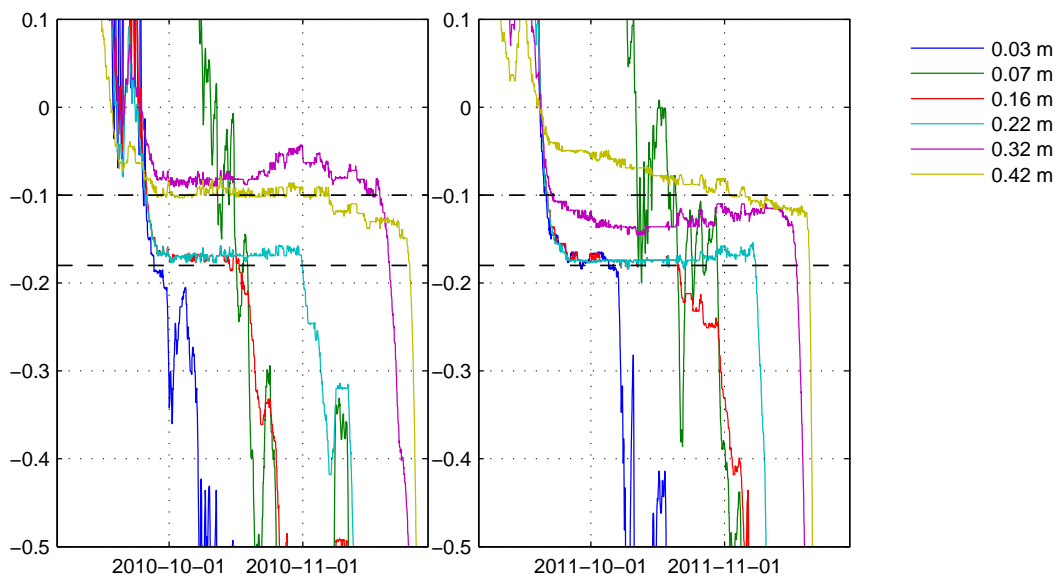


Figure A.7: Temperature data during the freezing periods of 2010 and 2011 before the offset correction for the polygon slope. The dashed lines indicate the offset value chosen and subtracted from the data for the whole modelling period from August 2010 to August 2012

A.4 Soil model with forcing from temperature sensors

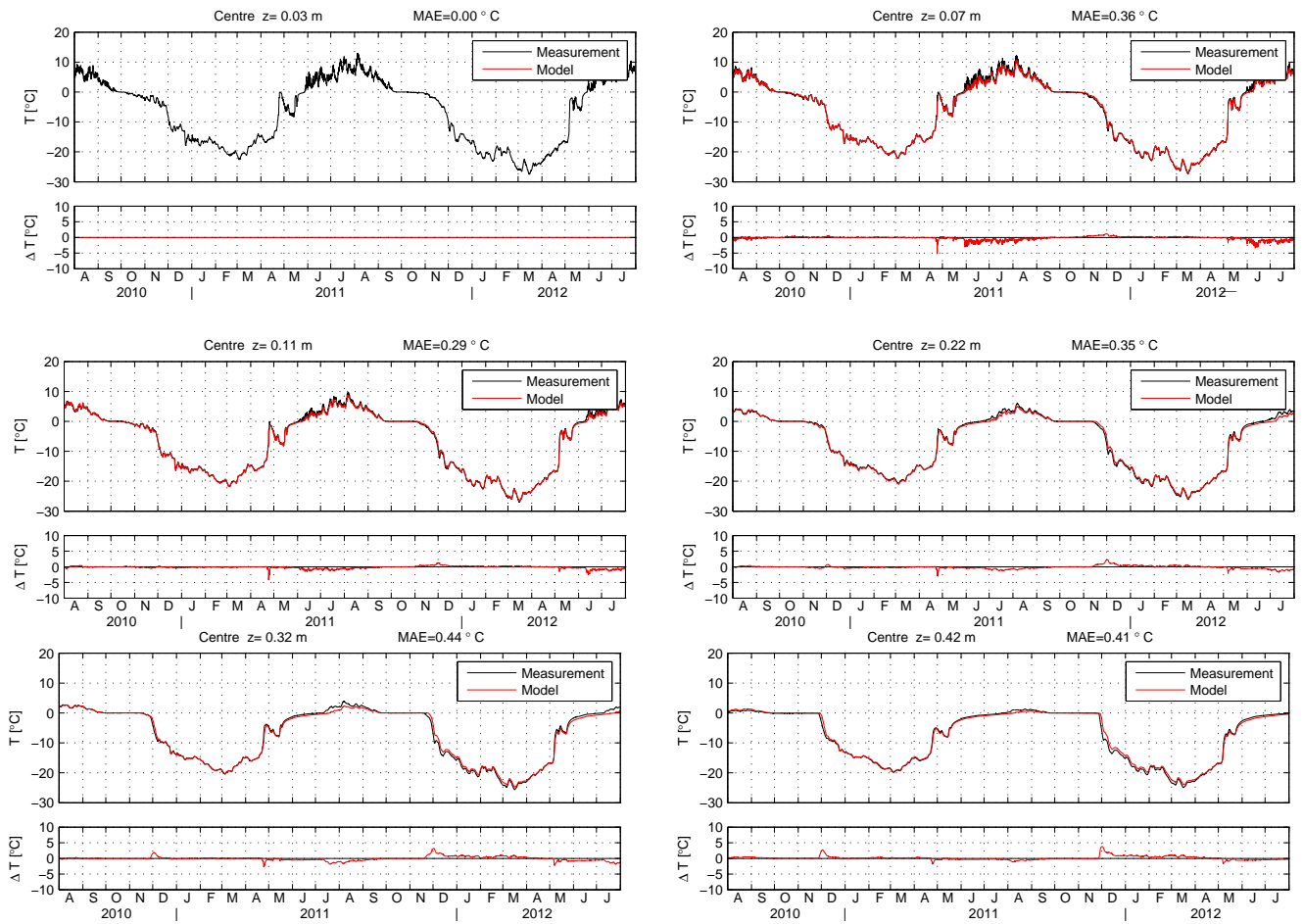


Figure A.8: Measured soil temperature (black) and simulated soil temperatures (red) with forcing from the uppermost sensor for the six sensors in the polygon centre. Only measurement for the uppermost sensors as it was used as boundary condition

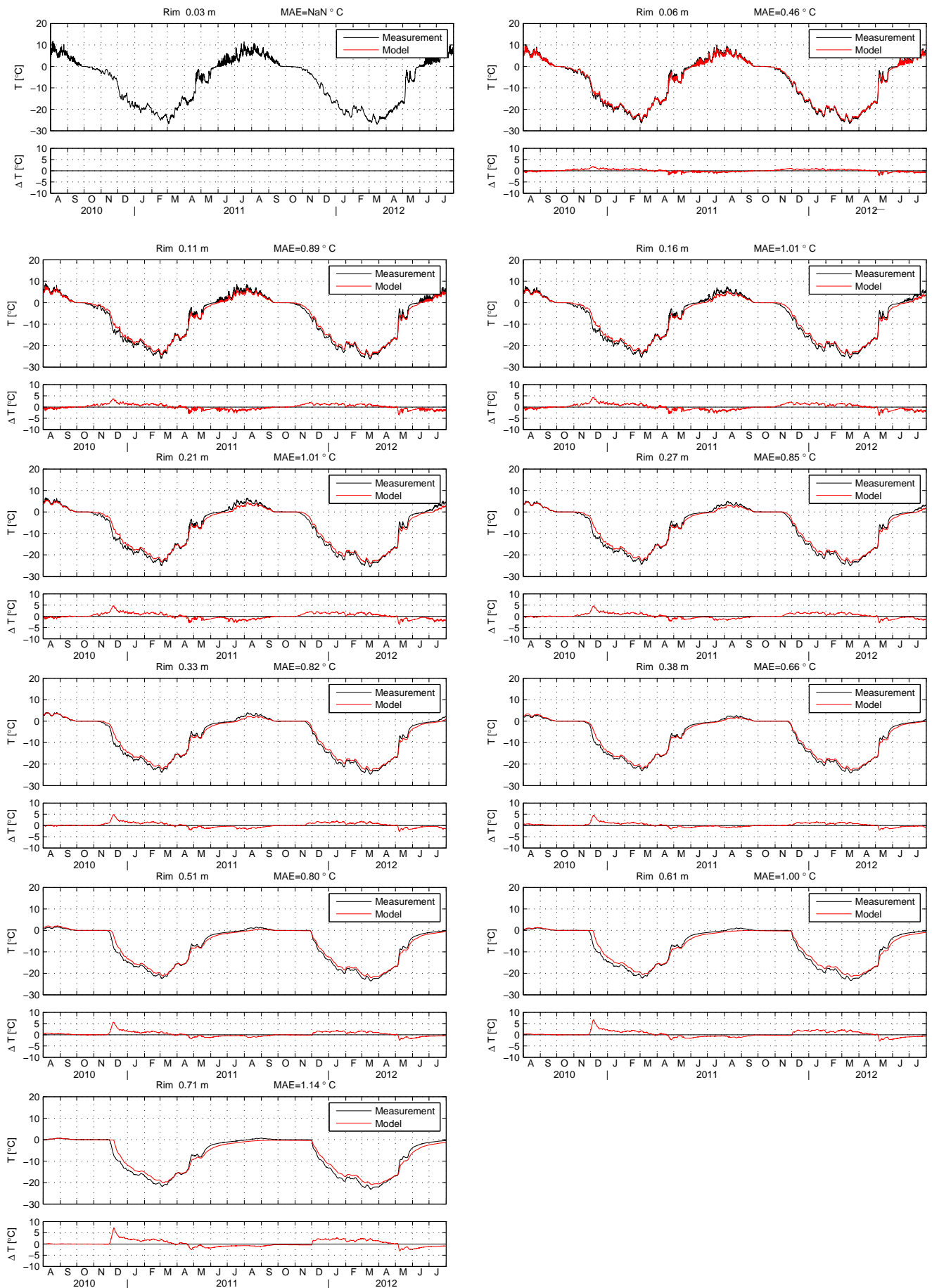


Figure A.9: Measured soil temperature (black) and simulated soil temperatures (red) with forcing from the uppermost sensor for the sensors in the polygon rim. Only measurement for the uppermost sensors as it was used as boundary condition

A.5 Coupled model with surface energy balance calculations

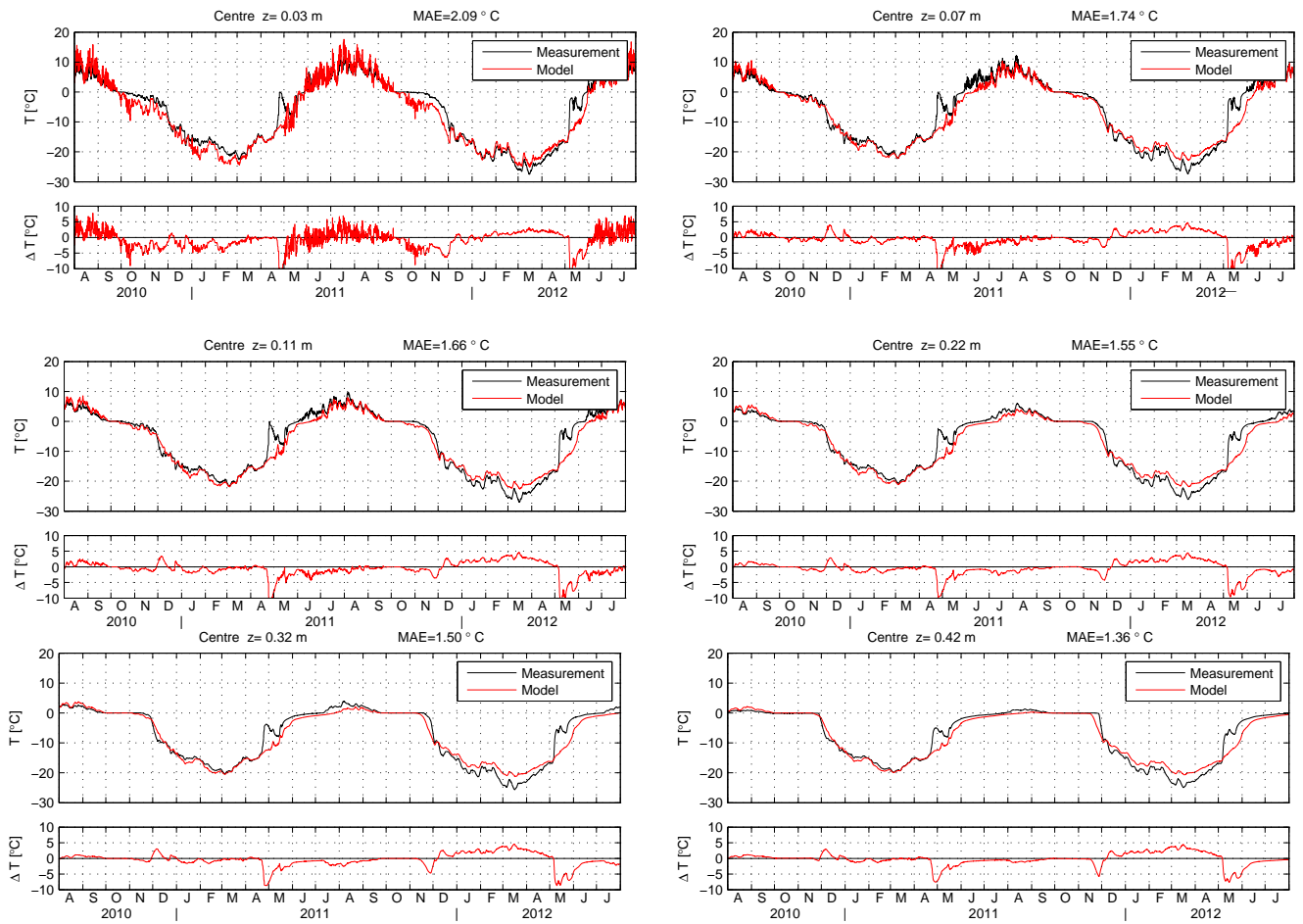


Figure A.10: Measured soil temperature (black) and simulated soil temperatures (red) with forcing from the surface energy balance model in the polygon centre

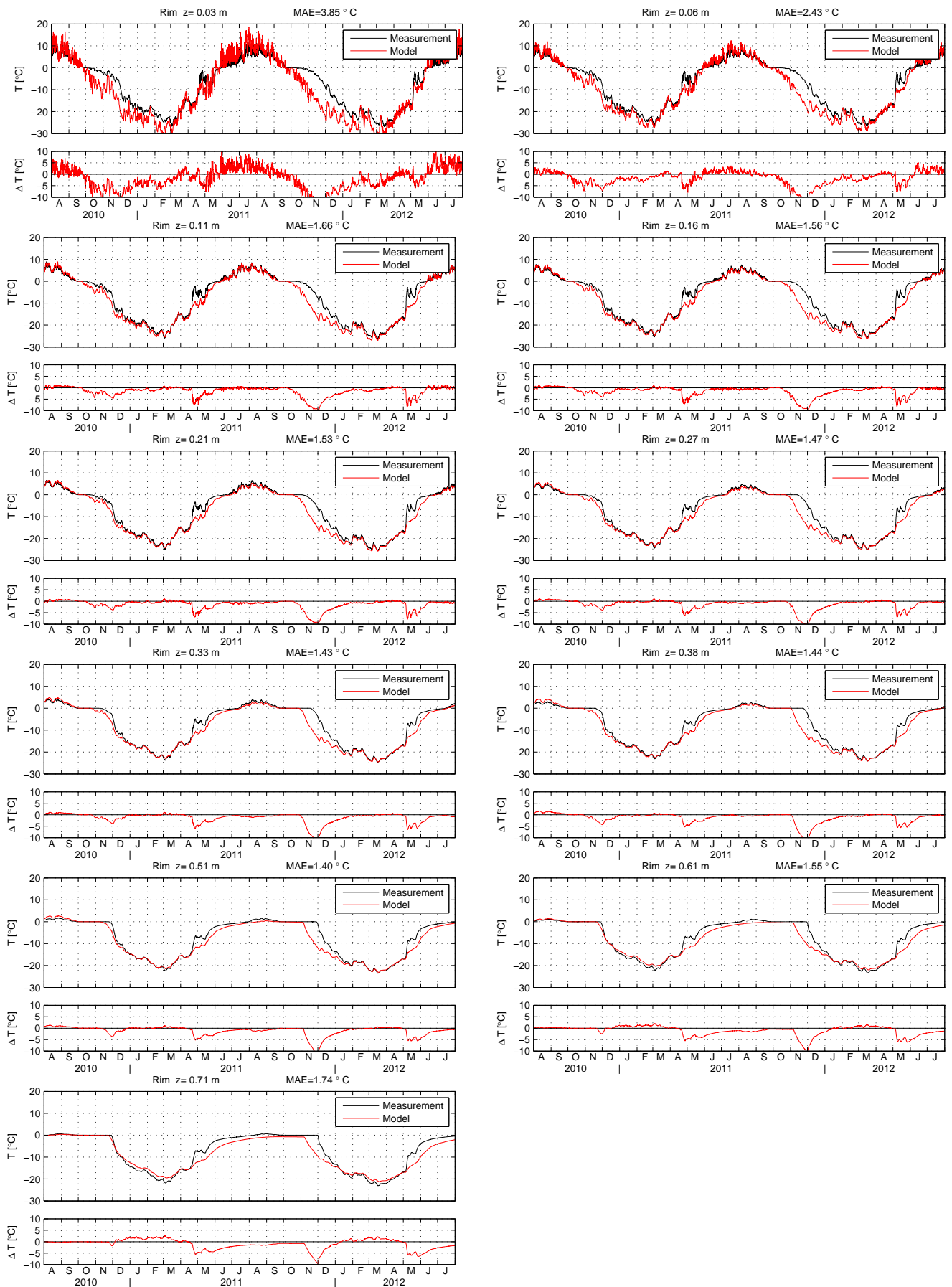


Figure A.11: Measured soil temperature (black) and simulated soil temperatures (red) with forcing from the surface energy balance model for the sensors in the polygon rim.

A.6 Variation of the organic surface layer

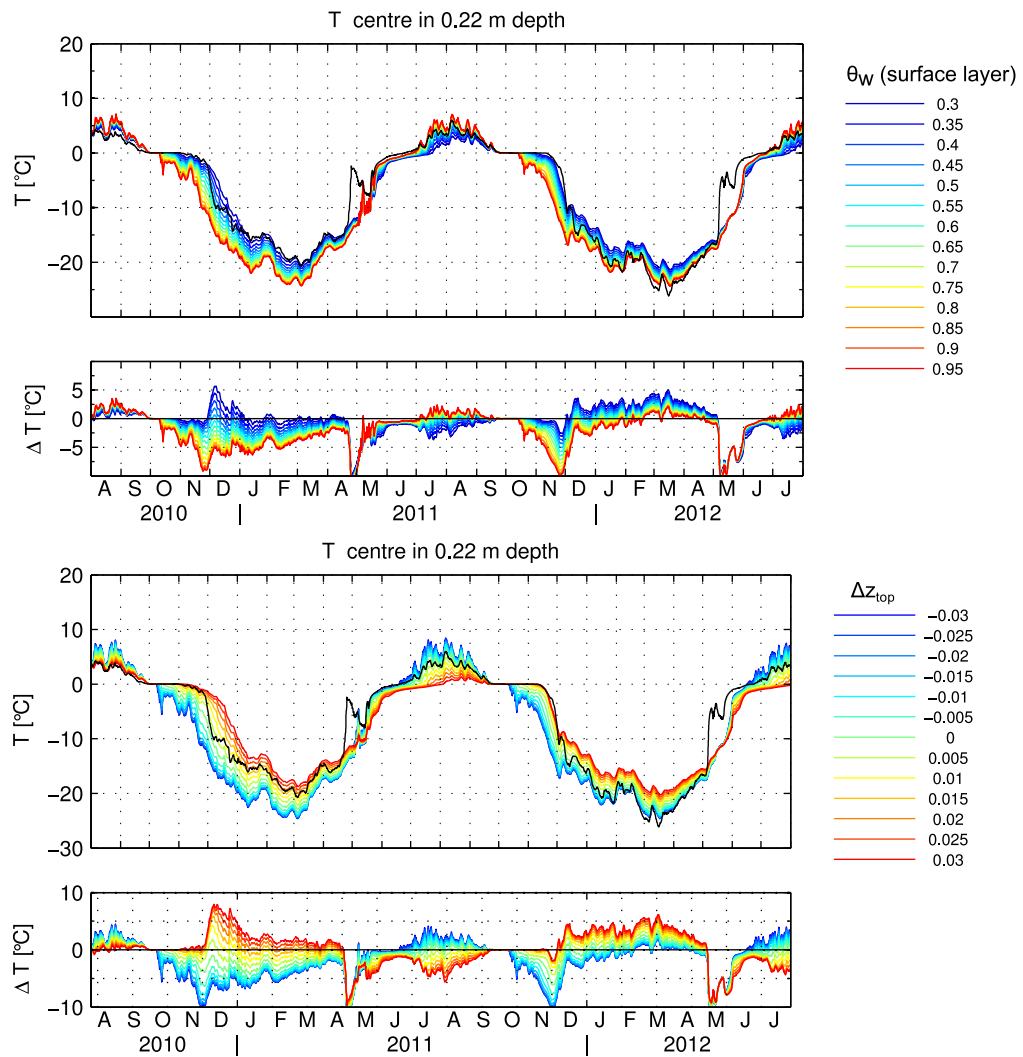


Figure A.12: Soil temperature in 0 cm depth in the polygon centre for a variation of the organic layer at the soil surface. *Top:* Variation of the soil water content in the uppermost 3 cm *top:* Variation of the thickness of the surface layer

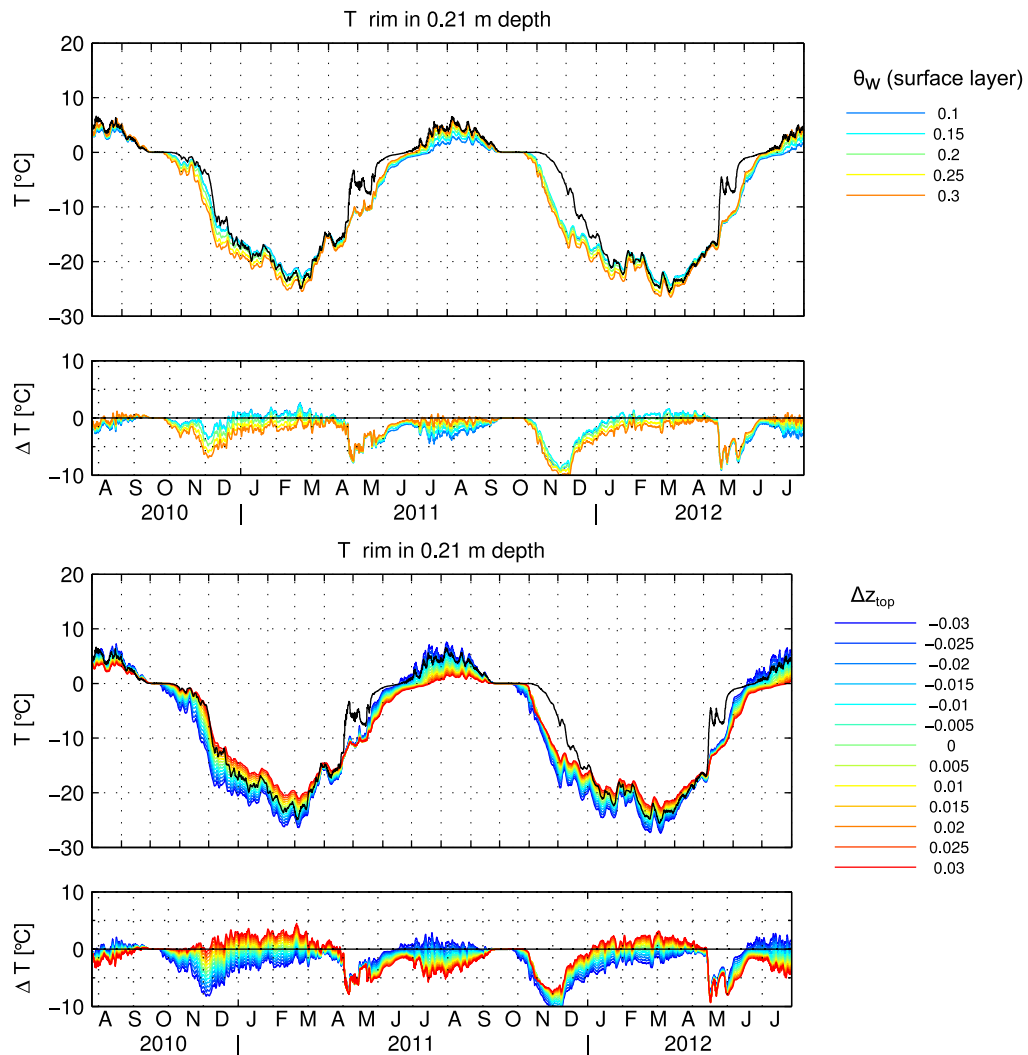


Figure A.13: Soil temperature in 20 cm depth in the polygonal rim for a variation of the organic layer at the soil surface. *Top:* Variation of the soil water content in the uppermost 3 cm. *Bottom:* Variation of the thickness of the surface layer

Erklärung:

Ich versichere, dass ich diese Arbeit selbstständig verfasst habe und keine anderen als die angegebenen Quellen und Hilfsmittel benutzt habe.

Heidelberg, den 17.08.2013

.....